



ROS-scavenging magnetic nanocubes as a novel theranostic for brain cancer

Supervisor

Prof. Gianni Ciofani

Co-Supervisor

Dr. Christos Tapeinos

Candidate

Francesca Tomatis

242453

POLITECNICO DI TORINO

Biomedical Engineering Master Thesis

Academic Year 2017/2018

A Edo, Mamma e Papà
Verso nuove avventure... e oltre!

Table of contents

Table of contents.....	i
1. Introduction.....	1
1.1. Current GBM treatments	2
1.2. State of the art	4
1.3. Nanoparticles	6
1.3.1. Types of nanoparticles	6
1.3.2. Commercialized nanoparticles	10
1.3.3. In vivo barriers and the importance of the targeting.....	10
1.3.4. Nanoparticles' toxicity.....	12
2. Main Project: lipid-coated ROS-scavenging magnetic nanocubes	13
2.1. Hypotheses and objectives.....	13
2.2. Overview of the theory behind the instruments and the analysis methods	14
PART I: material synthesis and characterization	25
3. Synthesis and characterization of uncoated NPs	25
3.1. SEM and FIB analysis	28
3.2. FT-IR analysis	29
3.3. DLS analyses	31
3.4. TEM analysis	39
3.5. XRD analysis.....	40
3.6. EDS analysis	42
3.7. ICP analysis	42
3.8. BET analysis	43
3.9. Magnetic measurements: VSM and NMR.....	44
4. Antioxidant properties	46
5. Oxygen generation	49
6. Coating and characterization	53
6.1. Cell membrane coating	54
6.1.1. Coating procedure.....	54
6.1.2. Characterization	55
Confocal analysis	55
SEM images	56
TEM images	56
FT-IR analysis	57

EDS analysis	57
ICP analysis	58
DLS analysis	58
TGA analysis.....	60
Antioxidant measurements.....	61
Magnetic measurements: VSM	62
6.2. Coating with cetyl palmitate	62
6.3. Coating with lipids	65
6.4. The protein corona effect.....	69
7. Hyperthermia experiments	77
8. Loading with temozolomide.....	86
9. Release studies.....	88
PART II: <i>in vitro</i> studies.....	90
10. Internalization	91
11. Viability studies	96
11.1. Metabolic assay	96
11.2. Proliferation test	97
11.3. Hyperthermia induced apoptosis.....	98
12. The blood brain barrier crossing	101
Conclusions.....	103
Appendix.....	105
Bibliography.....	108
Acknowledgments.....	119

1. Introduction

Glioblastoma multiforme (GBM) is a malignant tumor of the central nervous system (CNS). According to the 2016 World Health Organisation (WHO) classification of tumors, this neoplasm with astrocytic differentiation, 90% of which are classified as GBM [1], is one of the most commonly diagnosed brain cancers, that usually (in 60% of cases) affects people at ages between 55 and 74, most of which are men [2]. Unfortunately, this grade IV astrocytoma is rarely diagnosed in its initial stages since it behaves in an atypical way, because it has traits of extracranial tumors even if it is an intracranial one, and it is not easily treatable surgically. Moreover, GBM is characterized by numerous alterations, both genetic and epigenetic, which lead to cellular reorganization and extracellular matrix (ECM) modification. These changes result in a multiform number of mutation subgroups (MSG), and this is the reason why this cancer is called “multiforme” [3]. Besides the genetical alterations, this cancer is called multiforme also because of the way it presents itself, with pleomorphic nuclei and cells, regions of necrosis and regions of proliferation [4].

GBM presents also other specific characteristics. First of all, it is part of the group of the so-called diffuse astrocytic tumors, whose hallmark of malignancy is astrocytic tumor migration [5]. Migration and invasion of the GBM are linked with the overexpression of integrin $\alpha 3$ that activates the extracellular signal-regulated kinase (ERK) pathway [6]. This integrin is especially localized in invading cells and in cells surrounding vessels. Secondly, it shows an increased expression of some proteins. Indeed, mutant p53, a variant of the protein that in healthy conditions repairs the DNA, plays a key role in the modification from a low-grade astrocytoma to the high-grade glioblastoma [7]. Its nuclear localization has been correlated with long-term survival rates, because of the apoptosis induced by the protein and the consequent limitation of the cancer. In addition to the aforementioned, it has to be noticed that GBM cancer stem cells (GBMsc or GSC) can be identified by the presence of CD24 (also known as heat stable antigen – HSA), CD44 (hyaluronic acid receptor), CD133 and Hes3 positivity. These cells are highly resistant to treatment thanks to active mechanisms of DNA repair and self-regeneration, but these receptors make their targeting with specific functionalization possible.

GBMs' common symptoms include headache, nausea, vomiting (due to increased intracranial pressure), personality changes, motor weakness, slowing of cognitive function and seizures. Although, GBM is an aggressive form of cancer, extra cranial metastases are rare, either due to the short lifespan of the patients, or due to the obstruction of the metastatic cells by the absence of lymphatic transport in the brain [8]. Metastases of GBM is usually observed after a surgical resection and the consequent damage to the blood-brain barrier (BBB).

As in most of the tumor environments, also in GBM oxidative stress is huge due to cancer cells' metabolism [9]. Indeed, exaggerated quantities of reactive oxygen species (ROS), such as hydrogen peroxide (H_2O_2), hydroxyl radical ($\cdot OH$), superoxide anions (O_2^-) and hypochlorite anions (OCl^-), are produced in disease conditions. Even if these small reactive molecules, which are generated intracellularly and mostly in the mitochondria [10], in physiological concentrations take part in many metabolic pathways, they can become harmful when produced in excess. ROS overproduction is related with acidosis [11], that means a decrease of the pH which in turn is related with metastasis. The presence of ROS increases or maintain a low intracellular and extracellular pH and vice versa the acidosis can improve ROS production. The oxidative stress is also related with hypoxia [12], which is connected with the multidrug resistance (MDR) phenomenon [13] and angiogenesis [14].

1.1. Current GBM treatments

Nowadays, the most common treatments for GBM consist of surgical resection followed by radiotherapy and chemotherapy.

Neurosurgical methods for the resection of glioblastoma improved a lot over the decades, and one of the reasons is the possibility to use advanced imaging technologies that help surgeons to better understand the tumor pathophysiology and how to treat it. One of the most used imaging techniques is positron emission tomography (PET) [15], that exploits the different metabolism of cancer cells. Indeed, cells in the tumor site switch their way to produce ATP from the oxidative phosphorylation to the lactic acid production. Even if the last one is less efficient in general, the cancer can take advantage of it in order to proliferate and to differentiate into GBM [16]. However, spatial resolution of PET is still a limitation. Other imaging techniques are available: tumor resection can be realized with the help of cortical mapping or can be fluorescence-guided.

Radiotherapy (RT) in the form of kilovoltage X-rays were first introduced during the 1940s, and megavoltage X-rays started to be part of the cancer treatments during the 1960s; nevertheless it was not until 1970s that these therapies were applied in the whole brain, and only after computed tomography and magnetic resonance imaging (MRI) were developed, the partial brain radiotherapy became possible [17]. Radiotherapy dose escalation was attempted through brachytherapy, but this kind of therapy resulted in numerous problems, such as, worsening neurological deficit, increased seizure activity, infection, hemorrhage, pulmonary embolus, and radiation therapy necrosis. It has to be noted that, brachytherapy was combined also with hyperthermia (also known as thermotherapy) thanks to ferromagnetic implants that could be heated by an external stimulus. Although, this technique improved the survival of the patients, at least 50% of them undergo a second surgery due to the observed resistance of these patients in the radiotherapy. This relative radio-resistance was

explained by the ability of the hypoxic tumor cells to withstand sublethal damage. These cells required a higher dose of radiation to reach the cellular death compared to the healthy and oxygenated cells.

Nowadays, the radiation therapy is applied at a maximum of 60 Gy over 6 weeks and the method of intensity-modulated radiotherapy (IMRT) allows the treatment using different doses in different brain areas producing multiple beamlets of radiation [17]. Unfortunately, this technique requires a significant amount of time.

In the last but most robustly used treatment, chemotherapy, different **chemotherapeutic agents** can be used, but the most employed one is temozolomide (TMZ) [3]. This drug, approved by the European Agency for the evaluation of Medicinal Products in 1999 [18] and by the Food and Drug Administration (FDA) in 2005, is an alkylating agent which once it is found inside the body, at physiological pH, it is converted to monomethyltriazenoimidazolecarboxamide (MTIC). MTIC methylates the O6- and N7-positions of guanine in the DNA of the tumor cells, with the help of a methyl diazonium ion, [19] and can alkylate DNA during all phases of the cell cycle, resulting in the inhibition of the DNA replication and the induction of the cell-cycle arrest and of apoptosis. It has been observed that the covalent DNA changes happen more in the brain tumors cells compared to normal tissue, [20] and this can be probably explained due to the different pH environment of the two types of cells, coupled with different abilities to repair the methylated lesions. An alternative hypothesis is that in some cases tumor cells may have more exposed guanine-rich regions than normal cells.

The TMZ dose for glioblastoma patients is 75 mg/m²/day for 42 days, then 150 mg/m² po once/day for 5 days/month during the next month, followed by 200 mg/m² po once/day for 5 days/month in subsequent months for a total of 6 to 12 months. Patients receiving chemotherapy require a complete blood count (CBC) at varying intervals in order to determine if there are changes in the blood cell counts. Unluckily, TMZ is successful only in 40% of clinical cases [21], and its effectiveness is limited by the hypoxia-induced MDR phenomenon and by a small number of miRNAs, like miR-455-3p and miR-10a, the decrease of which has shown to allow the enhancement of the TMZ treatment [22]. miRNAs have been also shown to be implicated in the proliferation and the invasion of GBM [16].

Other common employed agents against GBM are 5-fluorouracil, carmustine, semustine, cisplatin, procarbazine and lomustine (CCNU), the latter of which showed to highly improve the life expectancy of some GBM patients [17].

These treatments are usually not enough to completely eradicate the tumor and there are several factors that limit their efficacy. One of them, for example, is Mgmt gene, which is responsible for the production of the Mgmt protein, able to fix the DNA damage caused by RT and TMZ in cancer cells [23]. The survival rate after the common treatments is approximately 50% after 1 year from the

diagnosis, 25% after 2 years, and 10 to 15% after 5 years. Many patients cannot tolerate the considerable side effects that therapies involve and suffer from low quality of life. Moreover, there is often the tumor relapse.

1.2. State of the art

Of course, the best way to improve the survival rate would be to achieve an **early diagnosis** of cancer. Different solutions could become possible and among them, the detecting of biomarkers is a promising way to follow. An example is the exploitation of the presence of microvesicles. Microvesicles derive from the plasma membrane of the cells from which they are released, and they carry mRNA, miRNA, and proteins. It should be noted that the horizontal transfer of these components into the endothelial cells induces the angiogenic effect which is typical of the solid tumors [24]. Moreover, the quantity of GBM-derived microvesicles inside the patients' bloodstream was proved to decrease after the TMZ treatment [25]. Not only the serum can contain microvesicles, but it could also be analyzed to detect RNU6-1, a small non-coding RNA that is related with GBM [26]. Except this, a less specific sign of GBM, but a clue of a change in the nervous system environment, is the increase of certain proteins inside the cerebrospinal fluid (CSF), such as albumin and osteopontin [16]. An additional example of a prognostic indicator is PTEN, a phosphatase tumor suppressor fundamental in cellular homeostasis that is often mutated in GBM [27]. The advantage of exploiting biomarkers is that they are non-invasive, quick and accurate diagnostic tools.

Concerning the **imaging** techniques, PET/MRI scanners allow better diagnosis thanks to the combination of high-resolution anatomical imaging and functional imaging. In order to identify hypoxic cancer cells, [F]-fluoromisonidazole ([F]-FMISO) and Metronidazole, a hypoxic sensitizer, can be used as tracers.

If an early diagnosis could surely improve the survival rate of patients, new therapies are also fundamental. As intensity-modulated **radiotherapy** (IMRT) takes lots of time, another method named as volumetric-modulated arc therapy (VMAT) has been developed, in which the various parameters such as, dose rate, gantry speed and field aperture, dynamically change during the treatment [17]. Another recently tried treatment is hypofractionation, in which the total radiation dose is divided in large doses and treatments are provided less often but also for shorter periods of time. With hypofractionation the requested time and costs are reduced. Unluckily, it cannot improve the survival. Recently, mathematical algorithms have been developed in order to optimize radiotherapy for a single patient by analysing and simulating the specific tumor kinetics [28].

Concerning innovative **drugs** that act as novel chemotherapeutic agents, the AG-120 that targets isocitrate dehydrogenase (IDH-1) mutations, which are critical in the transition from the low-grade

tumor to the highest grade one, is the newest discovery by Agios pharmaceuticals that entered the clinical trials. The mutation is represented by an arginine that is replaced in the aminoacidic sequence of the enzyme and this change in the active site prevents it from converting isocitrate to alpha-ketoglutarate.

Immunotherapy is another promising technique for cancer treatment. The hypothesis that the immune system is able to kill cancerous cells is supported by the fact that increased incidences of cancer are exhibited in immunosuppressed patients [29]. Lots of immunological methods have been developed against tumors, such as adoptive cell-based therapies, tumor vaccines (it is possible to target proteins of the immune cascade or tumor proteins), monoclonal antibodies, and cytokine treatment. Popular therapeutic targets are the driver mutations of the cancer cells, which confer them the huge growth potential, and which are almost 50 in GBM [30]. In this brain tumor, an overexpressed receptor tyrosine kinase is the epidermal growth factor receptor (EGFR). It is involved in many processes, such as cell proliferation and inhibition of apoptosis. Moreover, a mutant variant of EGFR called EGFRvIII that was found in about 30% of primary GBM, not only increases tumorigenicity and cancer cell migration, but it also enhances the resistance to RT and TMZ-therapy. Exploiting this protein, the GBM vaccine Rindopepimut[®] which is a combination of EGFRvIII with the carrier protein keyhole limpet hemocyanin, that was developed and licensed in 2008, allows the specific elimination of cells expressing EGFRvIII [31]. Another immunotherapy technique is the induction of antigen-specific immune responses by employing dendritic cells which can be sensitized with different tumor antigens, and then be inserted in the body [32].

An alternative technique for the treatment of GBM that has already been approved by the Food and Drug Administration, is the tumor treating field (TTF) therapy, which leads in the termination of the tumor cell mitosis, due to an applied **alternating electric field**. This approach reached the clinical trials and showed minor side effects and high patient compliance [33].

Finally, **nanoparticle (NP) -based** delivery systems can be exploited against GBM because of their multiple advantages [34]. Indeed, these smart drug delivery systems (DDS) can improve the pharmacokinetics and pharmacodynamics of drugs, they can avoid the uptake by the reticuloendothelial system (RES), they can cross the BBB, they can combine different therapies and encapsulate various drugs, and they can reduce the side effects on the healthy tissues [35] by providing selectively specific amounts of drug at a tumour site. Moreover, NPs can take advantage of some of the abnormal properties of cancer cells in order to kill them or to induce their apoptosis.

1.3. Nanoparticles

Nanoparticles, defined as particles with dimensions of 1 to 100 nanometers by the National Institute of Health (NIH) of the United State of America, are considered an innovative approach both for the treatment and the diagnosis of GMB, due to some attractive characteristics they present, some of which are, easy fabrication procedures and consequently low cost, specific optical properties, controllable size and shape, responsiveness to biological, physical and chemical stimuli and biocompatibility. An additional advantage of using nanoparticles in biomedicine is their ability to be administered in the patients using various traditional routes, like oral, parenteral and ophthalmic.

NPs can have either a diagnostic or a therapeutic character, or a combination of them in the form of a theranostic system, which means that in a single type of nanoparticle it is possible to put together therapeutic and diagnostic abilities. Theranostic structures have the ability to detect endogenous abnormalities and to treat them, and can be exploited to map the metabolic pathways, in order to understand how a pathogenic condition develops [36]. The dimensions of the theranostic NPs vary depending the targeted tissue and the application, but a size of approximately 100 nm is considered a good compromise for the majority of the existing bio-applications [37]. An increased size may result to a higher uptake by the macrophages, while a smaller size may result to a faster reticulo endothelial system (RES) clearance.

Finally, it should be noted that, one more characteristic that makes nanoparticles attractive in the nanomedicine field, is their ability to response to various stimuli. Among the stimuli-responsive structures, most of them exploit physical (e.g., temperature [38], magnetic and electric fields [39], ultrasound [40] and osmotic pressure) or chemical (e.g., pH [41], ionic strength, and glucose) stimuli. Noteworthy, only a small amount of studies is related to biological stimuli, such as enzymes and ROS [36]. For example, if ROS are present, ROS-scavengers can be exploited. These are substances that react with ROS and lead to the formation of less active molecules.

1.3.1. *Types of nanoparticles*

Among the diagnostic NPs, there are the so-called **quantum dots (QD)** which are semiconductor crystals used as inorganic fluorophores. They are composed of a core of lead sulfide (PbS), cadmium selenide (CdSe) or cadmium sulfide (CdS); a shell that improves the quantum yield; a stabilizing layer that makes them biocompatible, as for example copolymer micelles [42]; a targeting group that imparts specificity to numerous cell surface ligands. Their fluorescence properties depend on the fact that when an electron in the valence band absorbs a photon, it is transferred to the conduction band and when it returns to the lower band there is an energy emission in the form of a photon. The higher the gap between the bands, the more the electron needs high frequencies and small wavelengths to

move, then the energy of the emitted photon is higher. Small QDs have a bigger band gap compared to larger ones, resulting to a fluorescence dependence on the dimension of the NPs. QDs can be used for imaging, both as single QDs and as QD-embedded NPs [43], and they have the advantage not to present the photobleaching effect like the traditional fluorescent dyes. QDs-loaded nanocapsules have been used for cell imaging and showed stability up to 30 days [44]. Moreover, the QDs core can be modified to enhance their magnetic properties, so the dots can be identified both from their fluorescence and their magnetic resonance. Among the applications of QDs, near-infrared imaging of deep tissues, single-particle tracking of biological processes, multimodal imaging of tumors, QD-based FRET processes, cellular delivery of QDs, and QD-based biosensors have been studied [45]. Finally, it has been shown that QDs can be also used as part of a possible therapeutic strategy, boron neutron capture therapy (BNCT) for GBM, if they are combined with boron nitride nanotubes (BNNT) [46].

Another type of NPs, used both for the diagnosis and for the therapy, is represented by **metal NPs**, such as gold and silver. These NPs have a diameter from 1 to 10 nm, they are relatively of low cost, they are biocompatible but one of their disadvantages is that they are not biodegradable. Metal NPs can be efficient markers thanks to the quantity of different techniques that can be used to reveal them, including, resonance light scattering (RLS), optical absorbance, fluorescence (as QDs, they do not present a photobleaching effect), Raman scattering, electrical conductivity, atomic force microscopy (AFM) and magnetic force microscopy (MFM). With respect to the therapeutic properties, these NPs are able to absorb the light and convert it into thermal energy rendering them capable to induce hyperthermia in cancer cells. The main disadvantage of these NPs is that they are too small, and they are eliminated fast from the body. Larger iron oxide NPs of approximately 10-50 nm, that present longer circulation times compared to the NPs with sizes less than 10 nm, have been shown to regulate plasma glucose in mice through radio-wave heating [47]. In this study, radio frequencies were exploited to penetrate the tissues and were absorbed by the NPs, resulting in an increase of their temperature which subsequently led to the opening of the calcium channels due to the thermal stimulation. Consequently, a pathway to modify the genetic expression was activated and insulin started to be produced by the cells. This was a proposed solution to decrease the glucose in tumor sites.

Magnetic NPs represent a subset of metal NPs used in the biomedical field. They can be single domain NPs [48], with a diameter that ranges from 5-20nm (usually made of iron [49], nickel [50], cobalt [51], or a combination of them [52] and they have the tendency to create agglomerates); multidomain NPs, with diameters larger than 20-25 nm; and microparticles with a polymeric matrix and iron oxide beads sprinkled inside or on the surface of the polymer. Magnetic NPs are useful as contrast agents, and they can also be exploited to induce hyperthermia into the tumors cells, but they are also capable to

physically destroy tumor cells as it was recently shown [53]. In this work, magnetic NPs that accumulated into the lysosomes were then stimulated with an external magnetic field. The resulting rotating vibrations of the NPs broke the organelles and the acidic pH of the lysosomes destroyed the rest of the cells. Ferromagnetic NPs smaller than 5-10 nm show a particular behavior, in which there is an absence of a residual magnetic hysteresis after the removal of an external applied magnetic field. This phenomenon is characterized as superparamagnetism and is a property that can be found in ultrasmall superparamagnetic iron oxide (USPIO) NPs. This property along with their high biocompatibility allowed these particles to reach into clinical trial and were successful in more than 70% of the treated patients. In order to avoid the fast elimination of USPIOs and SPIONs from the body due to their small size, these nanoparticles are encapsulated or attached covalently or through electrostatic interactions with larger structures, allowing them to be transferred through the circulatory system in the site of interest. Moreover, magnetic NPs can be guided with the help of an external magnetic field in order to accumulate into the desired site of the body. Magnetic guidance was proved into an *in vivo* study [54] where different groups of mice were treated with phosphate-buffered saline (PBS), drug alone or magnetic NPs loaded with both doxorubicin and verapamil hydrochloride. After the injection of the solution, a constant magnetic field of 2000 Oe was kept outside the skin near the tumor site at 25°C for 3 hours. The distribution of drug was significantly increased into the cancer site in the mice treated with NPs and magnetic guidance, proving that this approach was successful.

NanoTherm® is an example of an FDA-approved therapy for GBM exploiting magnetic NPs. It is an aqueous colloidal dispersion of iron oxide NPs with an average size from 10 to 15 nm [55]. The magnetic fluid is injected into the tumor site and the cancer cells uptake the NPs. Then an alternating magnetic field generator is positioned near the head of the patient and the NPs are stimulated to produce heat. Cells reach the temperature of 43°C and thanks to the hyperthermia effect an irreversible cytotoxicity is induced. This solution showed to increase the life expectancy of 6-10 months, but it cannot be used more than twice because of the high accumulation of NPs into the brain and because having too many NPs into the tumor site does not allow the use of MR to check the cancer growth [55].

Magnetic NPs were FDA approved even if they were considered not biodegradable because the excretory system through the kidneys was demonstrated. More recent studies proved that these NPs can be degraded by specific enzymes and the iron can become part of some metabolic paths into the body.

Nanoceria or CeO₂ NPs consist of cerium which is a rare earth element with multiple valence states. At the nanoscale, this valence states may change more quickly, and oxygen vacancies dramatically

increase. This fact confers catalytic properties to CeO₂ NPs, which mimic catalase and superoxide dismutase (SOD) enzymes inside the cells [56]. By regulating the REDOX reactions, they adjust the oxidative stress and the number of free radicals. Due to the change of their valence state these NPs can be used either as antioxidant or pro-oxidant depending their environment. CeO₂ NPs are also considered autoregenerative since, they are able to start a new antioxidant cycle immediately after the end of the previous one. CeO₂ NPs are antioxidant in environments with a basic pH and for pH lower than 5.5, like in the tumor sites or inside the lysosomes, they become pro-oxidant and toxic.

Solid lipid NPs (SLN) and/or **nanstructured lipid carriers (NLC)** are an additional type of NPs that attracts more and more the interest of researchers, mostly due to the high biocompatibility that these nanoparticles present, as well as due to their inherent ability to cross easily the BBB. These NPs are made from a combination of solid and/or liquid lipids, surfactants, and water. SLN and NLC are carrier systems for pharmaceutical agents and drugs (both hydrophobic and hydrophilic), they are not toxic, they increase the drug stability and its release, and they can be easily functionalized with a variety of targeting moieties in order to specifically target various pathogenic tissues. A recent example of theranostic SLN, is a system developed to encapsulate both the drug Sorafenib (Nexavar®), a hydrophobic drug to treat liver cancer, as well as SPIONs. The developed system was used not only for improved imaging, but it was also used for therapeutic purposes since it was shown to be able to inhibit the proliferation of cancer cells. In addition, this system showed great potential to be used as a guided drug delivery system as well as a system capable to exploit hyperthermia. Another type of lipid-based structures, similar to SLN and NLC that are used in the biomedical field, are liposomes. **Liposomes** are composed of phospholipids that in water create auto-assembling systems called micelles. Liposomes can be unilamellar or multilamellar and they can carry drugs, genes and antigens without causing an inflammatory response of the body. An example of self-assembled lipid-based nanocomplexes used to treat GBM are immunoliposomes such as sCL-p53 and SGT-53, which reached the clinical trials because they showed the induction of apoptosis after the treatment with standard chemotherapy [57]. In this system, the payload is encapsulated into a cationic liposome and the targeting is realized with an anti-transferrin receptor (TfR) antibody fragment. Due to this functionalization, the NPs are able to cross the BBB by TfR-mediated transcytosis and later they are uptaken by the tumor cells via receptor-mediated endocytosis. Unluckily, some adverse effects like fever, chills, hypotension and tachycardia have been reported.

Finally, polymeric and dendritic structures like **polymeric NPs** and **dendrimers** respectively, are also very common in the biomedical field. [58]. Polyethylene glycol (PEG) and poly(lactic-co-glycolic acid) (PLGA) are the most exploited polymers to create NPs, but also polyurethanes (PU) are usually used

thanks to the fact that they are adaptable materials. Over the years different polymeric systems have been realized for the co-encapsulation of drugs and iron oxide NPs.

1.3.2. Commercialized nanoparticles

Until now, three classes of NPs have been marketed for the treatment of different diseases: liposomes, polymeric micelles and NPs with albumin.

The first FDA-approved liposomal nanodrug, in 1995, was Doxil[®], which comprised a doxorubicin hydrochloride liposomal injection [59]. Although Doxil[®] increased the circulation half-life of doxorubicin and it enhanced the therapeutic effect of the drug, its limitation was that its maximum tolerated dose (MTD) was lower than the one of standard doxorubicin and that the patients in which the drug was administered exhibited the hand-foot syndrome which was a set of skin changes like desquamation on palms of the hands and soles of the feet.

The second liposomal nanoparticle that reached commercialization was Ferumoxide (Feridex[®] in the U.S and Endorem[®] in the EU) in 1996, which was a SPIO approved as a magnetic resonance imaging (MRI) agent [60], while the third one was Abraxane[®] in 2005. [61]. Abraxane[®] is an 130nm diameter NP that contains paclitaxel and is coated with albumin (Nab-paclitaxel). It has an MTD higher than the drug alone, while its half-life in the bloodstream is not altered.

In the category of the polymeric micelles the current representative is Genexol-PM[®]. Genexol-PM[®] is a polymeric micelle loaded with paclitaxel and was commercialized in Korea in 2007 [62]. It is made of a PEG shell and a polylactic acid (PLA) core with the drug. It shows an improved MTD, a higher loading versatility and the possibility to control the release.

Nowadays, the marketed NPs for therapeutic purposes include eleven liposomes, one albumin NP, and one polymeric micelle, all of which are characterized by a passive targeting. Moreover, three iron NPs have been approved for imaging purposes. Other types of NPs, such as BIND 014 [63], a self-assembly polymeric NP made of PLGA-PEG with aptamers as ligands and docetaxel as a drug, CALAA-01 [64], a PEG NP loaded with siRNA, and with transferrin and cyclodextrins on its surface and Doxorubicin NPs realized with a layer-by-layer method, are additional examples of NPs in the phase of the clinical trials [65].

1.3.3. In vivo barriers and the importance of the targeting

The enormous potential of NPs and their efficiency risk to be reduced or canceled by the *in vivo* barriers. The two major obstacles that the nano delivery systems have to overcome in order to successfully deliver their therapeutic cargo in the site of interest are their uptake by the macrophages

and the subsequent clearance from the reticuloendothelial system as well as their uptake by the vascular endothelium. When the nano delivery systems are designed to target the brain and treat GBM, this last factor should be carefully taken into consideration, because the presence of the BBB inhibits the delivery of numerous chemotherapeutics in the brain [66].

After the intravenous administration, NPs adsorb plasma components like opsonins onto their surface [67], leading to the attraction of monocytes and macrophages, and to the subsequent sequestration by the phagocytic cells of the RES and by organs such as the liver and the spleen that permit a passive filtration. Vessel leakiness is typical of diseased tissues, including some types of cancer (in this case it is referred to as the enhanced permeability and retention (EPR) effect), and this condition, although it leads to an accumulation of NPs in the cancerous tissues, it is not sufficient for the needed treatments. Moreover, NPs with a hydrodynamic radius smaller than 5nm are rapidly cleared by the glomerular filtration [68].

One of the first strategies that was used to overcome the problem of circulation time, was a predosing strategy, in which an excess of NPs without the drug was administered, aiming at saturating the RES clearing capacity and to block the hepatic uptake (but not the splenic one). After RES saturation loaded NPs would be administered [66]. Unfortunately, this method could not be used due to its high toxicity and immune-suppressiveness. Nowadays, the main solution to allow the NPs to reach the desired tissue, is to extend their circulation time without RES saturation, and to realize an active targeting. Size, surface chemistry, and shape are fundamental parameters that need to be taken into account in order to increase the NPs lifetime in the blood [69]. The superficial grafting usually involves hydrophilic polymers, the most used of which are polysaccharides, heparin, dextran, and PEG (PEGylation). Once the resistance of the NPs into the bloodstream is improved, then the functionalization with various ligands like, antibodies, aptamers, peptides or small molecules allows the crossing through the endothelial barrier, allowing the therapeutic nanostructures to reach the target tissue.

As it was mentioned above, one of the major obstacles for the treatment of GBM is the presence of the so called blood-brain barrier. BBB is a multi-cellular structure composed of brain endothelial cells, astrocytes and pericytes that envelope blood-brain vessels. Small molecules and NPs cannot cross the first part of the vessels because between the vascular endothelial cells there are intercellular tight junctions really restrictive. BBB from one side prevents the passage of toxic compounds that could harm the brain, but from the other side poses a major obstacle to the ability of drugs to reach the CNS [70].

1.3.4. Nanoparticles' toxicity

As NPs are more and more employed in biomedical applications, it is important to study their cytotoxicity, also called nanotoxicity. Two main problems related to NPs toxicity are the interruption of the cell membrane and the release of the magnetic core for the iron oxide NPs [71].

Small (around 3 nm) and spherical NPs can affect more the cell membrane integrity [72], in particular if they have dimensions comparable to the thickness of the phospholipid bilayer. Hydrophilic NPs can also lead to the formation of pores and holes inside the cell membrane, consequently leaving it interrupted. Moreover, the coating and surface chemical properties play an important role in the interaction of the NPs with the membrane. It should be mentioned that, the type of cells is also related with the toxicity that NPs present [73].

The interaction of the magnetite (Fe_3O_4) with cell components, due to the destruction of the protective shell of the NPs, can be the cause of homeostatic disturbances, with consequent increase of the oxidative stress, and damages to the cytoskeleton and the DNA. Nevertheless, as previously written, the catabolism inside the cells can also lead the iron of the NPs to be involved in some metabolic pathways [74].

2. Main Project: lipid-coated ROS-scavenging magnetic nanocubes

2.1. Hypotheses and objectives

Taking into consideration the limitations in the treatment of GBM, it was hypothesized that a multi-stimuli responsive nanovector could be designed and developed in order to enhance the therapeutic effect against the brain cancer by using synergistic treatments. As magnetic and antioxidant nanoparticles (MANPs) were described as feasible by the literature [75], it was hypothesized that multifunctional solid lipid nanoparticles, able to scavenge the overproduced ROS and in tandem to generate oxygen, able to increase temperature due to hyperthermia, and to specifically deliver through BBB the anticancer drug temozolomide loaded in the surface pores, would increase apoptosis and reduce the proliferation of the cancerous tissue. In order to test these hypotheses, the following objectives were set.

1. **Synthesis** of a manganese doped iron oxide nanocomposite in the form of nanocubes, able to induce hyperthermia and in tandem to scavenge ROS with the simultaneous generation of oxygen. **Characterization** of the NPs as the obvious and necessary objective to reach after the synthesis. Morphological characterization with the help of scanning electron microscopy (SEM), transmission electron microscopy (TEM), dynamic light scattering (DLS, also called photon correlation spectroscopy - PCS), and X-ray diffraction (XRD). Physicochemical analysis through Fourier transform infrared spectroscopy (FT-IR), energy dispersive X-ray spectrometry (EDX or EDS), X-ray photoelectron spectroscopy (XPS), inductively coupled plasma atomic emission spectrometry (ICP-AES, also called inductively coupled plasma optical emission spectroscopy – ICP-OES), Brunauer-Emmett-Teller (BET) porosimetry, nuclear magnetic resonance spectroscopy (NMR), and scanning with vibrating sample magnetometer (VSM).
2. Assessment of the **antioxidant ability** of the nanocubes as well as their ability to **generate oxygen**. The first one is important to reduce the acidosis and consequently the probably related metastasis, while the reduction of hypoxia is helpful not only to increase the responsiveness of cells to the drug and to the radiotherapy but also to block the angiogenesis inside the tumor. In addition, the increase in temperature during the ROS-scavenging activity was checked.
3. **Coating** of the nanocubes to improve the half-life in the bloodstream and the targeting. Coating by using the cell membrane (CM) as a biomimetic approach, followed by the lipid-based coating to have another kind of coated NPs to use and compare in the internalization experiments. Characterization of the coated NPs through SEM and TEM images, FT-IR and EDS analyses, ICP

tests, DLS measurements, XPS analysis and thermogravimetric analysis (TGA), magnetic measurements.

4. Assessment of the ability of the nanocubes to induce **hyperthermia** under the influence of an alternating magnetic field by applying different frequencies and different entities of the magnetic field. Optimization of the parameters for the successive experiments with the cells.
5. Assessment of the ability of the nanocubes to induce **apoptosis** under the influence of an alternating magnetic field and measurements through flow cytometry.
6. Assessment of the targeting and consequent **internalization** of the MANPs inside the cells
7. Cytotoxic evaluation of the nanocubes through **viability studies**. Alamar Blue as metabolic assay and PicoGreen® as proliferation test.
8. Transformation of MANPs into drug delivery systems: evaluation of the **loading** ability with DiO, doxorubicine and TMZ. **Release** profile of the nanocubes under various conditions of pH and with the help of an alternating magnetic field. High-performance liquid chromatography (HPLC) for both loading and release studies.
9. Assessment of the targeting ability and the ability of the nanocubes to pass the **BBB** using an *in vitro* culture model. Check of the enhancement of the crossing due to the presence of an external magnet.

2.2. Overview of the theory behind the instruments and the analysis methods

2.2.1. Dual beam system: Scanning Electron Microscopy and Focused Ion Beam Microscopy

Electron microscopes, in general, allow to reach higher magnification and resolution than optical microscopes, thanks to the low wavelength of the electrons used, instead of the photons. The image is realized by a focused electron beam that scans over the surface area of the sample and its most evident property is the three-dimensional appearance, due to the large depth of field. It has to be noted that the optics of the scanning electron microscope are similar to the ones of the scanning confocal laser microscope. SEM consists of an electron gun (that can be thermionic or field emission type) and a series of electromagnetic lenses and apertures, including condenser lenses and one objective lens. The signal electrons emitted by the sample are collected by the detector, composed of a Faraday cage and a scintillator that converts the electrons into photons, which then travel through a light guide and finally they are amplified with the help of a photomultiplier tube. The voltage necessary to generate the electron beam is in the range 1-40 kV [76]. High vacuum is usually used because the interaction between high-energy electrons and air molecules could cause a big energy loss, but solutions with a low vacuum also exist. When the high-energy beam reaches the specimen, two events happen: some electron are elastically scattered, they keep 60-80% of their energy and their deflection angles are large (backscattered electrons); while other electrons hit the atoms of the material and,

during the inelastic scattering, they lose a lot of energy and give it to the electrons of the sample that are ejected from it with a low angle (secondary electrons). Secondary electrons are useful to achieve the topographic contrast, while backscattered electrons allow to realize the elemental composition contrast. The sample needs a coating of gold, platinum, silver or chromium. It represents a protective layer for biological samples and materials that are sensitive to the electron beam: indeed, it defends the sample from the heat that the high-energy electrons can cause when they hit the specimen. Moreover, the coating is useful with non-conductive samples, too. For these specimens, it acts as a channel that allows charges to go away from the material. Otherwise, the non-conductive property of these materials would be a sort of “electron trap” and the accumulation of charges would affect the information of the image.

Standard focused ion beam instrument is similar to the SEM one, into which it can also be incorporated. FIB system consists of vacuum chambers (one for the source and ion column, one for the specimen and detectors, and one for the sample exchange), a liquid metal ion source, a vertical ion column, a sample holder, detectors, and a gas delivery system. The vacuum is on the order of 1×10^{-8} torr [77]. The liquid metal ion source is a tungsten needle linked to the reservoir with the source material and it provides ions of approximately 5 nm. The metal that is usually used, mostly because of its low melting point (29.8 °C), is gallium. The voltage that generates the ion beam is in the range 5-50 keV. The sample is sputtered, and it can release secondary electrons or secondary ions that then are collected by the detector.

2.2.2. Transmission Electron Microscopy

The optics of the transmission electron microscope are similar to the ones of the conventional transmission light microscope. Indeed, there is a light source, a condenser lens, a sample stage, an objective lens and a projector lens. TEM significantly differs from the light microscope in the fact that the beam is made of electrons instead of photons, that the lenses are electromagnetic instead of being glass lenses for visible light and that high vacuum is needed for its proper operation. Electromagnetic lenses are composed of solenoids, in which the current flows and creates a magnetic field. The electron beam is then focused and deflected by the field’s lines of force. The voltage used to generate the beam is higher than the one used for SEM: 200 kV is the commonly used value, but up to 1000 kV can also be reached [76]. The acceleration voltage V_0 determines the electron energy E following Equation 1.

$$E = eV_0 \quad (\text{Eq. 1})$$

The electron energy defines the wavelength of the electron, which in turn determines the resolution of the microscope, therefore, by setting the acceleration voltage the resolution is also decided.

TEM sample must be very thin (about 100 nm, but it depends on the atomic weight of the material), in order to be transparent for the electrons that need to be transmitted. In order to fit the holder, the sample must be 3 mm in diameter and if it is smaller it is mounted on a 3 mm mesh disc. Copper meshes coated with thin polymeric films allow the specimen not to fall into the vacuum column.

2.2.3. Dynamic Light Scattering/Photon Correlation Spectroscopy

Initially, this technique was also named QELS, because it exploited the quasi-elastic light scattering, or IFS (intensity fluctuation spectroscopy) [78]. The dynamic light scattering instrument, basically composed of a laser, a cell with the sample and a detector, is useful to get the information about the size and the polydispersity of particles as well as their Z-potential (surface charge).

Other characteristics can also be measured with this equipment, but the cited ones are the most important. In order to determine the **size**, the Brownian motion of the particles is measured thanks to the dynamic light scattering. Indeed, particles are constantly moving because of the bombardment of the molecules that surround them, and the relation between their size and their speed due to the Brownian motion is given by the following generalized Stokes-Einstein relation (Equation 2)

$$D_c = \frac{k_B T}{6\pi\eta\xi} \quad (\text{Eq. 2})$$

where D_c is the diffusion coefficient, k_B is the Boltzmann constant, η is the viscosity of the solution and ξ is the correlation length, that for diluted spherical particle suspension represents the radius of the particles [79]. In a liquid, small particles move faster than bigger ones and this difference of speed can be detected by exploiting a laser. When the light illuminates the particles, it is scattered, and its intensity fluctuations (due to the constructive and destructive interference of the scattered light) can be analyzed to know the speed of the particles, from which the size can be derived through the Stokes-Einstein equation. A typical size graph is an intensity distribution where on the y-axis there is the amplitude of the intensity, while on the x-axis there is the diameter dimension, expressed in nm. By exploiting Mie theory, the volume distribution and number distribution can be obtained from the intensity distribution. An idea of the size of the particles can also be extracted from the correlogram, a diagram of the correlation coefficient function of the time. Indeed, in the DLS instrument, there is a correlator, that compares two signals over a period of time and measures their degree of similarity (which of course decreases with time). If particles are big, for example, they move slowly, so the correlation decreases also in a slower way. Fluctuations in the lower part of the graph reveal the presence of aggregates.

Z-potential is an important measure of the superficial charge of the NPs and it gives an idea of the stability of the particles in an aqueous solution. According to the Derjaguin-Landau-Verwey-Overbeek

(DLVO) theory, that predicts the stability of a colloidal system by considering the attractive Van der Waals interactions and the repulsive forces caused by the electrostatic double layer (EDL) [80], the higher is the absolute modulus of the Z-potential ($Z < -30$ mV or $Z > +30$ mV), the higher is the stability in water, because the particles repel each other. For lower values of the Z-potential, the particles tend to aggregate and collapse in a short period of time. A particle in a liquid is charged because of the ionization of the surface groups or because of the adsorption of charged molecules or ions, and it is surrounded by ions of the opposite charge which create a layer with strong interactions really close to the particle (Stern layer), but there are also ions with a weaker binding with the particle. The latter follow the particle during its movements only if they are close enough to it. The boundary between the ions that follow the particle and the ones that do not, it is called slipping plane, and the potential between the particle surface and this plane is exactly the Z-potential.

Zeta potential is measured through laser Doppler electrophoresis (a combination of electrophoresis and laser Doppler velocimetry), in which an electric field is applied, and the resulting speed of the NPs is measured, while the viscosity and the dielectric constant are known.

2.2.4. X-Ray Diffraction

XRD is a powerful technique that allows to understand the characteristics of crystalline materials. It gives information about structure, crystal orientation, grain size and crystal defects. A monochromatic beam of X-rays is generated in a cathode ray tube, which after filtering (to be monochromatic) and collimation, hits the sample and is scattered. The constructive interference that follows, produces typical peaks, the intensity of which is determined by the distribution of the atoms inside the material [81]. The Equation 3, that links the wavelength λ of the X-rays to the diffraction angle θ and the lattice spacing d in a crystal, is Bragg's relation.

$$n\lambda = 2d \sin \theta \quad (\text{Eq. 3})$$

n is an integer. The material is scanned in a range of 2θ angles in order to check all the possible diffraction directions. Once the graph with all the peaks is obtained, it is compared with standard reference patterns aiming to understand the compound of the unknown sample. In order to calculate the size of the crystallites, the Scherrer equation [82] can be exploited (Equation 4).

$$B = \frac{K\lambda}{d \cos \theta} \quad (\text{Eq. 4})$$

Where B is the width of the peak at half height, k is a shape factor that depends on the material, λ is the wavelength of the incidence beam, d is the dimension of the crystallite and θ is the considered angle. K has a value of about 0.9 for magnetite [83].

2.2.5. Fourier Transformed InfraRed spectroscopy

FT-IR spectroscopy is a useful technique to understand the chemical composition of samples. A light beam hits the material and it is absorbed by it, but the infrared radiation absorption depends on the molecule of the sample [84]. In particular, every material absorbs specific wavelengths based on the vibrational energy gap, and this implicates a change in the dipole moment of molecules. Therefore, the obtained spectrum is a vibrational spectrum. Typical units in infrared spectroscopy are wavenumbers, the reciprocal of the wavelength (in centimeters). To study the fundamental vibrations, mid-infrared rays are used. As this band goes from 2.5 μm to 25 μm , the reciprocals are

$$2.5 \mu\text{m} = 2.5 \times 10^{-4} \text{ cm} = 4000 \text{ cm}^{-1}$$

$$25 \mu\text{m} = 2.5 \times 10^{-3} \text{ cm} = 400 \text{ cm}^{-1}$$

So, the typical IR spectrum runs from 4000 cm^{-1} to 400 cm^{-1} . Thus, the wavenumber is directly related to energy and that means that the higher is the energy of the absorption, the higher is the wavenumber. Every peak in the final graph is characteristic of a particular binding between atoms of a specific substance, so it can be identified by comparing the graph with standard or previously studied spectra.

2.2.6. Energy Dispersive X-ray analysis/Energy Dispersive X-ray Spectrometry

EDS is usually coupled with SEM but it lets the user obtain chemical information about the sample. A beam hits the specimen, so some electrons are excited and their position in the energy level is occupied by other electrons previously in higher levels. Then, these electrons lose a defined quantity of energy that is released in the form of X-rays and measured with the help of an energy dispersive spectrometer. Every substance has a particular atomic structure, so a different energy is emitted if different materials are analyzed.

The typical spectrum obtained with an EDS analysis shows the counts per second per electron-volt (cps/eV) as a function of energy (keV). Every peak is then associated with a particular chemical element.

2.2.7. X-ray Photoelectron Spectroscopy

XPS technique allows to analyze the superficial level of a material, so it can be useful to get information about the coating of the NPs. Photoelectron production is the phenomenon for which a photon beam hits the sample electrons. The consequences of the photo-electron interaction are the annihilation of the photon, the energy transfer to the electron and the ejection of the electron from the atom if the energy is enough. The energy of a photon is expressed by Einstein equation (Equation 5).

$$E = h\nu \quad (\text{Eq. 5})$$

Where h is the Planck constant and ν is the frequency of the radiation. This energy is transformed into kinetic energy (KE) of the electron and into the necessary energy to emit it from its atom, that is the binding energy (BE). As a consequence, Equation 6 is valid.

$$BE = h\nu - KE \quad (\text{Eq. 6})$$

The photon energy represents a known parameter. The kinetic energy of the electron is the measurable parameter and it depends on the particular atom of origin. Therefore, the XPS technique is useful to perform an elemental analysis of the surface of the specimen. The typical XPS spectra are functions of the photoelectron and Auger electrons emission [85].

2.2.8. Inductively Coupled Plasma atomic/optical emission spectroscopy

ICP represents an elemental test which gives quantitative information about the material composition. In ICP analysis, the sample is solubilized and sprayed in a chamber. Meanwhile, an argon plasma passes through a coil with a high frequency alternated current, so an alternating magnetic field is produced. Electrons start to move following the magnetic field's force lines, with a circular trajectory. Then they collide with the argon atoms, so a stable and extremely hot plasma is produced. Thanks to the thermal energy, the sample is ionized. The electrons are excited and when they go back to their ground level, photons are emitted and can be detected. The emission spectrum is characteristic of the material. The spectrometer measures the light intensity and with the help of a calibration curve, it is possible to calculate the percentage of each element [86].

2.2.9. Brunauer-Emmett-Teller porosimetry

BET analysis is useful to quantify the surface area of a sample and its pore dimensions. The model at the base of this technique was developed in 1938 [87] as a multi-layer extension of the gas adsorption theory proposed by Langmuir in 1916, according to which the adsorption takes place only as a monolayer formation on the surface of the material, the adsorption is reversible, the adsorbate-adsorbate interaction is negligible if compared to the adsorbate-adsorbent one, and all the sites are energetically equals, so can be occupied with the same probability [88]. BET method is based on the following assumptions: homogeneous surface, the fact that molecules adsorption can happen even if the lower layer is not complete, and that no lateral interaction between molecules is present. The starting point is the adsorption isotherm which is the graph of the adsorbed volume as a function of the relative pressure [89]. Indeed, through nitrogen physisorption it is possible to obtain the specific surface area of the material, but also the total pore volume is a parameter that is commonly derived.

Equation 7 is the so-called BET relation.

$$q = q_m \left(\frac{C \left(\frac{p}{p_0} \right)}{\left\{ 1 - \frac{p}{p_0} + C \left(\frac{p}{p_0} \right) \right\} \cdot \left\{ 1 - \frac{p}{p_0} \right\}} \right) \quad (\text{Eq. 7})$$

q is the adsorbed amount of gas, q_m is the BET monolayer capacity, C is the dimensionless BET parameter (ratio between the adsorption constants) that is approximated with Equation 8.

$$C \approx \exp \left(\frac{E_1 - E_2}{RT} \right) \quad (\text{Eq. 8})$$

Herein, E_1 and E_2 are the molar adsorption energy of the first layer (E_1) and of the second and further layers (E_2). Once determined the monolayer capacity, it is possible to calculate the specific surface area with Equation 9.

$$S_{BET} = \frac{q_m \rho_{STP}^{vap} N_A A_{cs}}{M_{N_2}} \quad (\text{Eq. 9})$$

where ρ is the density of nitrogen vapor at standard temperature and pressure, N_A is Avogadro's constant, A_{cs} is the cross-sectional area of nitrogen molecule (0.162 nm^2), and M_{N_2} is nitrogen's molar mass. Another adsorption derived property is the pore size distribution, that can be found through the Barrett, Joyner, Halenda (BJH) method. It assumes that for a specific relative pressure, the volume of adsorbate inside the pores of the material depends on two factors: the formation of layers of adsorbed molecules on the pore surface and the condensation of the adsorbate due to the capillary phenomenon.

The sample is purified by degassing. Regarding the specimen, one of the problems of this technique is that the sample must be dried, but the drying method can deeply affect the results of the analysis. For example, oven-dried samples show more aggregation than the freeze-dried ones, leading to a reduction of the specific surface area [90].

2.2.10. Thermogravimetric Analysis

TGA can be helpful to get information about the coating of the NPs. It exploits weigh-recording balances focused on temperature both to analyze a material or to modify it [91]. This technique basically consists in measuring a physico-chemical property at elevated temperatures and in particular, the changes in weight that are detected as a function of the increasing temperature.

The thermogravimetric results can be presented in two ways [92]:

- Thermogravimetric curve: weight function of temperature (here the weight axis can be presented as weight scale, as percentage of the weight, as percentage of the weight loss, as fraction of the total weight lost, etc.)
- Differential thermogravimetric curve: rate of loss of weight versus temperature.

2.2.11. Nuclear Magnetic Resonance relaxometry

Standard NMR spectroscopy allows to observe local magnetic fields around atomic nuclei. The most common technique is the H-NMR, based on hydrogen atoms, but C-NMR exists too, and it is based on ¹³C atoms. An electromagnetic radiation is used to change the nuclear spin from the low energy condition (aligned with the external magnetic field) to the higher one (opposite to the external magnetic field). The necessary energy to realize this transition depends on the applied magnetic field and it is given by the electromagnetic radiation in the radio frequencies. When the nucleus goes back to the aligned condition, a signal in the radio frequencies is emitted. The Fourier analysis of the output produces the NMR spectrum where the absorbance is a function of the applied radio frequency.

An important parameter is the chemical shift, as defined in Equation 10.

$$\delta = \frac{\nu_{res} - \nu_{ref}}{\nu_{ref}} \quad (\text{Eq. 10})$$

where ν_{res} is the resonance frequency of the sample (frequency of the signal), while ν_{ref} is the reference frequency of the spectrometer. The magnetic field conveyed to the nucleus is affected by the structure of the molecule and it depends also on how many and what type of atoms are present near it. Then, for different material the same atom has different chemical shifts. The electrons create a shield around protons because they are responsible for an opposite magnetic field with respect to the external one. If the electron density around a proton increases, the chemical shift decreases. In the obtained graph, each chemical group produces a peak that changes when the group is added to a molecule because it is affected by this interaction. The area of each peak is proportional to the number of hydrogen protons that the peak represents.

The solvent is usually deuterated, meaning that it has deuterons in place of its protons. The sample is spun at 20 Hz, and phases of locking, shimming, and tuning are necessary to respectively compensate for variations in the magnetic field strength, to optimize the current in the coils and to tune the NMR probe for the right frequency. This technique is useful to understand if a functionalization was successful, for example.

NMR relaxometry allows to monitor slow dynamics in many different materials and compared to standard NMR equipment it has a fast-switchable magnetic field. In this technique, nuclear magnetic

moments are used to measure specific physical and chemical properties of materials. In particular, the relaxation rate of nuclear spin depends on the mobility (fluctuations, diffusion) of the microscopic environment and the strength of the applied magnetic field. Strong magnetic fields lead to increased sensitivity on fast dynamics while low fields lead to increased sensitivity on slow dynamics. Thus, the relaxation rate as a function of the magnetic field strength is a fingerprint of the microscopic dynamics.

The source of magnetic field is an iron core electromagnet energized by a stabilized constant current power supply. T1 and T2 are the characteristic times of relaxation respectively along the z-axis and the xy-plane. The spin-spin relaxation process (T2) is due to the interaction among like or un-like nuclear spins, while spin-lattice (T1) refers to the interaction between the nuclear spins and all the surrounding environment (with direct or indirect energy exchange). Longitudinal (T1) and transverse (T2) relaxation times can be measured by applying different pulse sequences. Saturation Recovery (SR) sequence is the standard one for T1 measurements. This pulse sequence consists of a repeating block of two $\pi/2$ -pulses. The first pulse flips the nuclear magnetization from the z-axis, where it is initially directed, to the xy-plane; after a time ' τ ', during which the magnetization rebuilds itself along the longitudinal direction, a second pulse turns the reconstructed magnetization on the xy-plane. The height of this part of the magnetization is measured and, by repeating the $\pi/2$ - $\pi/2$ pulse sequence varying the time τ between the pulses, it is possible to reconstruct the recovery curve of the longitudinal magnetization. For T2 measurements, Carr-Purcell-Meiboom-Gill (CPMG) sequence can be used: a $\pi/2$ pulse is followed by a series of π -pulses. The $\pi/2$ -pulse excites the nuclei turning their spins in the xy-plane; the π -pulses refocus the rotating spins, reversing their motion in the xy-plane. After each π -pulse, an echo signal is generated and from the envelope of the echoes' amplitudes one can evaluate the T2 value. This sequence was invented to overcome the so-called problem of diffusion of resonating nuclei in liquid samples.

The magnetic field intensity is usually indicated with the corresponding Larmor frequency of the investigated nuclei, by following Equation 11.

$$2\pi\nu_L = \gamma B_0 \quad (\text{Eq. 11})$$

where $\gamma = 2.67513 \cdot 10^8 \text{ rad s}^{-1}T^{-1}$ is the gyromagnetic factor of the proton.

The efficiency of the sample as contrast agents can be evaluated by considering the nuclear relaxivities, r_1 and r_2 . They are calculated as the inverse of the relaxation times corrected for the host diamagnetic contribution (e.g. water) and normalized for the contrast agent concentration (Equation 12), that in the case of magnetic NPs is the concentration of the magnetic part.

$$r_i = \frac{\left(\frac{1}{T_i}\right)_{\text{measured}} - \left(\frac{1}{T_i}\right)_{\text{diamagnetic}}}{c} \quad (\text{Eq. 12})$$

2.2.12. Vibrating Sample Magnetometry

VSM gives information about the magnetic properties of the sample, similar to the one that can be obtained with a superconducting quantum interference device (SQUID). The sample is placed in a constant magnetic field and a vertical vibration is transmitted to it. Then, the alternating magnetic field of the sample generates an electric field in a coil based on Faraday's law of induction. The voltage induced in the sensing coil is proportional to the magnetization of the sample, thus the magnetic properties of the specimen can be recorded by a software and analyzed.

The magnetization M represents the quantity of magnetic moment per volume unit. The magnetic dipole moment is a measure of the ability of the dipole to align with an external magnetic field H . The relation between the magnetic field and the magnetization is reported in Equation 13 [93].

$$H = \chi M \quad (\text{Eq. 13})$$

χ is the volumetric magnetic susceptibility and it is dimensionless, while H and M are expressed in A/m. The field H can also be expressed in tesla or in oersted; M can be found expressed in emu/g. For diamagnets and paramagnets the previous law is linear, but for ferromagnets it has a sigmoidal shape: it increases rapidly at the beginning, then it becomes asymptotic as it approaches the magnetic saturation M_s . When the magnetic field decreases, the magnetization does not follow the same graph, but it shows a residual magnetization M_r . The coercivity or coercive field (H_c) is another important parameter and it represents the magnetic field that must be applied in the negative direction in order to have again a null magnetization. The hysteresis loop is shown in **Figure 2.1** and its area is a measure of the dissipated energy upon reversal of the field.

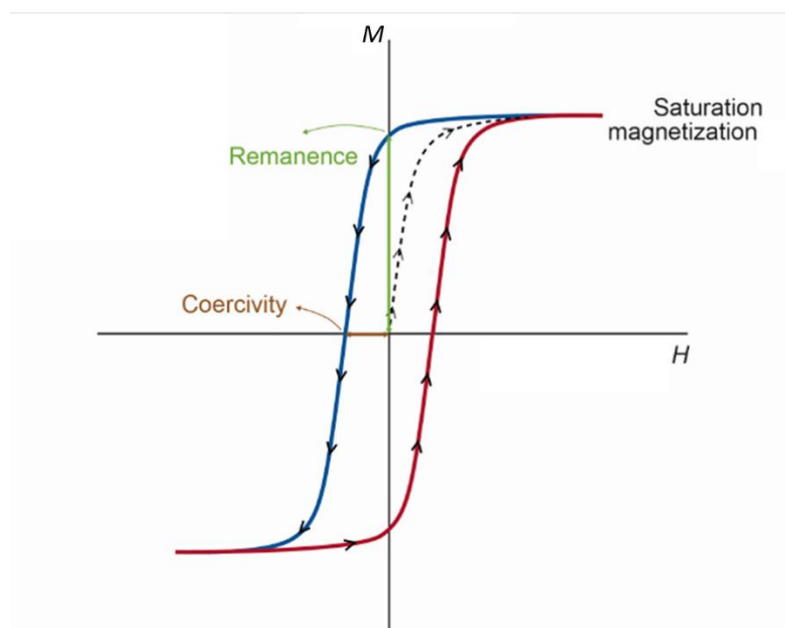


Figure 2.1 B-H sigmoidal curves for a ferromagnetic material. (Adapted from [93])

Moreover, the shape of the loop depends on the size of the particles, too. Indeed, for larger and multidomain particles the loop is narrow because the field energy needed to make the domain wall move is small, while in little particles with a single domain ground state the hysteresis loop is larger. For hyperthermia therapy, a large area enclosed by the graph B-H is the most effective one.

The external magnetic field H exerts on the magnetic NPs a force of attraction F_m defined by Equation 14, where V is the particle volume.

$$\vec{F}_m = V(\vec{M}_s \cdot \nabla)H \quad (\text{Eq. 14})$$

So, indirectly the force depends on the size.

Different materials give different values of M_s , M_r and H_c . For example, superparamagnetic Fe_3O_4 nanoparticles have an M_s around 75-80 emu/g and $H_c=0$ T (or Oe).

2.2.13. High Performance Liquid Chromatography

HPLC is a technique that allows to separate different substances dissolved in a solvent through a chromatography column. The affinity between the mobile phase and the stationary one is exploited: molecules that are more similar to the stationary phase need more time to go out of the chromatography column. Substances are revealed with UV radiation when they reach the end of the column. For each analyzed sample, a chromatogram is realized, and the peak of interest is kept into consideration because the area under the peak is proportional to the concentration of the molecule. The peak position depends on the sample, on the solvent and on the speed exploited to make the sample pass through the column.

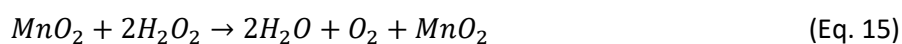
PART I: material synthesis and characterization

3. Synthesis and characterization of uncoated NPs

NPs in general can be produced with a top-down or a bottom-up approach. The first one does not guarantee a homogeneous dispersion when dimensions become too small, while the second type of synthesis is often preferred even if it usually involves solvents that then need to be carefully removed because of their toxicity. Bottom-up methods include precipitation (where the introduction of additives stabilizes the particles), condensation (where the additives help to produce the particles) and synthetic procedures (through which NPs are directly created). The MANPs presented in this thesis were fabricated with a bottom-up approach, in particular with a modified one-pot approach that was previously described by Liu et al. [75].

First of all, the core of the MANPs contained iron oxide (Fe_3O_4), also known as magnetite and characterized by a face-centered cubic cell unit. Thanks to this component, lots of advantages are reachable. First of all, the NPs can be magnetically guided directly to the cancer zone (an idea that Freeman et al. had in 1960 [94]) and they can be tracked in real time through the magnetic resonance navigation (MRN), that is achieved with a clinical MRI scanner upgraded with an insert of steering coils. Moreover, the magnetic property lets control the drug release in a better way (a method introduced by Kost et al. in 1987 [95]) and by using an external magnetic field it is possible to induce hyperthermia. Finally, the NPs can be easily tracked with imaging techniques.

Together with magnetite, the other principal material, cheap and abundant in nature, used for the NPs was manganese dioxide (MnO_2), also called ramsdellite: it is a ROS scavenger and it leads to oxygen generation. Therefore, the MANPs' shell of manganese dioxide is beneficial because it can reduce the oxidative stress in the tumour environment. In fact, MnO_2 represents a catalyst for the decomposition of the oxygen peroxide (Equation 15).



By looking at Equation 15 it is possible to see that among the products of the reaction there is also O_2 . So, the manganese dioxide shell of the NPs acts not only as a ROS scavenger but also as an oxygen generator.

MATERIALS

For the MANPs' synthesis, precursors of the abovementioned materials (magnetite and ramsdellite) were needed. So, 2.5 mmol of iron sulfate heptahydrate ($\text{FeSO}_4 \cdot 7\text{H}_2\text{O}$) were used as precursors of iron,

while potassium permanganate (KMnO₄) was the source of manganese. Six different molar ratios of manganese and iron were used:

$$\frac{Mn}{Fe} = \frac{1}{2}; \frac{Mn}{Fe} = \frac{1}{5}; \frac{Mn}{Fe} = \frac{1}{7.5}; \frac{Mn}{Fe} = \frac{1}{10}; \frac{Mn}{Fe} = \frac{1}{12.5}; \frac{Mn}{Fe} = 0$$

The same mass of FeSO₄·7H₂O was used for all the sample, while the KMnO₄ amount changed. The employed quantities of the materials are reported in **Table 3.1**.

Table 3.1 Materials and quantities used to realize the MANPs with six different molar ratios of manganese and iron

Mn/Fe	FeSO ₄ ·7H ₂ O	KMnO ₄	NaOH 5M	Deionized water
1/2	695 mg	198 mg	1 ml	99 ml
1/5	695 mg	79 mg	1 ml	99 ml
1/7.5	695 mg	53 mg	1 ml	99 ml
1/10	695 mg	40 mg	1 ml	99 ml
1/12.5	695 mg	32 mg	1 ml	99 ml
0	695 mg	-	1 ml	99 ml

Deionized water and sodium hydroxide (NaOH) 5 M were added to the solution at diverse time points. The materials were bought from Sigma Aldrich®.

PROCEDURE

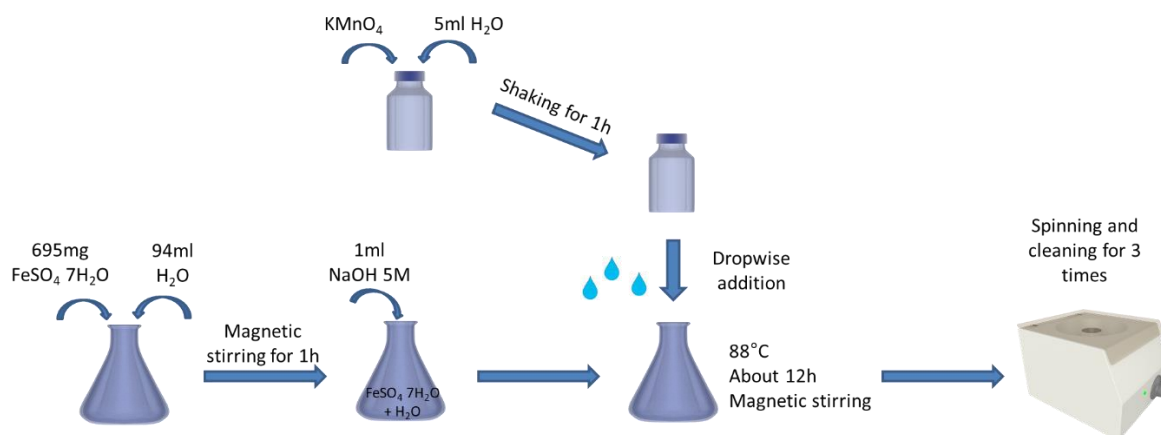


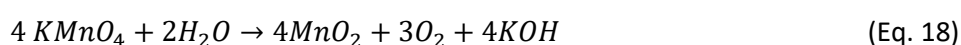
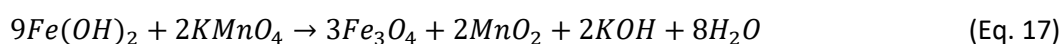
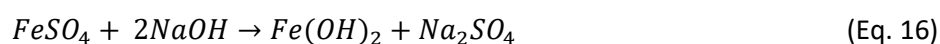
Figure 3.1 Scheme of the synthesis procedure of the MANPs

The fabricated MANPs were fabricated using a simple hydrothermal method as presented in **Figure 3.1** and after performing a detailed parametrical study. Briefly, the experimental procedure was as following described. The iron sulfate heptahydrate was dissolved in 94 ml of water in a conical flask under gentle magnetic stirring for one hour. Meanwhile, 5 ml of water were added to the potassium permanganate and left shaking. After 1 h, the speed of the stirring of the iron solution was increased in order to avoid the attraction of the magnetite nanoparticles by the stirring magnet and sodium hydroxide was added drop-by-drop (1 ml/min at room temperature), creating a dark green solution.

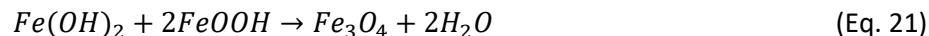
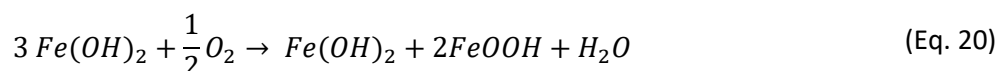
While adding the NaOH, the temperature was adjusted to 90 °C. When it reached 80°C (5-10 min), the KMnO₄ solution was added dropwise (1.5 ml/min) in the iron solution. Finally, the black solution was left at 88°C under magnetic stirring for 12 h. In the end, three cleanings with deionized water were accomplished: each time the solution was stirred down 10 min at 8965 xg and at 4°C.

DISCUSSION

The following redox reactions (Equation 16, 17, 18) explain what happened during the fabrication of the MANPs [75]:



Concerning the sample without the manganese, the reactions reported in Equation 19, 20, and 21 took place:



Thanks to the hydroxyl radicals on its surface, the MnO₂ has a strong affinity for the Fe₃O₄ nanoparticles, so it creates the shell layer [96]. In reality due to the one-pot procedure it is not possible to be sure that the core and the outer layer are completely separated. Probably the iron oxide core is doped with manganese dioxide particles, some of which cover the surface.

The main problem during the synthesis procedure was the oxidation of magnetite to maghemite, due to the fact that the procedure was realized in oxygen atmosphere. The transformation of the first oxide into the second one was not desired because even if both of them are ferromagnetic, the magnetite has a higher bulk saturation magnetization and a lower Curie temperature ($T_{C_{\text{magnetite}}} = 577^\circ\text{C}$). Indeed, the saturation magnetization of the magnetite is 92-100 emu/g, while the one of maghemite is 60-80 emu/g.

The yield of the procedure was calculated for every sample with the following formula (Equation 22)

$$\text{yield}(\%) = \frac{\text{final weigh of the material}}{\text{initial weigh of the material}} \times 100 \quad (\text{Eq. 22})$$

The sample with the ratio Mn/Fe=1/10 is the one with the highest yield, equal to 31.89%, while the worst results are the ones of the sample with ratios Mn/Fe=1/2 and Mn/Fe=1/7.5. **Table 3.2** contains all the calculated yields.

Table 3.2 Yields of the samples with different Mn/Fe ratios. The best result is the one of the sample with Mn/Fe=1/10.

Mn/Fe	yield (%)
1/2	11.37
1/5	13.70
1/7.5	11.24
1/10	31.89
1/12.5	13.63
0	28.06

3.1. SEM and FIB analysis

All the samples were observed with a dual beam microscope in order to have a first information about the shape of the NPs and the eventual presence of impurities. Before SEM 10 μ l of the sample were put on a stub containing a piece of silica wafer attached on a dual side carbon tape, and they were left at 37°C to dry. The preparation of the sample consisted also of a step of a 10 nm coating with gold using a gold sputtering device, by employing a 30 mA current for 60 s. SEM images for this thesis project were taken with a FEI 200 operating at 15 keV, with beam currents varying from 43 pA to 0.17 nA.

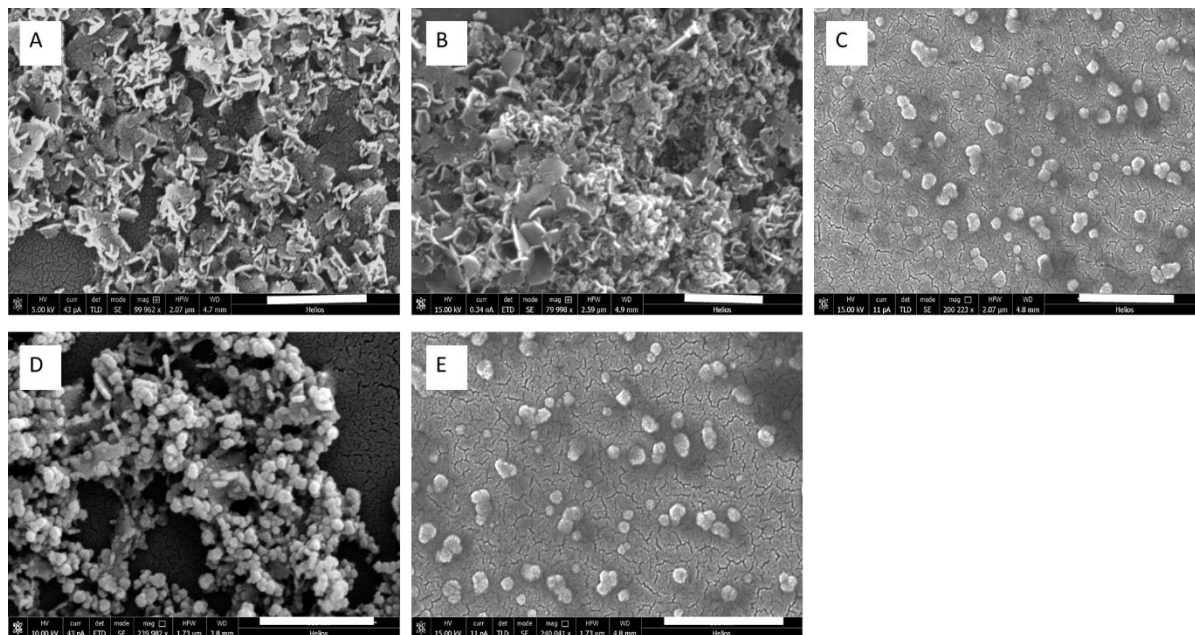


Figure 3.2 SEM images of the samples with different Mn/Fe molar ratios; the scale bar represents 500 nm. In both the samples with Mn/Fe=1/2 (A) and Mn/Fe=1/5 (B) there are many impurities. On the contrary, samples with Mn/Fe=1/7.5 (C), Mn/Fe=1/10 (D) and Mn/Fe=1/12.5 (E) show NPs.

As shown by **Figure 3.2**, the samples with a bigger quantity of manganese (Mn/Fe=1/2 and Mn/Fe=1/5) have impurities, while when there is less manganese (Mn/Fe=1/7.5, Mn/Fe=1/10 and Mn/Fe=1/12.5),

the images show the presence of NPs. Images of the sample without manganese are not presented because nanostructures were not observed.

Images with higher enlargements are presented in **Figure 3.3**: NPs are more evident in the samples with lower Mn/Fe molar ratios, while nanostructures without consistent morphology are shown in the sample with Mn/Fe=1/2. So, with this first analysis it was evident that samples without or with high quantities of manganese, in respect to the iron part, were not able to give spherical nanoparticles.

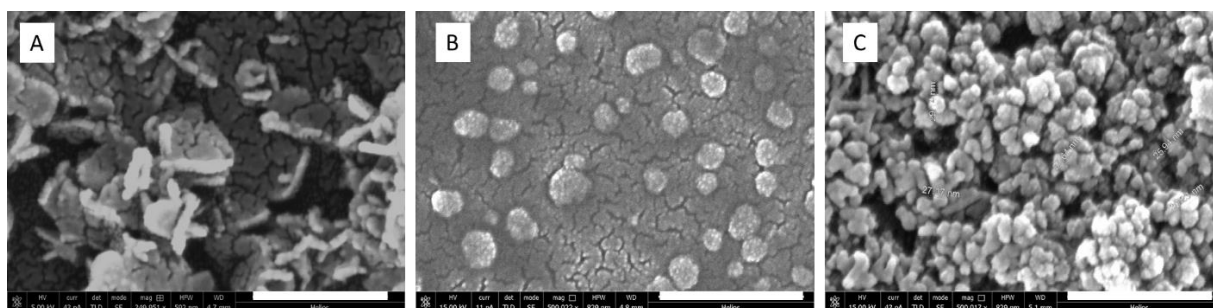


Figure 3.3 Magnified SEM images showing different nanoformulations after altering the molar ratio of Mn/Fe. More specifically: Mn/Fe=1/2 (A) shows petals (scale bar represents 200 nm), Mn/Fe=1/7.5 (B) and Mn/Fe=1/10 (C) show nanoparticles (scale bars represent 300 nm).

The images of the samples containing NPs were analyzed with the software ImageJ, in order to measure the diameter of the MANPs. At least 30 measurements from each sample were used to calculate the average and the standard deviation of the diameter; data that are reported in **Figure 3.4**. The sample with the Mn/Fe ratio equal to 1/10 showed smaller NPs, with a diameter of about 37 ± 10 nm, but in general all the MANPs had dimensions between 20 nm and 90 nm.

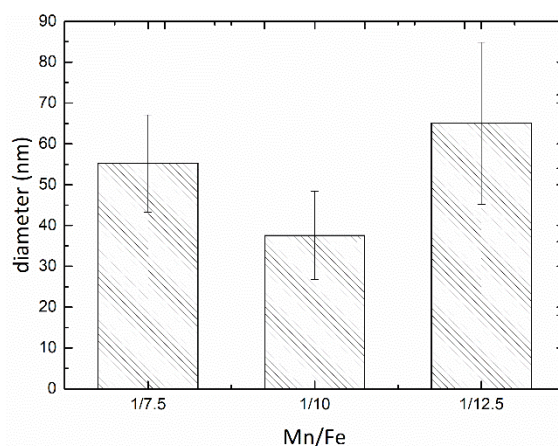


Figure 3.4 Average diameter of the NPs of the samples with Mn/Fe ratios equal to 1/7.5, 1/10, and 1/12.5. The measurements were performed with the software ImageJ.

3.2. FT-IR analysis

The FT-IR analysis was used in order to check if the desired components were created. Infrared spectroscopy for this project was performed using a Shimadzu Miracle 10. Before the measurements,

all of the samples have been freeze-dried. The number of scans was set to 45 and the resolution step was 4 cm^{-1} . The graphs were plotted using OriginPro software 9.1.

The spectra of the five samples with iron and manganese are reported in **Figure 3.5**, where the important peaks are highlighted.

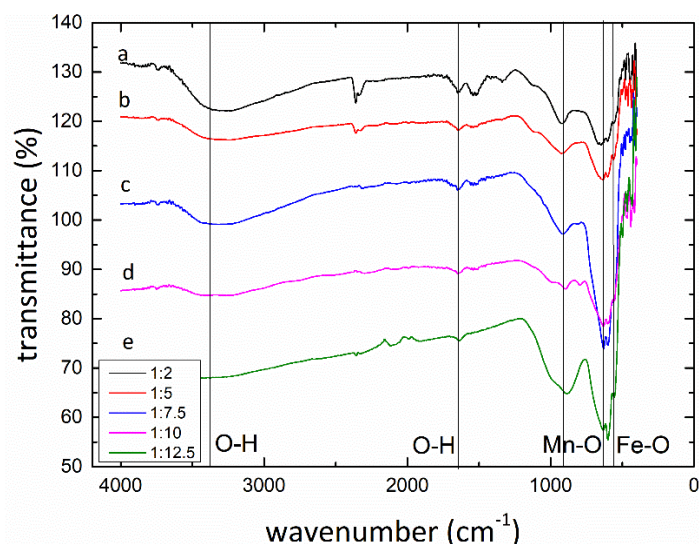


Figure 3.5 FT-IR spectra of the samples with different Mn/Fe molar ratios: 1/2 (a), 1/5 (b), 1/7.5 (c), 1/10 (d), 1/12.5 (e).

According to the literature, the FT-IR wavenumber that corresponds to the Mn-O bond is approximately at 745 cm^{-1} [97], while the one of the Fe-O bond is approximately at $592\text{--}600\text{ cm}^{-1}$ [98]. Moreover, the FT-IR spectra of the Fe_3O_4 shows peaks at 450 cm^{-1} and 582 cm^{-1} [99]. The peak at 1640 cm^{-1} can be associated with hydroxyl groups, like the band between 3380 cm^{-1} and 3440 cm^{-1} [100]. They can be probably attributed to the environmental humidity absorbed by the samples. Samples with a Mn/Fe ratio equal to 1/2 or 1/5 presents some peaks between 2300 cm^{-1} and 2400 cm^{-1} that are probably due to impurities.

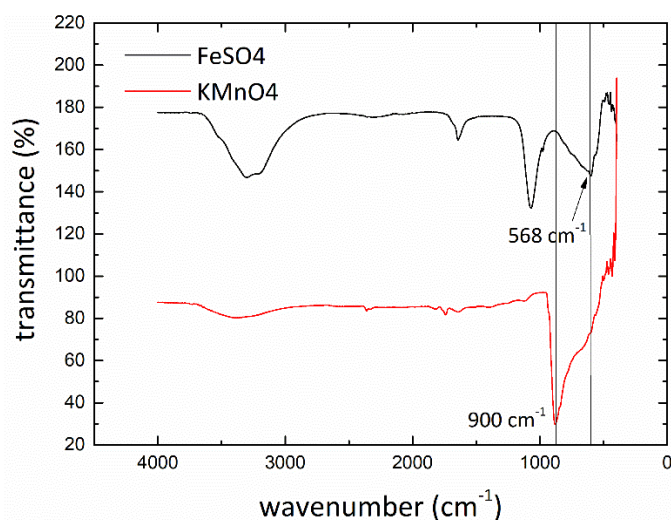


Figure 3.6 FT-IR spectra of the precursor materials used to realize the NPs: Fe_3SO_4 and KMnO_4 .

In addition, by comparing the NPs' spectra with the FT-IR analysis of the initial material FeSO₄ and KMnO₄ reported in **Figure 3.6**, it is possible to notice that the peak around 900 cm⁻¹ is due to the manganese shell, while the peak at 568 cm⁻¹ can be attributed to the iron core [101].

In conclusion, the analyses proved that Mn-O and Fe-O bonds were obtained, suggesting through Equation 18 and Equation 21 that both manganese dioxide and iron oxide were present in the final system, but again samples with a Mn/Fe molar ratio equal to 1/2 or 1/5 showed some impurities with the peaks between 2000 cm⁻¹ and 2500 cm⁻¹.

3.3. DLS analyses

The DLS measurements for this thesis project were performed with a Zeta-sizer Nano ZS90 of Malvern Instruments LTD. In the data presented, each measurement represents the average value of 3 measurements, with 15 runs for each measurement, of 1 ml of sample. Before measuring, each sample was sonicated for 1 minute by using a Bandelin ultrasonic probe at 8 W, to avoid the presence of aggregates during measurements. Different solvents, with various conductivities, were used in addition to deionized water in order to simulate and test the conditions that the NPs can find into the cell cultures or inside the human body. Therefore, Dulbecco Modified Eagle Medium (DMEM) without phenol red, DMEM without phenol red but with 10% fetal bovine serum (DMEM+10%FBS), and artificial cerebrospinal fluid (aCSF) were also employed as dispersants.

MEASUREMENTS OF THE DIFFERENT Mn/Fe RATIO SAMPLES

For the hydrodynamic diameter measurements, the concentration of the under examination samples was adjusted to 0.1 mg/ml and the temperature was set at 37°C in order to simulate the body temperature. For every Mn/Fe ratio, three solvents were used to disperse the NPs: water, DMEM and DMEM+10%FBS. Moreover, all the samples were tested at different time points: 0 h (that means after 1 min sonication), 1 h, 6 h, and 24 h after the addition of the solvent; the samples were always kept at 37°C.

In all cases (**Figure 3.7**, **Figure 3.8**, **Figure 3.9**, **Figure 3.10**, **Figure 3.11**), it is possible to observe that the solutions with DMEM showed larger hydrodynamic diameters of the NPs, while the MANPs in DMEM+10%FBS seemed to have smaller diameters. Probably this was due to the fact that the proteins of the FBS created a layer on the surface of the NPs that allowed them to be more stable and to remain separated because of the steric hindrances that prevents the NPs to aggregate, as they would do because of the Van der Waals interactions [80]. In fact, DMEM contains only inorganic salts, vitamins and amino acids, while FBS is rich of proteins, larger than amino acids and charged also at neutral pH, thus, able to cover the charged NPs' surface. As DMEM+10%FBS is a more biomimetic solvent than simple DMEM, it means that the NPs' behavior inside the body would be similar to the *in vitro* one

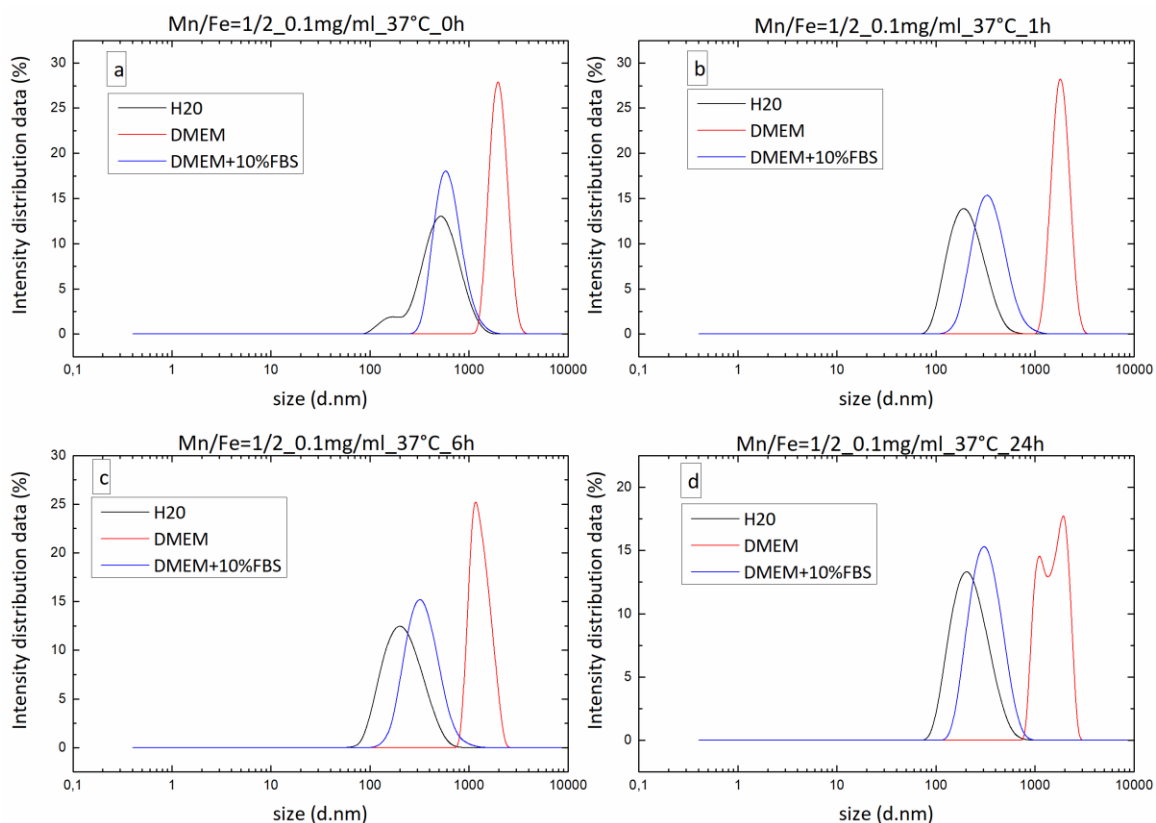


Figure 3.7 DLS measurement of the NPs with Mn/Fe=1/2 ratio. Samples with a concentration of 0.1 mg/ml were employed and tested at 37°C, with water, DMEM or DMEM+10%FBS, and at different time points: 0h (a), 1h (b), 6h (c), 24h(d).

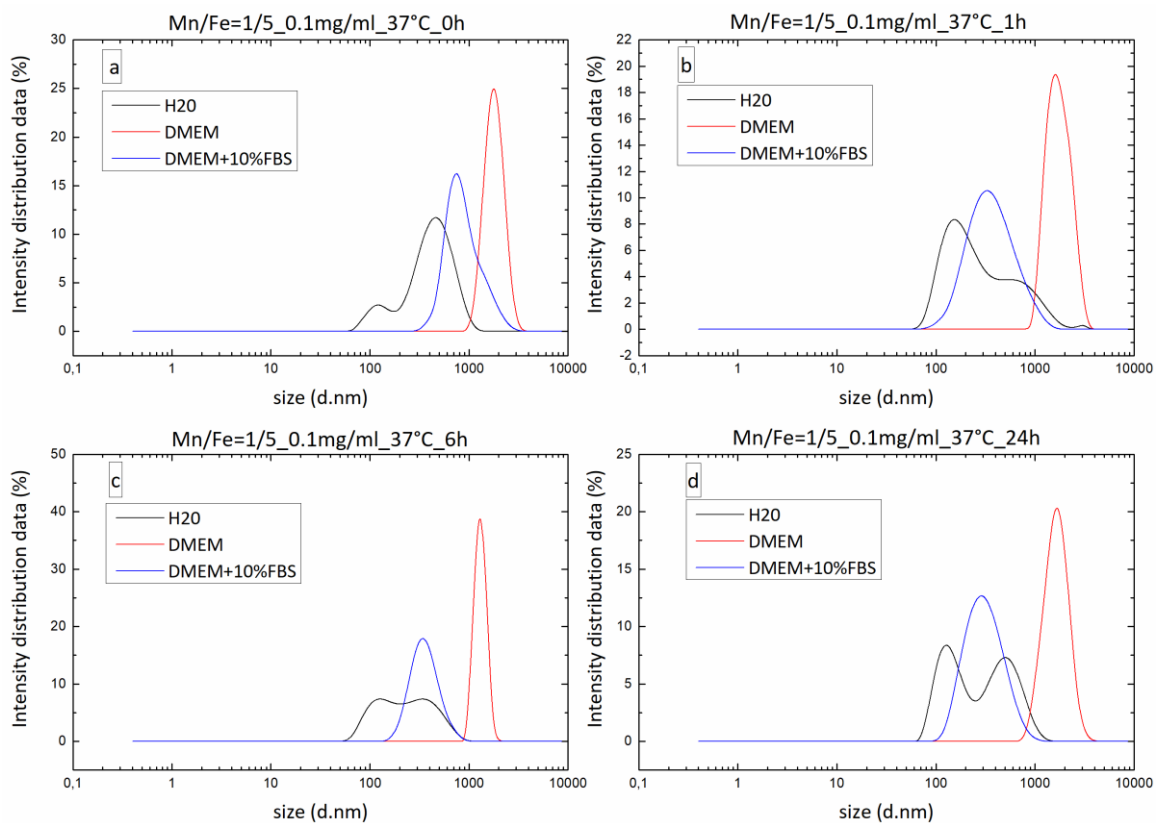


Figure 3.8 DLS measurement of the NPs with Mn/Fe=1/5 ratio. Samples with a concentration of 0.1 mg/ml were employed and tested at 37°C, with water, DMEM or DMEM+10%FBS, and at different time points: 0h (a), 1h (b), 6h (c), 24h(d).

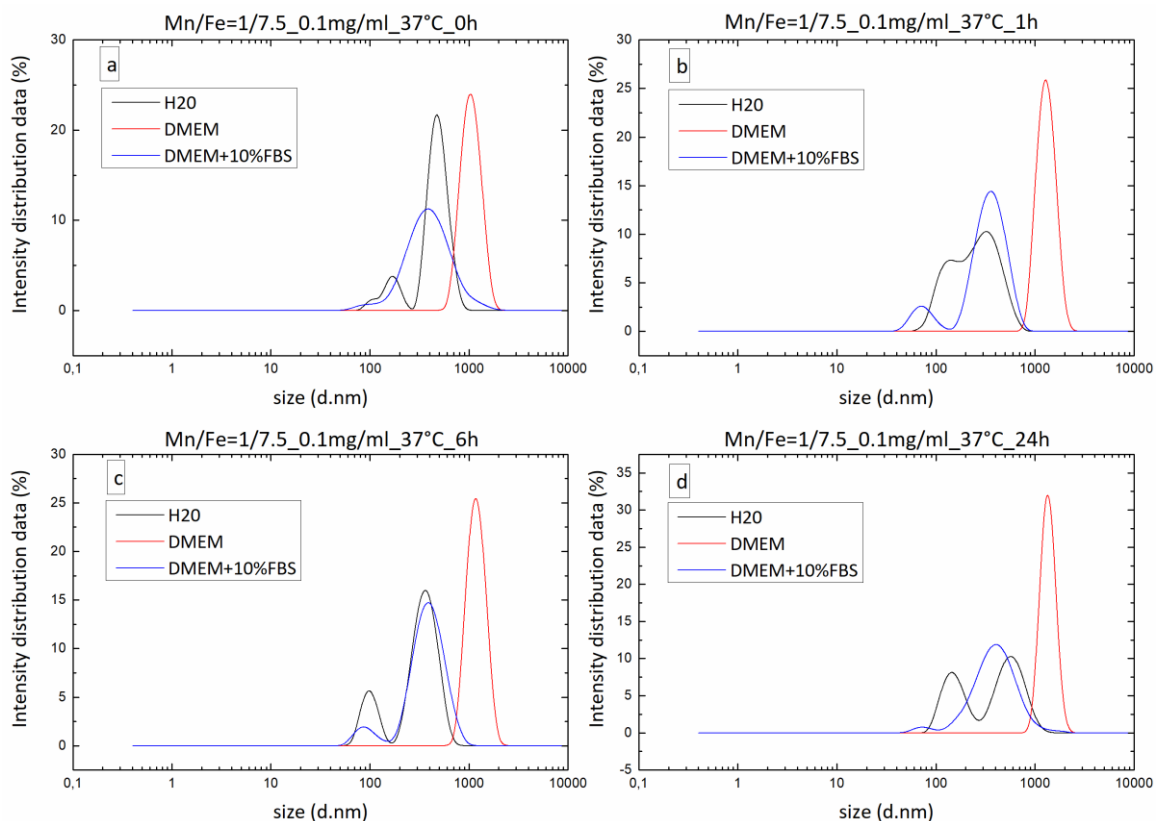


Figure 3.9 DLS measurement of the NPs with Mn/Fe=1/7.5 ratio. Samples with a concentration of 0.1 mg/ml were employed and tested at 37°C, with water, DMEM or DMEM+10%FBS, and at different time points: 0h (a), 1h (b), 6h (c), 24h(d).

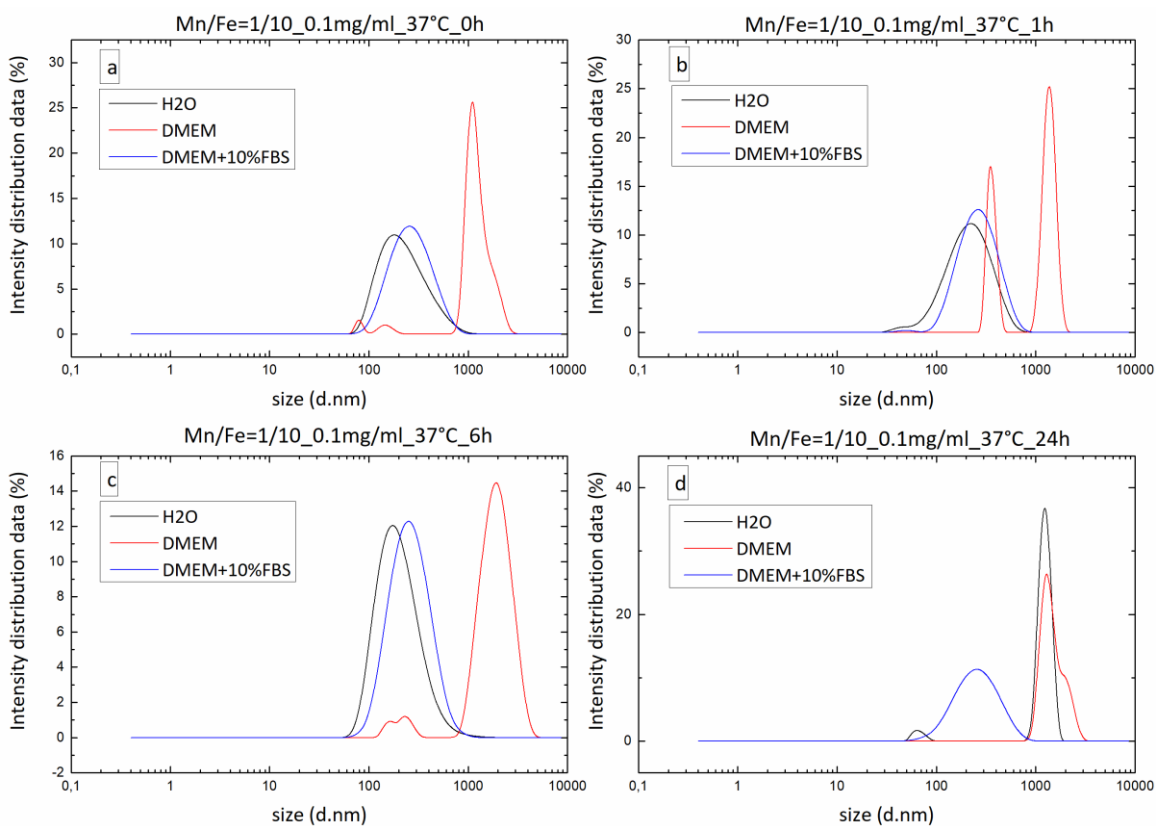


Figure 3.10 DLS measurement of the NPs with Mn/Fe=1/10 ratio. Samples with a concentration of 0.1 mg/ml were employed and tested at 37°C, with water, DMEM or DMEM+10%FBS, and at different time points: 0h (a), 1h (b), 6h (c), 24h(d).

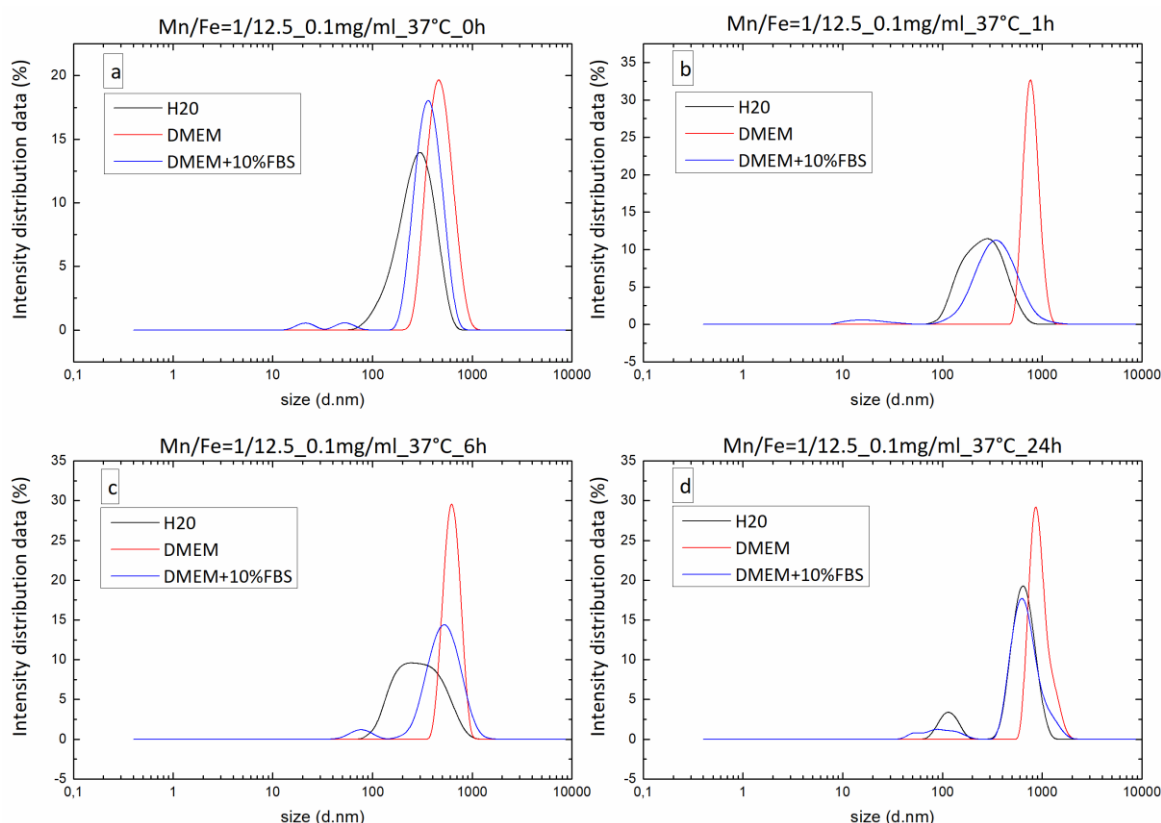


Figure 3.11 DLS measurement of the NPs with Mn/Fe=1/12.5 ratio. Samples with a concentration of 0.1 mg/ml were employed and tested at 37°C, with water, DMEM or DMEM+10%FBS, and at different time points: 0h (a), 1h (b), 6h (c), 24h(d).

with serum, and with no or small aggregates. Aggregation is a common but often neglected phenomenon when NPs are put into a liquid, but it can negatively affect the uptake by the cells and the toxicity profile of the NPs [80]. Aggregation can directly alter the cellular response because of the increased dimension of the NPs, but it can also indirectly modify it through the changed diffusion and velocities of the systems. Moreover, aggregated NPs are more inclined to be cleared by the RES and their ability to reach the desired site drastically decreases.

As shown in **Figure 3.9**, the sample with Mn/Fe ratio equal to 1/7.5 is characterized by two population with different hydrodynamic diameters of the NPs. The same behavior can also be seen in the results concerning the sample with Mn/Fe=1/12.5 (**Figure 3.11**), which presents two dimensional populations when in DMEM+10%FBS. These samples had also the highest polydispersity indexes (PDI) (**Table 3.3**). All these data together suggest that probably inside the samples with a molar ratio Mn/Fe equal to 1/7.5 and 1/12.5 there are two size populations of NPs.

Table 3.3 Polydispersity indexes (PDI) of the NPs with different Mn/Fe ratios solubilized in DMEM+10%FBS and at various time points (0h, 1h, 6h, and 24h). The lowest PDI are attributable to the samples with the highest amount of manganese.

Mn/Fe	1/2	1/5	1/7.5	1/10	1/12.5
0h	0.248	0.239	0.442	0.225	0.492
1h	0.157	0.253	0.529	0.210	0.498
6h	0.138	0.129	0.414	0.223	0.541
24h	0.158	0.196	0.409	0.207	0.524
average	0.175	0.204	0.449	0.216	0.514

Hydrodynamic diameters of the MANPs in DMEM+10%FBS are reported in **Figure 3.12**. Various time points were considered, and it is evident that at time zero the hydrodynamic diameter was bigger than the one after 1 h. This happened in almost all samples (with the exception of the sample with Mn/Fe = 1/10, whose hydrodynamic diameter was stable during all the measurements), but with a different entity of the variations. Systems with a higher amount of manganese (Mn/Fe = 1/2 or Mn/Fe = 1/5) almost halved their hydrodynamic diameters in the first hour, while samples with less manganese showed a smaller variation. This decrease was probably due to the fact that when the NPs were dispersed in a complex medium such as DMEM with FBS, the ionic strength of the solvent made the NPs aggregate. But then the proteins of the serum created a layer on the NP's surface, by separating them and consequently the hydrodynamic diameter decreased.

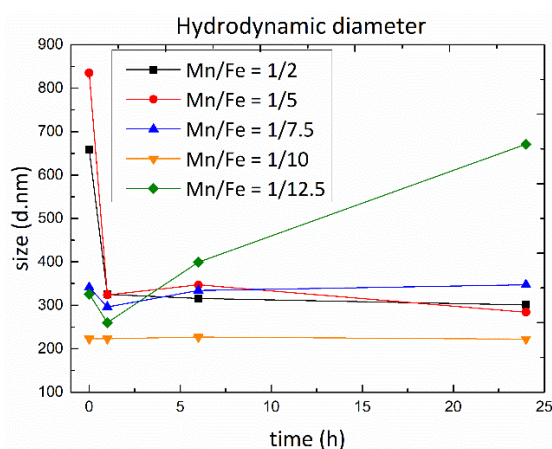


Figure 3.12 Hydrodynamic diameters of the MANPs with different Mn/Fe ratios, solubilized in DMEM+10%FBS and measured at various time points (0h, 1h, 6h, and 24h)

Between 1h and 24h, the hydrodynamic diameter remained almost constant in all the samples, with the exception of the Mn/Fe=1/12.5 system, in which the dimension increased again and strongly exceeded the initial hydrodynamic diameter, probably because of the aggregation of the NPs.

The correlation graphs of all the systems are reported in the Appendix. Correlograms were obtained with the same conditions as the intensity graphs. They confirmed the fact that the NPs created agglomerates in DMEM more than what they did in DMEM+10%FBS. Indeed, the DMEM plots show bigger oscillations when the correlation coefficient decreased.

Finally, the Z-potential of the NPs must be considered. The Z-potential measurements were carried out in deionized water at 37°C and the conductivity was adjusted at the range of 10-100 $\mu\text{S}/\text{cm}$. The attenuation of the samples during measurements was approximately 7. The surface charge measurements represent the mean \pm SD of 3 different measurements with 15 runs for each of them.

The dependence of the Z-potential on the concentration of the sample and on the temperature was assessed (**Table 3.4**) by measuring the same system with 3 different concentration and both at 25°C and at 37°C. Then, the same concentration and temperature conditions were employed to measure all the samples of interest.

Table 3.4 Dependence of the Z-potential on the concentration of the NPs and on the temperature.

sample	concentration (mg/ml)	temperature (°C)	z-potential (mV)
Mn/Fe=1/10	0.1	25	-26,1
Mn/Fe=1/10	0.01	25	11,5
Mn/Fe=1/10	0.001	25	12,6
Mn/Fe=1/10	0.1	37	-20,2

The systems with different Mn/Fe ratios were measured at various time points: 0h, 1h, 6h, and 24h. The results are reported in **Table 3.5**. First of all, it has to be noted that the MANPs are charged and this is extremely useful because it increases their probability to be uptaken by the cells, but most of all it lets the NPs interact with proteins (see Section 6.4) and have a higher stability inside the bloodstream.

Table 3.5 Z-potential of the NPs in the first 24h, measured in water at 37°C and with a concentration equal to 0.1mg/ml

Mn/Fe	1/2	1/5	1/7.5	1/10	1/12.5
0h	-41 mV	-23 mV	-17 mV	-20 mV	-24 mV
1h	-31 mV	-25 mV	-24 mV	-18 mV	-24 mV
6h	-29 mV	-24 mV	-21 mV	-24 mV	-25 mV
24h	-23 mV	-20 mV	-16 mV	-12 mV	-19 mV
average	-31 mV	-23 mV	-19 mV	-19 mV	-23 mV
standard deviation	6.3 mV	1.8 mV	3.1 mV	4.3 mV	2.1 mV

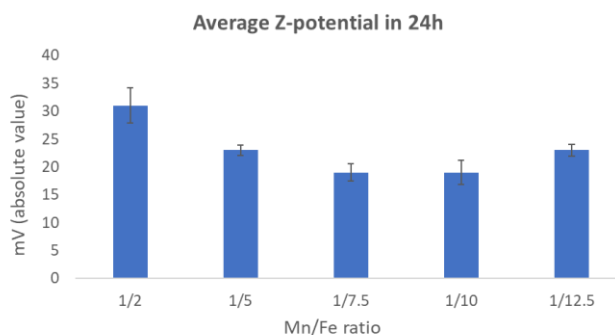


Figure 3.13 Absolute value of the average Z-potential during the first 24h, measured in deionized water at 37°C and with a concentration equal to 0.1mg/ml

In addition, it should be taken into account is that the absolute modulus of the NPs is in general a bit lower than the theoretical threshold of 30 mV, as MANPs are on the edge of stability in deionized water, because of what abovementioned in the DLS theory (Section 2.2), but MANPs are very small, so they do not need such high values of Z-potential to be stable.

In conclusion, by taking into consideration all the analyses realized for the systems with different Mn/Fe ratios (SEM, FT-IR and DLS), the sample with Mn/Fe=1/10 was chosen as the system for further analyses. In fact, SEM images were useful to understand that an amount of manganese not too high neither too low was the condition to create NPs, FT-IR confirmed that the desired compounds were obtained without impurities for the Mn/Fe=1/10 sample, and the DLS measurements showed the absence of aggregates and the presence of only one dimensional population in this system. Moreover, the same choice could be done by exclusion of the other samples. Indeed, the system without manganese did not show any kind of nanostructures at SEM, while Mn/Fe ratios equal to 1/2 and 1/5 led to the presence of impurities. Among the remaining samples, the sample with a molar ratio of Mn/Fe=1/10 showed NPs with the smallest size. FT-IR analyses confirmed the presence of probably unreacted KMnO_4 for the systems with the Mn/Fe ratio equal to 1/2 and 1/5. Then, the samples with 1/7 and 1/12.5 material ratios were excluded because they presented more than one population in the DLS measurements. Finally, the abnormal behavior regarding the increase of hydrodynamic diameter of the sample with the lowest amount of manganese proved that this system had not the desired properties. Given all these considerations, the subsequent characterizations were run only for the sample with the Mn/Fe molar ratio equal to 1/10.

DLS STABILITY STUDY

In order to check the stability of the MANPs with the optimized quantity of manganese, complementary DLS measurements were performed. In this case, only deionized water was used as solvent, because aqueous solutions are the best ones to quantify the colloidal stability of a system [80]. The data were collected at different temperatures, in order to simulate all the temperature conditions in which the NPs could come across. Thus, room temperature (25°C), body temperature (37°C), hyperthermia temperature (42°C) and maximum temperature for the healthy cells (46°C) [102] were tested. At the end of this cycle, the system was measured again at 25°C, in order to understand if the temperature changes its colloidal stability. Moreover, for every temperature condition, various time points were studied: 0 min, 30 min, 60 min, 90 min, and 120 min.

The results presented in **Figure 3.14** demonstrate that the system was stable and only one population of NPs was present, concerning the size. Moreover, the temperature changes seemed not to affect the MANPs' behavior. The hydrodynamic diameters and the PDI recorded during the stability study are

shown in **Table 3.6**. The hydrodynamic diameter slightly increased with temperature, but in general it remained around 205 nm \pm 105 nm. This high value, if compared to SEM and TEM results, could be due to the formation of small aggregates. The PDI was constant and approximately around 0.246.

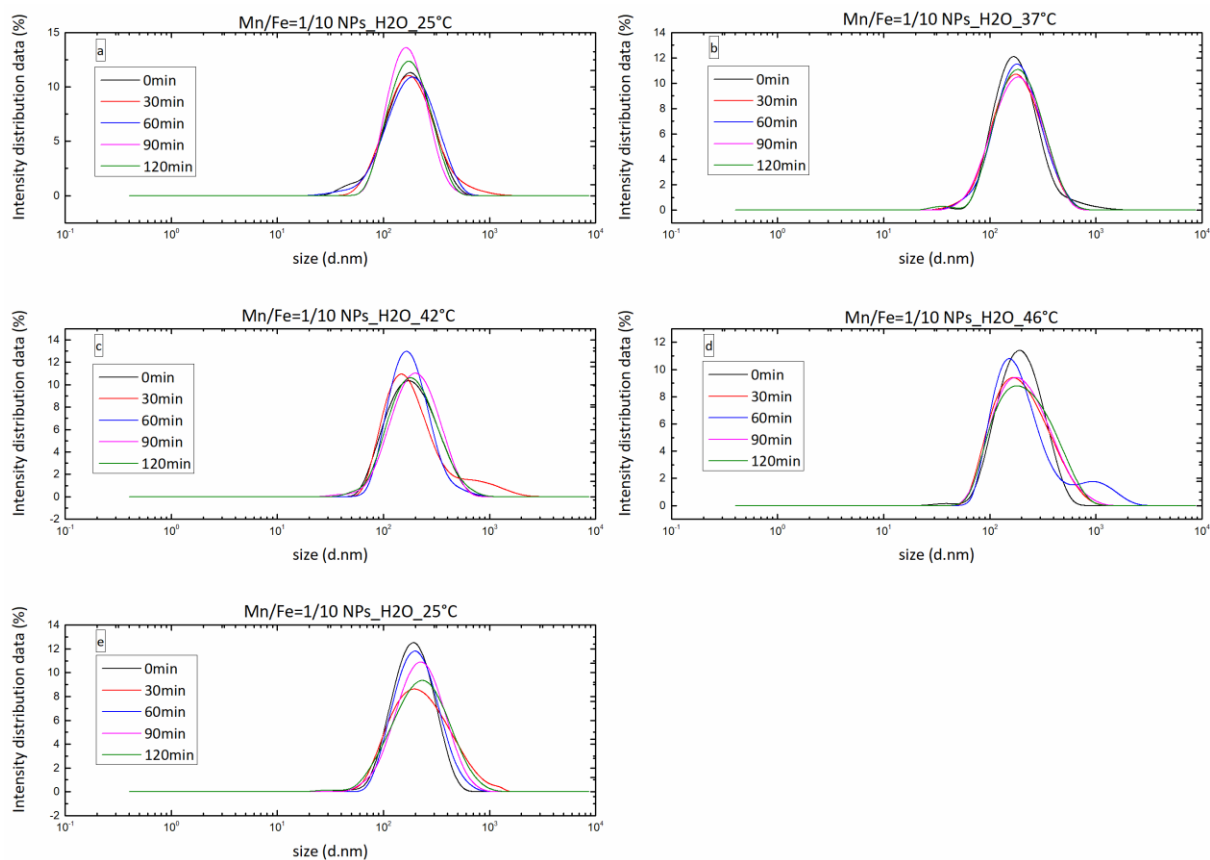


Figure 3.14 DLS stability study of uncoated MANPs. The measurements were run in water, at different temperatures: a) 25°C, b) 37°C, c) 42°C, d) 46°C, e) then again 25°C. For each temperature various time points (0, 30, 60, 90, 120 min) were considered.

Table 3.6 Hydrodynamic diameter and PDI of the uncoated MANPs during the DLS stability study

Temperature (°C)	Hydrodynamic diameter (nm)	PDI
25	189.5 \pm 92.8	0.241
37	208.3 \pm 137.5	0.254
42	208.0 \pm 109.6	0.253
46	213.1 \pm 98.7	0.235
25	206.4 \pm 88.2	0.247

MEASUREMENTS WITH aCSF

Once in the body, the MANPs could enter in contact with different fluids: not only the blood, but also the cerebrospinal fluid (CSF). Therefore, the NPs' behavior was tested in environment simulating the CSF. In order to achieve this simulation, artificial CSF (aCSF) was realized using materials and quantities given in **(Table 3.7)** by following a protocol from Alzet® corporation. First of all, 200 ml of deionized water were kept in the incubator one day in order to increase the CO₂ content. Briefly, 100 ml of an

aqueous solution A containing 296.58 mM sodium chloride (NaCl), 6.009 mM potassium chloride (KCl), 2.803 mM calcium chloride dihydrate ($\text{CaCl}_2 \cdot 2\text{H}_2\text{O}$), and 6.03 mM magnesium chloride hexahydrate ($\text{MgCl}_2 \cdot 6\text{H}_2\text{O}$) were prepared. Then, 1.597 mM disodium hydrogen phosphate heptahydrate ($\text{Na}_2\text{HPO}_4 \cdot 7\text{H}_2\text{O}$) and 0.391 mM sodium dihydrogen phosphate monohydrate ($\text{NaH}_2\text{PO}_4 \cdot \text{H}_2\text{O}$) were solubilized in 100 ml of deionized water (solution B). Solutions A and B were combined in a 1:1 ratio only when needed and they were stored at 4°C.

Table 3.7 Components and quantities of the Alzet® aCSF

Solution	Substance	Concentration
A	NaCl	296.58 mM
A	KCl	6.009 mM
A	$\text{CaCl}_2 \cdot 2\text{H}_2\text{O}$	2.803 mM
A	$\text{MgCl}_2 \cdot 6\text{H}_2\text{O}$	6.03 mM
B	$\text{Na}_2\text{HPO}_4 \cdot 7\text{H}_2\text{O}$	1.597 mM
B	$\text{NaH}_2\text{PO}_4 \cdot \text{H}_2\text{O}$	0.391 mM

As previously noticed with the DMEM, also when using the aCSF without or with 10% FBS the NPs changed behavior (**Figure 3.15**). In particular, when the FBS is added, the hydrodynamic diameter decreased because of the protein layer on the surface of the NPs that did not allow the aggregation.

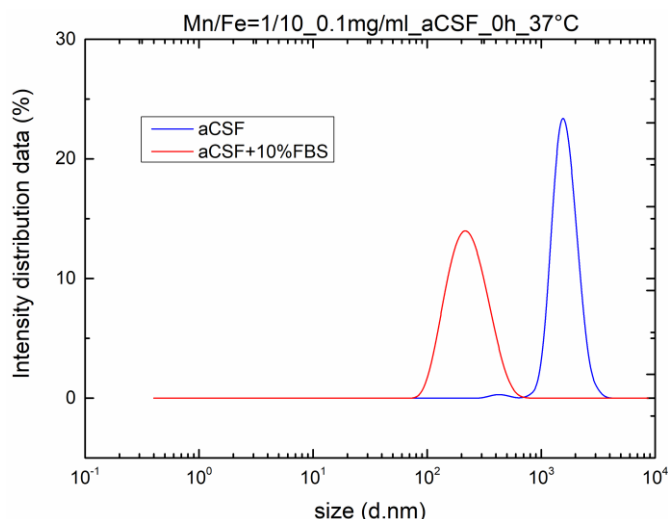


Figure 3.15 DLS measurements of the uncoated MANPs in aCSF and aCSF+10%FBS at 37°C

3.4. TEM analysis

The sample, that was previously diluted with milliQ water, was sonicated for few minutes and drop-casted onto a 150 mesh carbon coated copper grid. Before the sample deposition each grid was plasma-treated ($\text{O}_2 + \text{Ar}$ plasma, 15 W, 2 minutes) in order to remove hydrocarbon residues from carbon

film deposition. HAADF-STEM/EDS analyses for this thesis were performed using an FEI Tecnai G2 F20 TWIN TMP with a Schottky emitter operated at 200 kV.

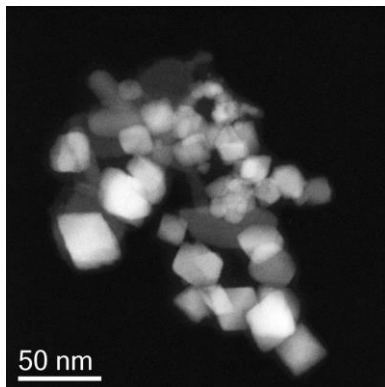


Figure 3.16 TEM image of the uncoated Mn/Fe=1/10 NPs: they are cubes.

Thanks to the higher resolution of TEM image shown in **Figure 3.16**, the shape of the NPs was better understood, and in fact it has been observed that instead of a spherical, the nanoparticles have a cubic structure. This cubic structure can be considered advantageous compared to the respective spherical form of some nanoparticles because nanocubes present a higher degree of crystallinity than nanospheres, resulting in enhanced magnetic properties [103]. In fact, they present higher saturation magnetization and higher coercivities, as well as increased surface contact area, compared to respective spherical nanoparticles.

3.5. XRD analysis

The crystal structure of the MANPs was investigated through XRD measurements at 25°C. The diffraction patterns of the NPs were obtained using a Phillips X'pert PRO X-ray diffractometer, with θ - 2θ geometry, under the following conditions: CuK α radiation ($\lambda = 1.5418 \text{ \AA}$); scans in the 2θ range of $10 - 80^\circ$ with a current of 40 mA, a voltage of 40 kV, and a scan rate of $2.8^\circ/\text{min}$.

Almost all the visible peaks in the graph in **Figure 3.17** are attributed to the magnetite structure. In fact, they are observable at 2θ values equal to 18° , 30° , 35° , 37° , 43° , 54° , 57° , 63° , 71° , and 74° , and correspond to (111), (220), (311), (222), (400), (422), (511), (440), (620), and (533) planes, as presented in Table 3.8 [75]. In the same spectrum the manganese dioxide presence is revealed by the peaks at 38° , 62° and 74° . Moreover, the peaks at 40° , 62° and 74° cannot be associated either with the magnetite or the manganese dioxide structure, but they can be attributed to hydroxides of iron oxide suggesting the existence of a second phase, except magnetite, in the MANPs.

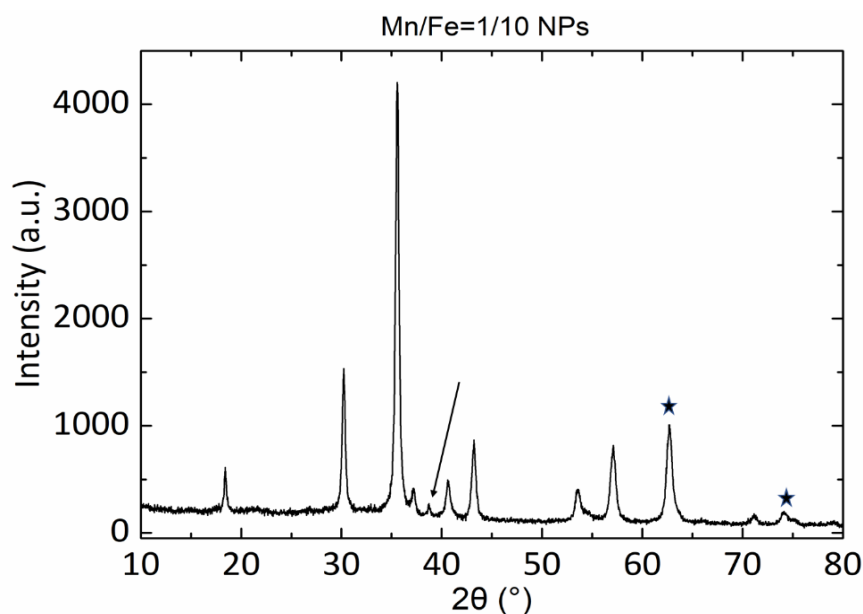


Figure 3.17 XRD spectrum presenting the peaks of the MANPs. The majority of the peaks are attributable to the magnetite (Fe_3O_4) structure, while the arrow underlines the structure of ramsdellite (MnO_2). The peaks with stars can be attributed to the presence of an iron oxide hydroxide (FeOOH).

Table 3.8 Correspondence between the 2θ values of the peaks and the crystal planes.

2θ	Crystal lattice
18°	111
30°	220
35°	311
37°	222
43°	400
54°	422
57°	511
63°	440
71°	620
74°	533

By using the Scherrer equation (Equation 4), it is possible to calculate the dimension of the crystals inside the material using the following parameters:

$$K = 0.94$$

$$\lambda = 1.5418 \text{ \AA}$$

The angles (θ) were expressed in radiant, instead of using degree as unit of measurement. The four highest peaks of the XRD pattern were employed to perform the calculations, while the “Multiple peak fit” analysis tool of OriginPro 9.1 was used to measure the peaks’ width at half height; the results are reported in **Table 3.9**. After the calculations it was found that the magnetite crystals have an average dimension of 18.31 nm, suggesting that the MANPs are almost monocrystalline since the size of their crystals is similar to their size as measured by TEM.

Table 3.9 Scherrer equation's results for the biggest peaks of the XRD pattern.

2θ	$B (\theta)$	$d (\text{Å})$
30°	0.40685	211.301
35°	0.43986	197.945
43°	0.47291	188.722
63°	0.72198	134.892

3.6. EDS analysis

EDS spectroscopy was used to further evidence the elemental composition of MANPs. The EDS analyses that are presented in **Figure 3.18** have been acquired using a Bruker XFlash 6|T30 silicon-drift detector (SDD), with 30 mm² effective area.

In the image it can be observed an increased density of red (**Figure 3.24-A2**) and yellow spots (**Figure 3.24-A3**), that correspond to Fe and Mn, accordingly, only where particles are observed (**Figure 3.24-A1**). The colocalization of iron and manganese presented in Figure 3.24-A4 as well as the quantification from the EDS spectrum presented in **Figure 3.18** and the results in the map show that the iron represents almost 90% of the samples, while manganese only 10%, further proving that the initial molar ratio Fe/Mn = 1/10 that it was used, was also the same to the final material.

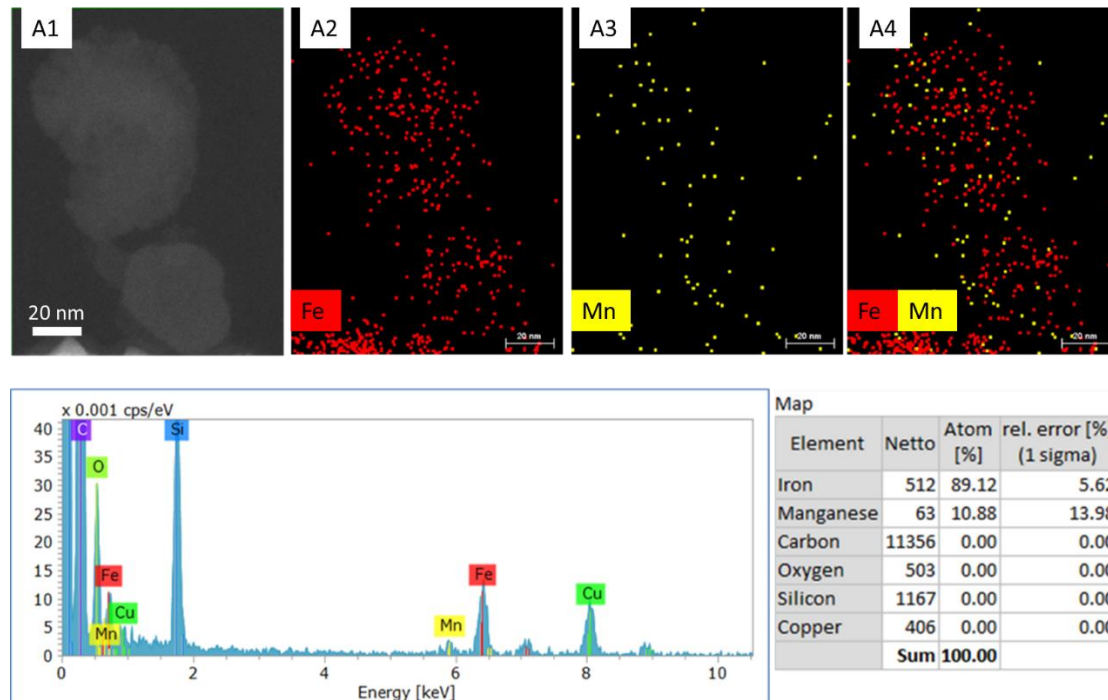


Figure 3.18 EDS analysis of the uncoated MANPs.

3.7. ICP analysis

ICP analysis was performed using an iCAP 6500 Thermo spectrometer and was used in order to have a more accurate analysis, concerning the chemical composition of the MANPs. All chemical analyses for

MANPs that were performed by ICP-AES were affected by a systematic error of about 5%. All samples before measurement were dissolved in HCl/HNO₃ 3:1 (v/v).

ICP results demonstrated that the desired Mn/Fe molar ratio was obtained, since the manganese presence was quantified as 6.10% (**Table 3.10**), which was almost the 1/10 of the iron, that was found to be 67.20%.

Table 3.10 ICP results: percentages and ppm of iron and manganese in the sample.

Element	Percentage	ppm
Fe	67.20	141.7
Mn	6.10	14.64

3.8. BET analysis

The BET specific surface area (BET SSA) of the specimen was determined using adsorption of Nitrogen (high purity grade). Nitrogen physisorption measurements were performed at 77 K (-196°C) using a Quantachrome Autosorb-6B unit gas adsorption analyzer and an equilibration time of 3 min (a data point is considered in equilibrium when the pressure varies less than 80 Pa in 3 min). The sample, 0.0774 g of powder, was pretreated ex-situ for 24 h under vacuum at 473 K before the adsorption measurements.

BET's most important results are reported in **Table 3.11**. The interparticle surface area was found to be 18 m²/g, a high value if compared with the specific surface area of other magnetite nanostructures found in literature (13.53 m²/g for hollow spheres [104] or even 8.3 m²/g for dense nanoparticles [105]). BET provide information also for the pore diameter of the MANPs which was 3 nm, suggesting that the loading of small drug molecules like temozolomide could be achieved.

Table 3.11 BET results: surface area and dimension of the pores of the MANPs.

Interparticle surface area	18 m ² /g
Mesopores diameter	2-3 nm

According to 1985 IUPAC recommendations [106], the isotherm reported in **Figure 3.19** is a Type III graph. There is not identifiable monolayer formation since here there is not the Point B typical of Type II isotherms. The adsorbent-adsorbate interactions are quite weak, and the adsorbed molecules are clustered around the most favorable sites on the surface of the porous NPs [107]. The amount adsorbed remains finite at the saturation pressure, that here is P/P₀=1. The hysteresis is a Type H3 loop and it is associated with capillary condensation [108]. In **Figure 3.20**, the adsorption and desorption graphs are shown.

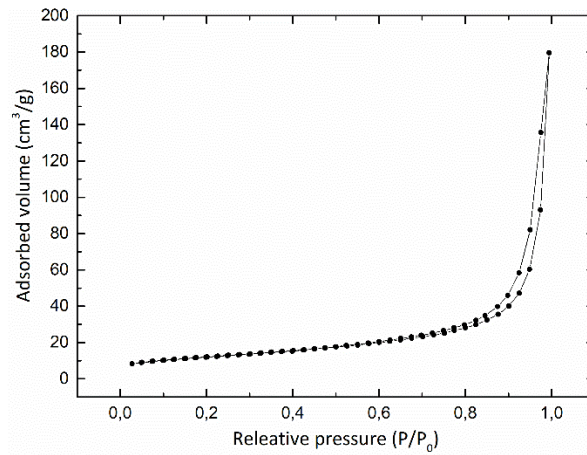


Figure 3.19 Isotherm graph for the MANPs.

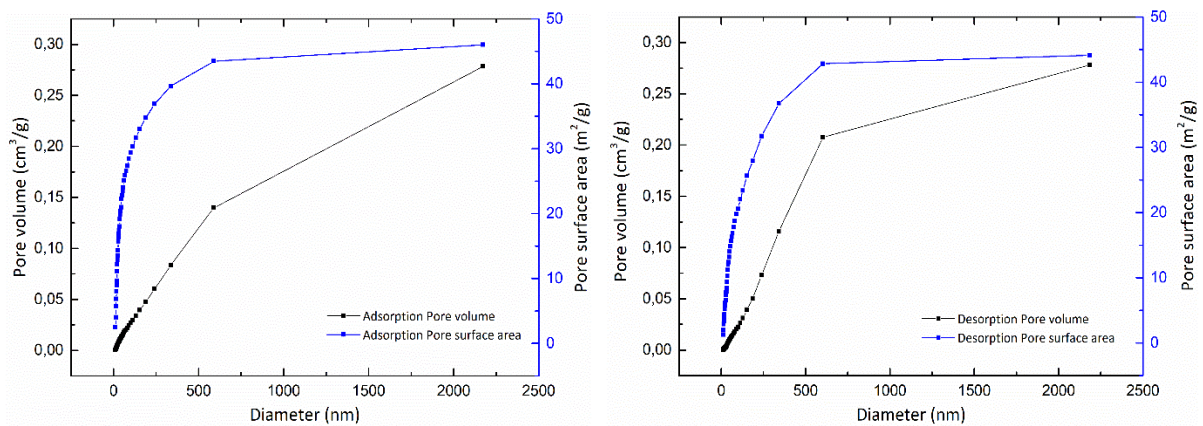


Figure 3.20 Adsorption (on the left) and desorption (on the right) graphs for the MANPs.

3.9. Magnetic measurements: VSM and NMR

Quasi-static hysteresis loops were recorded at room temperature, by using an Oxford Instruments 1.2H/CF/HT vibrating sample magnetometer with a field ranging from -1 to 1 T.

The graph of the magnetization as function of the field is reported in **Figure 3.21**. The results show a high coercivity of about 0.0185 T (185.413 Oe), which is higher compared to other similar systems presented in literature [104]. This could be considered a drawback since it can result to an aggregation of the MANPs, due to the magnetic dipole-dipole attractions [109], but it can also be considered as an advantage since the higher is the coercivity, the higher are the specific absorption rate (SAR) values [110]. The SAR is important to understand the rate at which energy (electromagnetic, ultrasound, etc.) is absorbed by the human body and it is the power absorbed per mass of tissue (W/kg). In this project, SAR values are taken into account considering the system exposed to a radio frequency electromagnetic field. From the graph presented in Figure 3.28 we can also calculate the the saturation magnetization (M_s) which is around 57 emu/g, a value that is similar to other nanoparticles presented in literature[110].

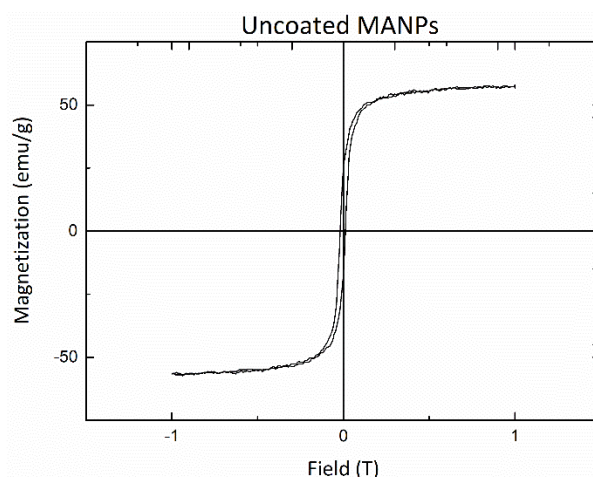


Figure 3.21 M-H graph of the uncoated MANPs, showing the high saturation magnetization and the big coercivity.

The NMR relaxometry measurements for this thesis were performed by using a Spectrometer Stellar Spinmaster, with an uncertainty in the values of relaxation equal to 8%.

The frequency and the magnetic field working range were similar with the ones covered by the clinical imaging systems. Indeed, the Larmor frequencies employed and reported in **Table 3.12**, correspond to magnetic fields equal to 0.2 T, 0.5 T and 1.3 T. Measuring the relaxation times, an estimate of the efficiency of the MANPs to be used as contrast agent was evaluated, by employing milliQ water as host solution. The results that are presented in

Table 3.13, show r_2 values (ranging from approximately 175 to 185 $s^{-1}mM^{-1}$), that are higher compared to the r_2 value of the commercial T2 contrast agent Endorem® (see Section 1.3.) which presents a nuclear relaxivity around 100 $s^{-1}mmol^{-1}L$ [111], suggesting the potential use of the MANPs as MRI contrast agents.

Table 3.12 Larmor frequencies employed for the NMR measurements and the equivalent magnetic field intensities.

Larmor frequency	Magnetic field intensity
8.5 MHz	0.2 T
21 MHz	0.5 T
57 MHz	1.3 T

Table 3.13 Results of the NMR relaxometric measurements, where both the relaxation times (T1 and T2) and nuclear relaxivities (r_1 and r_2) are reported.

Frequency	T1	r_1	T2	r_2
[MHz]	[ms]	[$s^{-1}mmol^{-1}L$]	[ms]	[$s^{-1}mmol^{-1}L$]
8.5	137	17.64±1.41	13.9	182.13±14.57
21.29	333	6.86±0.55	13.7	184.79±14.78
56.7	999.7	1.77±0.14	14.5	174.60±13.96

4. Antioxidant properties

Since the main hypothesis concerning the manganese shell of the NPs was its ability to scavenge the overproduced ROS, in particular H_2O_2 , and to subsequently reduce the oxidative stress, experiments proving its scavenging ability were performed.

The antioxidant measurements were realized by using an ABTS Antioxidant Assay Kit by Zen-Bio, Inc. The antioxidant ability of the MANPs was compared with the antioxidant ability of Trolox (6-Hydroxy-2,5,7,8-tetramethylchroman-2-carboxylic acid) which is a water soluble analogue of vitamin E (**Figure 4.1**), known for its antioxidant capacity. The assay measures the ABTS (2,2'-azino-bis(3-ethylbenzthiazoline-6-sulfonic acid) radical cation formation induced by metmyoglobin and hydrogen peroxide. Ferryl myoglobin radicals are formed from metmyoglobin and hydrogen peroxide. They can oxidize ABTS to generate radical cations, ABTS⁺, that are green in color and whose absorbance at 405 nm can be measured using UV-VIS spectroscopy. Antioxidants can suppress this reaction by electron donation radical scavenging, and inhibit the formation of the colored ABTS radical, resulting to a colorless solution.

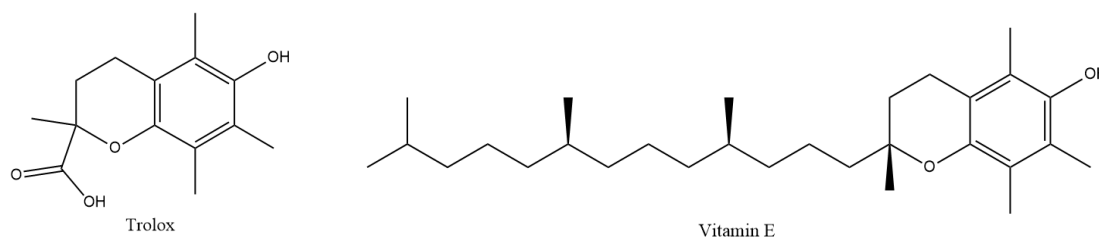


Figure 4.1 Chemical structures of Trolox and Vitamin E

Two concentrations of the uncoated Mn/Fe=1/10 MANPs were tested: 100 $\mu\text{g/ml}$ and 500 $\mu\text{g/ml}$ (**Figure 4.2**).

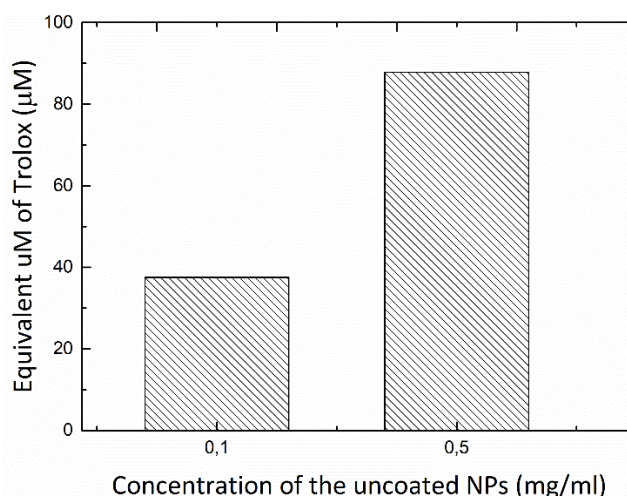


Figure 4.2 Antioxidant measurements for two concentrations of uncoated NPs: 100 $\mu\text{g/ml}$ and 500 $\mu\text{g/ml}$.

The used protocol was as described by the ABTS Antioxidant Assay Kit instructions. After the reaction of the MANPs with the ABTS solution, the MANPs were spun down for 1 min and the supernatants were transferred to a 96 well plate and their absorbance was analyzed by using a PerkinElmer Victor 2030 plate reader at 405 nm.

As the hydrogen peroxide scavenging activity of manganese represents an exothermic reaction, the temperature increase of MANPs' solutions when H₂O₂ was added was recorded, by employing various uncoated NPs concentrations (0.5 mg/ml, 1 mg/ml, 2.3 mg/ml, and 4.6 mg/ml). Moreover, various H₂O₂ concentrations were used during the measurements. A first test involved the highest concentrations of both solutions. After 10 min of temperature recording of a 9.2 mg/ml MANPs dispersion (1 ml) under magnetic stirring, 1 ml of H₂O₂ 10M was added, always keeping the solution on the stirrer. The temperature in the final solution immediately increased from 27.2 °C to 66.4°C (**Figure 4.3-a**), suggesting that the system was properly working as a ROS scavenger. It has to be pointed out that 20-30 min after the H₂O₂ addition the temperature returned to the initial one. The same procedure was applied also to realize a final 2 ml solution with 1 mg/ml MANPs and H₂O₂ 1M. In this case, there was an increase of 5°C, from 26°C to 31°C, but again the initial conditions were restored after around 30 min.

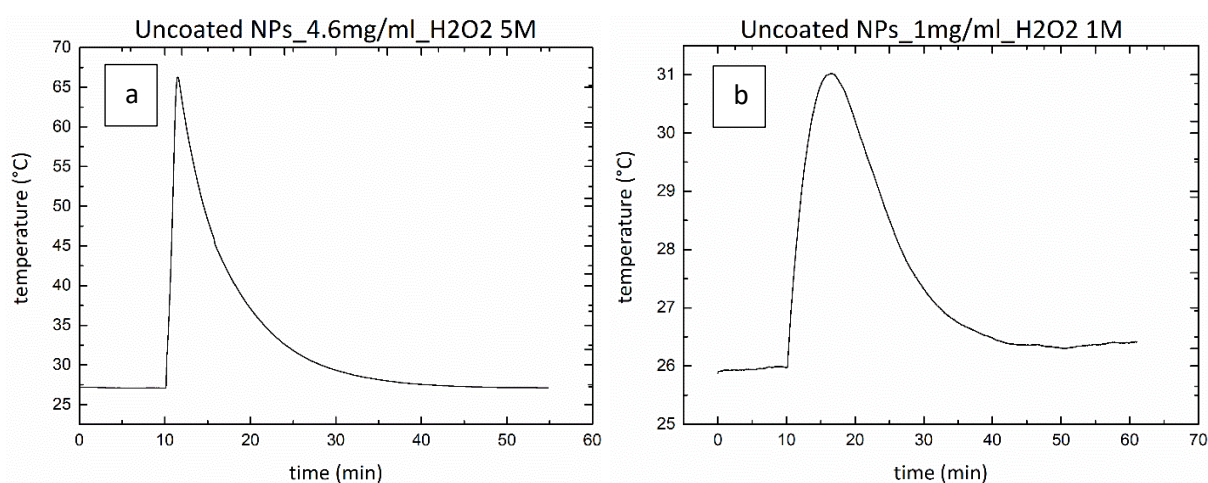


Figure 4.3 Temperature increase in 2 ml solutions of 4.6 mg/ml (a) or 1 mg/ml (b) of uncoated MANPs and H₂O₂ 5M (a) or 1M (b). The H₂O₂ was added at min 10.

Since in cancerous tissues the concentration of H₂O₂ is about 100 μM [112], experiments using this specific amount of H₂O₂ as well as MANPs have been carried out. Unfortunately, due to limitations of the temperature sensor an increase in temperature could not be observed. Nevertheless, experiments using higher concentrations of H₂O₂ were performed, firstly to study the profile of temperature increase when different concentrations of H₂O₂ and MANPs are used, and secondly to see if it was possible to take advantage of this reaction in order to increase the temperature and kill the cancer cells by exploiting this ROS responsive system.

In order to understand if the temperature increase was detectable also with small volumes, more representative of the body environment, final solutions of 100 μ l were tested. The results are reported in **Figure 4.4**. When H₂O₂ 100mM was added, the maximum temperature increase was 0.5°C: this was an advantage because it can contribute to the hyperthermia treatment, but the temperature increase due to the ROS scavenging action was not enough high to become an uncontrolled and unmanageable effect.

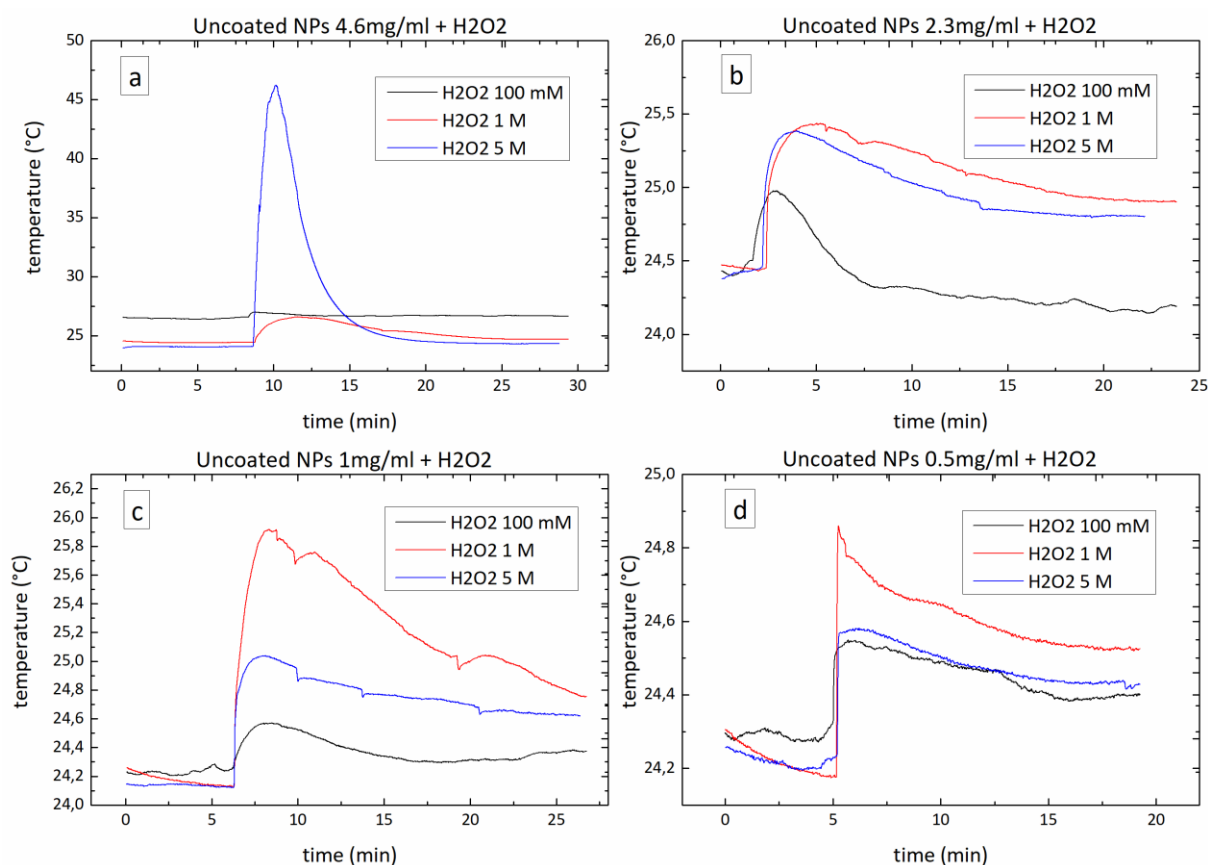


Figure 4.4 Temperature increase in 100 μ l solution with uncoated NPs and H₂O₂. Different concentrations of MANPs were employed: a) 4.6 mg/ml, b) 2.3 mg/ml, c) 1 mg/ml, and d) 0.5 mg/ml. Three solutions of hydrogen peroxide were also used.

A non-expected behavior was observed when H₂O₂ 1M and 5M reacted with MANPs. Indeed, even if the second one showed a higher temperature increase than the first one with 4.6 mg/ml MANPs (**Figure 4.4-a**) and they had similar results with 2.3 mg/ml NPs (**Figure 4.4-b**), when a lower NPs concentration was used, the H₂O₂ 1M led to higher temperatures (**Figure 4.4-c,d**). Probably this was due to the fact that the magnetic stirring with such a small volume was impossible to realize, then non-homogeneous solutions were obtained and maybe not all the NPs could create a contact with hydrogen peroxide.

However, the ROS-scavenging activity of MANPs was proved, both directly with the antioxidant measurements and indirectly with the temperature increase recordings.

5. Oxygen generation

The oxygen generation was a desired goal because of its consequent modulation of the hypoxic microenvironment. By reducing the hypoxia, the responsiveness both to administered drugs, as well as to the radiotherapy, could be improved. Moreover, the hypoxia-related angiogenesis in the tumor site could be reduced.

Dispersions with a final volume of 800 μl were realized by mixing 400 μl of NPs' dispersed in aCSF and 400 μl of H_2O_2 solubilized in aCSF. The graphs with the oxygen production are reported in **Figure 5.1**. Artificial CSF was employed in order to mimic the biological environment inside the brain. Four different concentrations of uncoated MANPs were tested: 50 $\mu\text{g/ml}$, 125 $\mu\text{g/ml}$, 250 $\mu\text{g/ml}$, and 500 $\mu\text{g/ml}$. For each NPs' concentration, six measurements were carried out, one for every hydrogen peroxide condition analyzed.

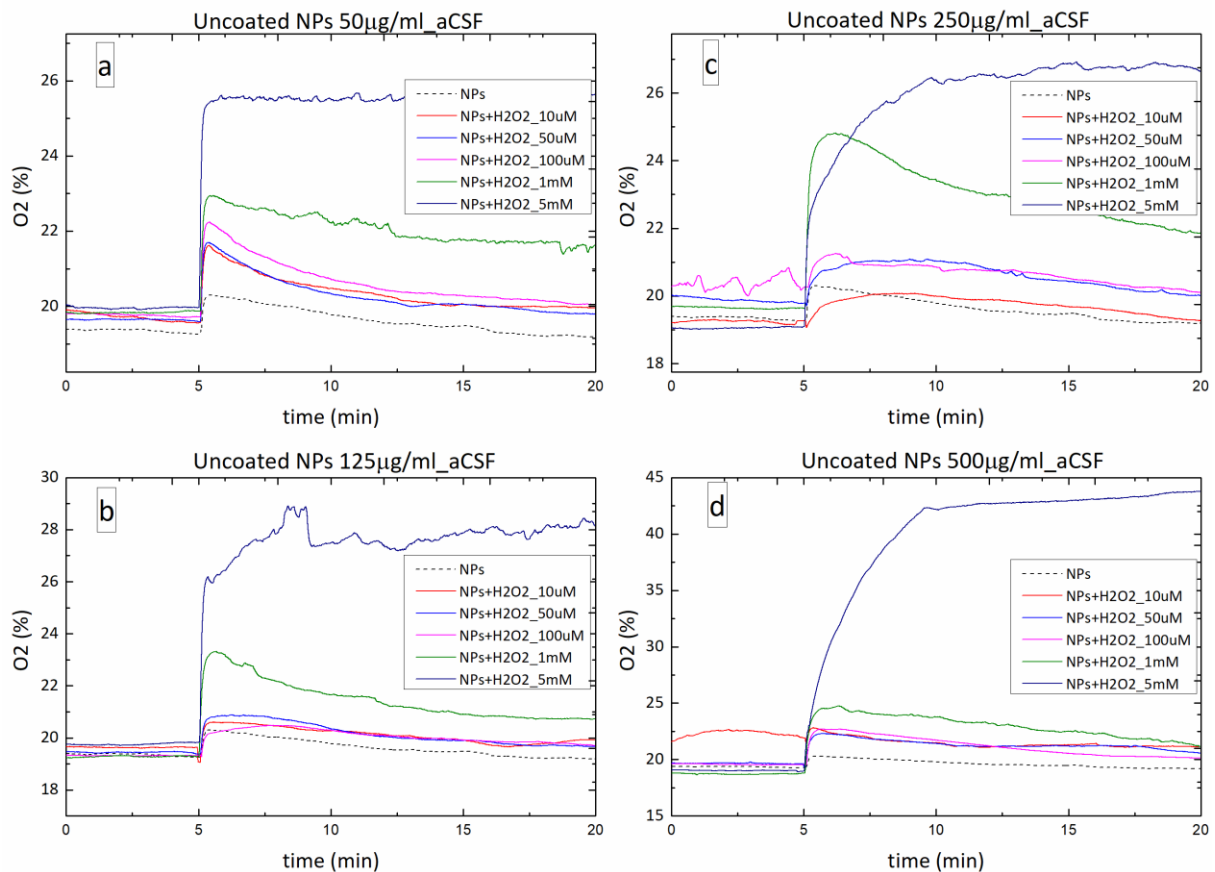


Figure 5.1 Oxygen generation measurements when various hydrogen peroxide concentrations were added to NPs solutions with different concentrations: a) 50 $\mu\text{g/ml}$, b) 125 $\mu\text{g/ml}$, c) 250 $\mu\text{g/ml}$, and d) 500 $\mu\text{g/ml}$. The tests were performed with aCSF.

The concentration of H_2O_2 inside the healthy human body is around 10 μM (but it depends on age and gender), while its concentration in the cancer sites is between 50 μM and 100 μM and it varies with the cell type [113]. Thus, H_2O_2 10 μM , 50 μM , and 100 μM were used in order to study the ability of

the MANPs to generate oxygen. Two higher conditions (1 mM and 5 mM) were also added in order to better understand the NPs' ability to increase oxygen. Furthermore, an experiment without hydrogen peroxide was also performed as control.

First of all, the control solutions were realized by adding 400 μ l of a solution identical to the one that was already in the vial after 5 min of recording, in order to keep the same experimental conditions used in the other measurements. But in this way new oxygen was added to the final solution and this explains why the results showed an increase in the oxygen percentage. Concerning the samples where hydrogen peroxide was present, in all of them a rise of oxygen percentage was observed. Even if the lowest hydrogen peroxide concentrations did not lead to a relevant increase of oxygen, the oxygen production was evident with the high concentrated solutions. Indeed, when H_2O_2 5mM was added to the 500 μ g/ml NPs solution, the oxygen level increased approximately by 22%. However, the oxygen generation ability of the MANPs, due to the manganese shell, was proved.

As the manganese dioxide reacts with the hydrogen peroxide, some DLS measurements were carried out with samples containing both MANPs (0.1 mg/ml) and H_2O_2 (different concentrations), in order to understand if the reaction affected the size and/or the colloidal stability of the NPs (**Figure 5.2**). The experiments were performed at 37°C, 24 h after the mixing of the two components. Deionized water and DMEM supplemented with 10% of FBS were used as solvents, but any significant difference was observed between the two conditions. The hydrodynamic diameter did not change, suggesting that the reaction did not affect the samples during the first day.

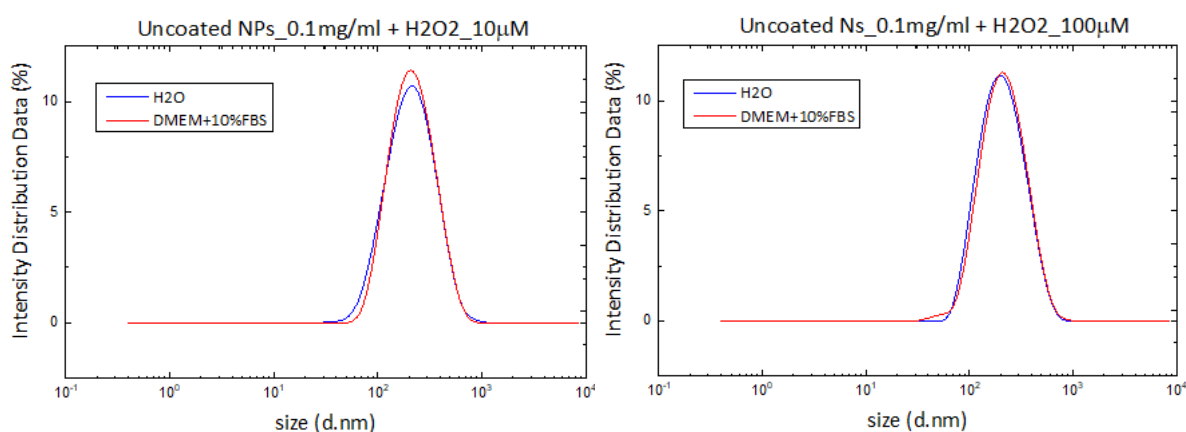


Figure 5.2 DLS measurements of the uncoated NPs with different concentration of H_2O_2 . The analyses were run at 37°C.

In order to better check if the reaction between manganese dioxide and hydrogen peroxide affected the NPs, a longer DLS study was performed. The same concentration of MANPs was used, but they were dispersed in deionized water or in aCSF.

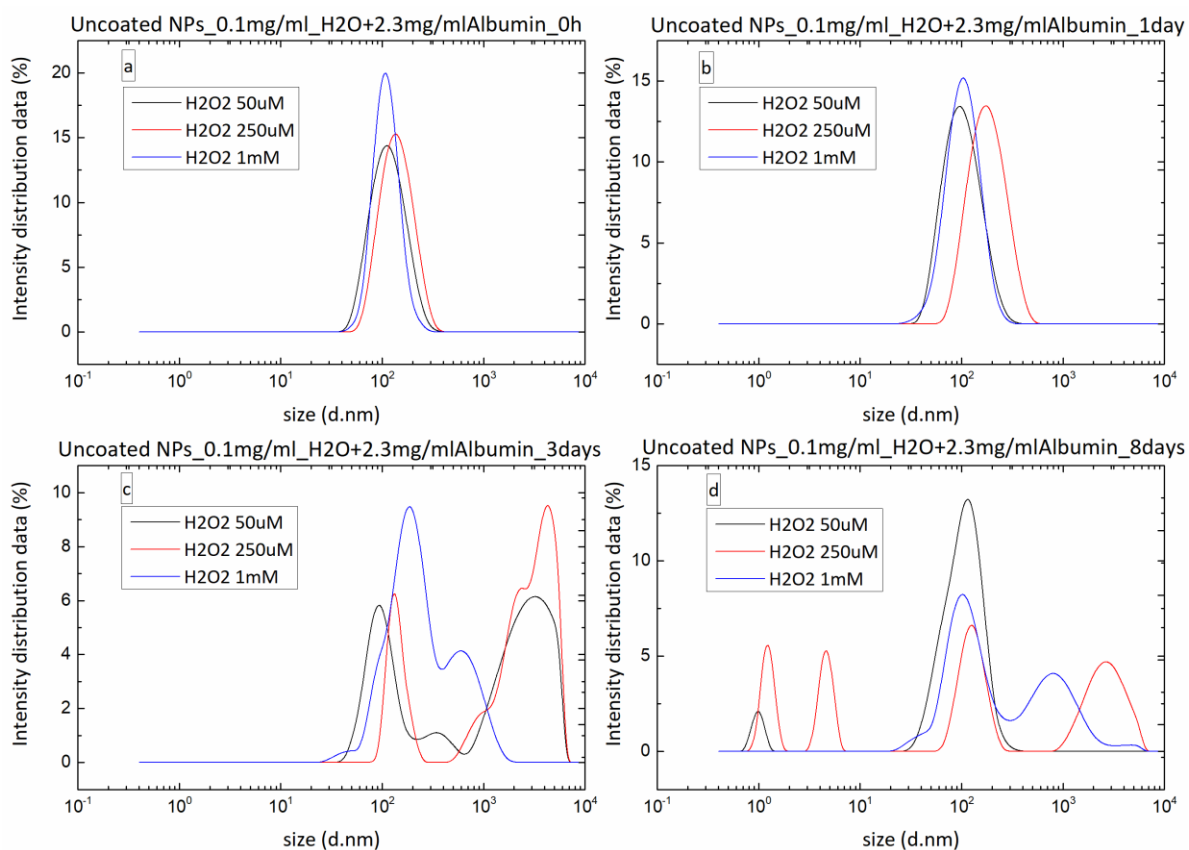


Figure 5.3 DLS measurements at a) 0h, b) 1day, c) 3days, d) 8 days of MANPs in water, albumin and different concentrations of H_2O_2 (50 μ M, 250 μ M and 1 mM).

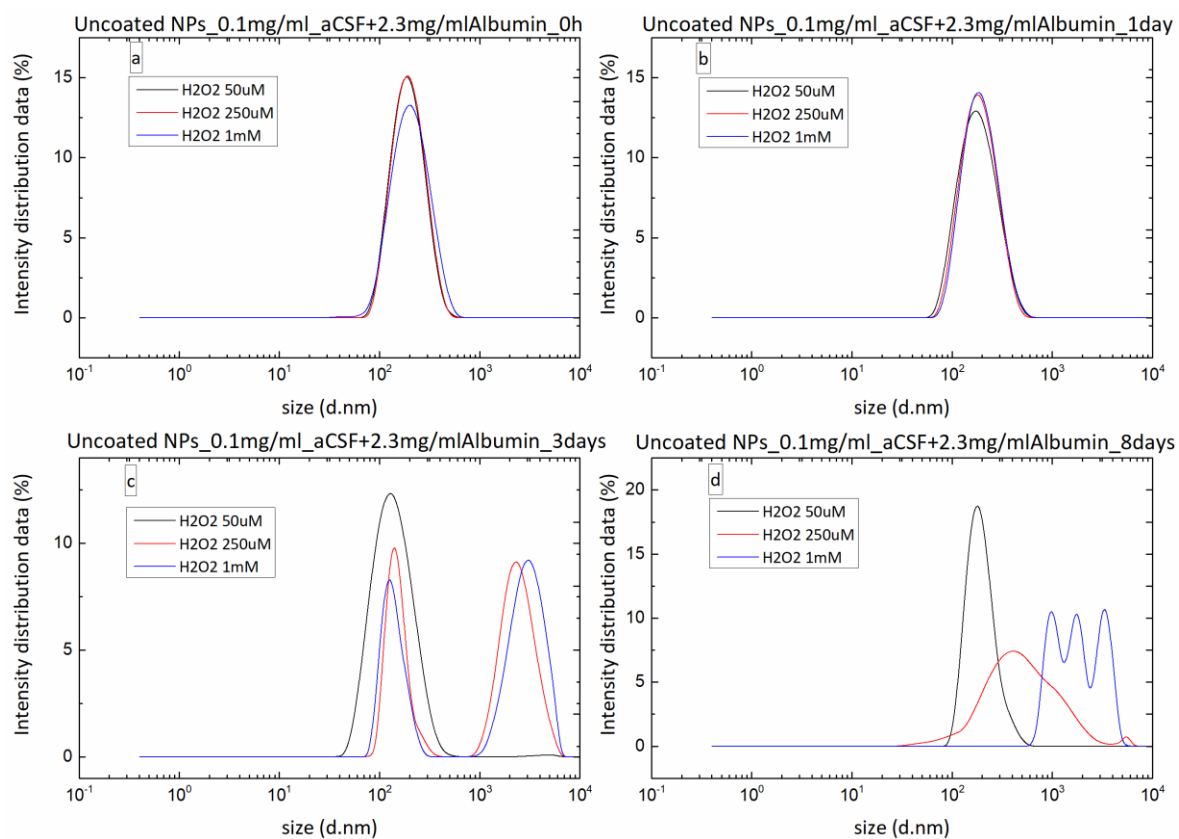


Figure 5.4 DLS measurements at a) 0h, b) 1day, c) 3days, d) 8 days of MANPs in aCSF, albumin and different concentrations of H_2O_2 (50 μ M, 250 μ M and 1 mM).

The results reported in **Figure 5.3** and in **Figure 5.4** showed that the reaction between the ROS and its scavenger (MnO_2) did not affect the NPs during the first day, but starting from the third day multiple populations were present and the hydrodynamic diameter became almost unmeasurable, even if some albumin was added to the solutions to mimic the condition in the blood and to stabilize the MANPs (as described in Section 6.4). Nevertheless, after the reaction of the MANPs with H_2O_2 an increase in the size distribution and the polydispersity was observed. A slightly different behavior could be observed between the samples in water, where high polydispersity and polymodal distributions was observed both at 3 days and 8 days, and the ones in aCSF. The last ones showed two populations at 3 days for the hydrogen peroxide concentrations equal to $250\ \mu\text{M}$ and $1\ \text{mM}$, and they were clearly affected by the reaction at the 8 days' time point. Actually, the NPs with H_2O_2 $50\ \mu\text{M}$ were stable and unaffected until the end of the experiment, probably because of the small amount of hydrogen peroxide.

At low concentrations of H_2O_2 ($50\ \mu\text{M}$) no significant difference was observed concerning the size distribution and the polydispersity of the MANPs, as happened with the higher concentrations of hydrogen peroxide, suggesting that the MANPs are able to keep their colloidal stability once they are found in the cancerous tissue, but their prolonged accumulation inside the tumor will lead to their degradation and possibly to their subsequent clearance from the body. A positive outcome of the sustained degradation of the MANPs (8 days) can be the controlled and sustained release, along with other stimulus like pH and/or temperature, of the encapsulated therapeutic cargo, enhancing this way their therapeutic ability.

6. Coating and characterization

Coating the fabricated MANPs can have numerous advantages, including, improved the biocompatibility as well as increased circulation times in the blood after intravenous administration. Moreover, adding a layer on the surface of the NPs results in the closing of the nanopores, in the cavities of which the drug is hosted, allowing for an enhanced loading efficiency and a sustained release profile. One more advantage of the coating is the inhibition of flocculation of the iron NPs that have the tendency to aggregate because of the Van der Waals' interactions and magnetic forces among them [114]. Finally, the coating may allow for a better crossing of the BBB and an improved targeting towards the cancer cells. Indeed, while the magnetic guidance lets the NPs to accumulate in the tumor site, the chemical targeting allows them to specifically select and reach the cancer cells.

The delivery of the NPs in specific tumor sites can be achieved either by active or passive targeting. While active targeting exploits specific targeting groups on the surface of the NPs, the passive targeting exploits the dimension of the NPs to cross the typical fenestrated endothelium of the vascular systems in advanced cancers. In fact, while at the beginning a tumor is hypoxic and does not need a lot of nutrients, the angiogenesis is stimulated when it develops. The vascular system created in this kind of situations is very porous, allowing the NPs to easily cross the endothelium and be collected by the tumor site. This phenomenon is known as the enhanced permeation and retention (EPR) effect (see Section 1.3). Moreover, in tumor tissues the lymphatic vessels are less developed, so the NPs that reach the diseased site accumulate there, allowing the drug to be released into the extracellular environment and subsequently be uptaken by the cells.

On the other hand, active targeting lets the NPs to recognize the cancer cells thanks to selective ligands on their surface, which are able to link the overexpressed receptors on the cells' surface. In this way, the NPs are uptaken through endocytosis: an endosome is created, and the NPs can be transported into the lysosomes or they can destabilize the endosome and be freed into the cytoplasm.

For the fabricated MANPs two coating strategies were tested: the first one made use of the cell membrane of homologous glioblastoma cancer cells, while the second one with a combination of lipids. The lipid coating of the NPs is a common strategy in the literature, but of course it requests a further step to realize the targeting and even if lipid coated NPs have already entered the clinical trials, they showed a low cellular uptake. On the other hand, the use of the cell membrane represents a more biomimetic approach, since it reduces the immunogenicity related to the lipid coating and does not need an additional targeting process because on its membrane it already contains the components that are able to recognize homologous tumor cells.

6.1. Cell membrane coating

The cell membrane, also called plasmatic membrane, is a phospholipidic bilayer of around 5 nm of thickness. It is a complex and dynamic system composed of lipids and proteins. It delimits the cell from its environment, it keeps the right substances' concentration inside the cell, protects against damaging molecules, and allows the communication with the external environment.

Cell membrane-based systems like red blood cells (RBC) membrane-coated iron oxide NPs that can be used as micromotors have already been reported in literature [115]. Although these systems demonstrated promising potential use as micromotors, they were not designed as a drug delivery and antioxidant system as the one in the presented study, and secondly due to the lack of the targeting molecules against cancer cells on the RBC membranes, these particles would be presenting a lower efficacy concerning the targeting, compared to MANPs here described. [116]. Other systems in literature that made use of cancer cell membrane coated polymeric NPs were used for drug delivery and vaccine applications [117], but, compared to the system of this thesis project, the latter mentioned were not magnetic, lacking this way all the derived properties to control both the path of the NPs and the release of the drug, as well as to induce hyperthermia. Here, by using the cancer cell membrane to coat the MANPs, all these characteristics were put together.

The fact that the MANPs are negatively charged could seem an obstacle to the realization of a coating with the negatively charged CM, but it has been proved that when components with opposite charge and strong affinity are employed, the system fails, resulting in aggregation [118]. On the contrary, a moderate affinity is required in order to set an interaction between the two components but at the same time it allows a certain mobility and local rearrangements.

6.1.1. Coating procedure

U-251 MG cell line was used to prepare the cell membrane and coat the NPs. A more detailed description of the cell line will be given in Part II, where the *in vitro* studies will be illustrated. The cell membrane was realized by using the phospholipid bilayer of the same cells by which the NPs should be uptaken. Indeed, the hypothesis was that in this way the cancer cells would recognize the NPs thanks to their coating, due to receptors and proteins that are found into their membrane, resulting in an enhanced internalization by homologous cancer cells.

U-251 MG cells were cultured until 90% confluence in Petri dishes with high-glucose DMEM supplemented with 10% FBS, 1% penicillin/streptomycin, and 1% L-glutamine, and at normal culture conditions (37°C, 5% CO₂). The cells were between passage 17 and 32 and the average of obtained cells per dish was 3.3×10^6 .

The cells were detached by using trypsin 0.25% and leaving the cells 5 min at 37°C. The cells were then spun down 6 min in DMEM with FBS at 2600 rpm at 24°C and they were re-suspended in PBS and counted. After a second spinning with the same parameter as the previous one, the cancer cells were suspended again in a small amount of PBS. Cells' lysis was performed with an EmulsiFlex-B15 by Avestin high-pressure homogenizer (HPH). A pressure of 20 psi (7 kPa) was used and the HPH passing was repeated 10 times. The final solution was spun down to remove impurities and intracellular components with a Beckman Avanti™30 centrifuge with F2402 24-place rotor for 5 min at 20000 xg (15000 rpm) and at 4°C. The supernatant was collected and spun down again for 1 h at 60000 xg (25000 rpm) and at 4°C. The pellet was then collected, re-suspended in deionized water, and sonicated 10 seconds. The solution was kept at 4°C.

Once the CM was ready, the desired quantity of NPs was solubilized in deionized water in order to obtain a 1 mg/ml solution, that was later sonicated with a Fisherbrand™ Model 120 Sonic Dismembrator for 30 min at 60% amplitude at 4°C. Another solution with the CM derived from 5×10^6 cells was then added to the first one (the reason of this value is discussed in Section 6.1.2). The solution was sonicated for 30 min at 60% amplitude at 4°C to fuse together the CM and the NPs, as described in the literature [118]. The cleaning was realized with deionized water and repeated 3 times, 1 h of spinning with a Sigma 1-14K centrifuge was performed at 16000 xg (15000 rpm).

6.1.2. Characterization

Confocal analysis

In order to understand the number of cells needed to coat 1 mg of NPs, 3 different conditions were tested. Following the previously described procedure, the CM-coating was realized by employing 3×10^6 cells, 5×10^6 cells, and 7×10^6 cells. All of the three CM coatings were stained with 5 μ l of Vybrant™ Cell-Labeling Solution green DiO ($C_{53}H_{85}ClN_2O_6$) ($\lambda_{ex}/\lambda_{em} = 484/501$ nm) by ThermoFisher Scientific, which is a dye that creates bindings with lipids and cell membrane. After adding the dye to the coated NPs, the solution was incubated for 20 min at 37°C. Then, two cleanings with deionized water were attempted by spinning the solution 5 min at 16000 xg (15000 rpm) at room temperature.

Finally, the samples were observed using confocal laser scanning microscopy on a Nikon C2+ system. The sample with the 3×10^6 cells' CM coating did not show any fluorescence, so no images were taken for it. On the contrary, the samples with 5 and 7×10^6 cells' CM coating were very similar and a picture of the 5×10^6 sample is reported in **Figure 6.1**. Since the results for 5 and 7×10^6 were the same, it was decided to employ the procedure by using 5×10^6 cells for every mg of NPs, an amount of cells that has already been used in literature [119].

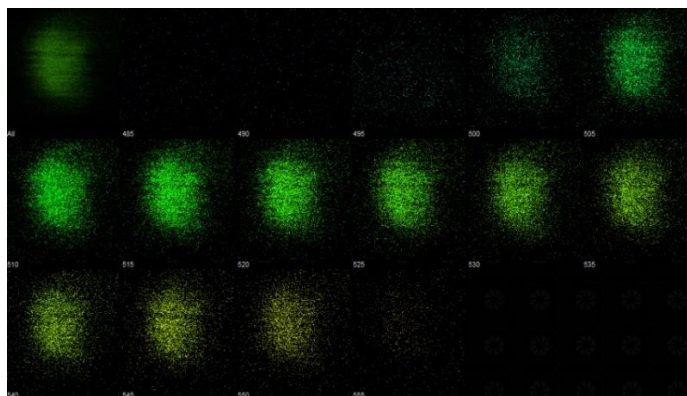


Figure 6.1 Confocal image of the stained CM-coated NPs for which 5×10^6 cells' membrane were employed.

SEM images

The coating of the MANPs using the cell membrane did not seem to affect their size and/or their morphology significantly as it can be seen in **Figure 6.2**. A larger size that can be observed in some particles, it can be attributed to the fact that more than one MANPs were coated together or that some MANPs presented bigger size than the average.

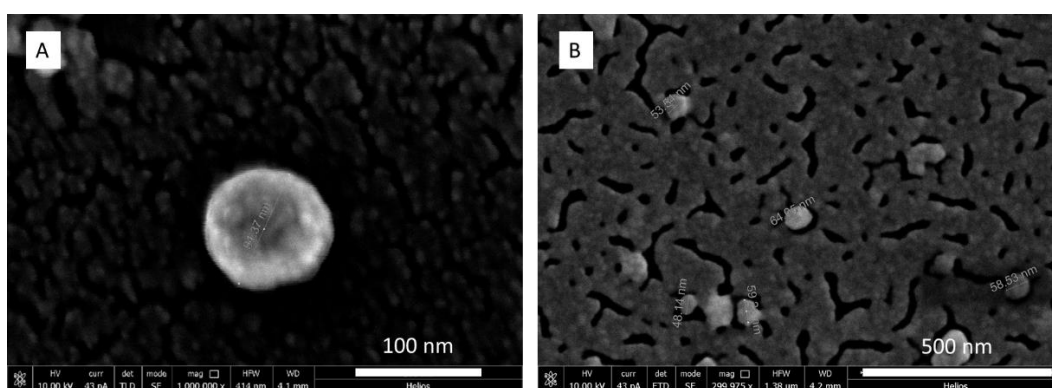


Figure 6.2 SEM images of the CM-coated MANPs.

TEM images

TEM analysis showed that the CM-coating did not change the cubic shape of the MANPs (**Figure 6.3**).

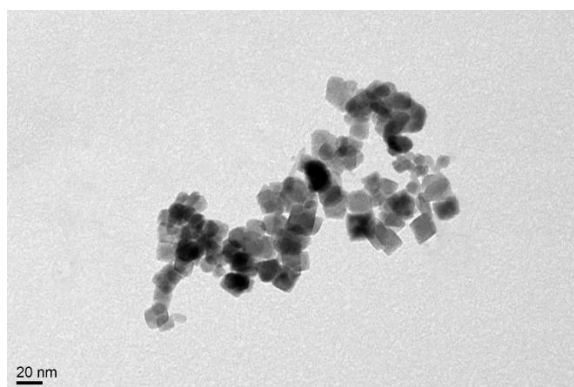


Figure 6.3 TEM image of the CM-coated MANPs

FT-IR analysis

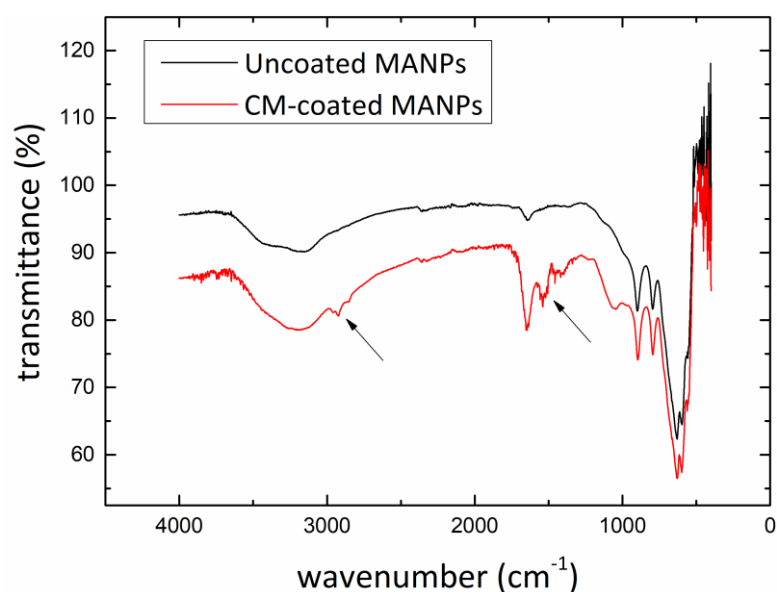


Figure 6.4 Compared FT-IR analysis of uncoated and CM-coated MANPs. The peaks associated with the CM are highlighted by the arrows.

The FT-IR analysis was performed for the CM-coated NPs and it was compared with the one previously realized for the uncoated NPs (**Figure 6.4**). A first proof of the obtained coating was the presence of the peaks at around 1500 cm⁻¹, that are typical for phospholipids and in particular of phosphatidylcholine [120]. Moreover, the peaks at around 1290 cm⁻¹ and 2900 cm⁻¹ were associated with the aliphatic chain of the lipids of the cell membrane [121].

EDS analysis

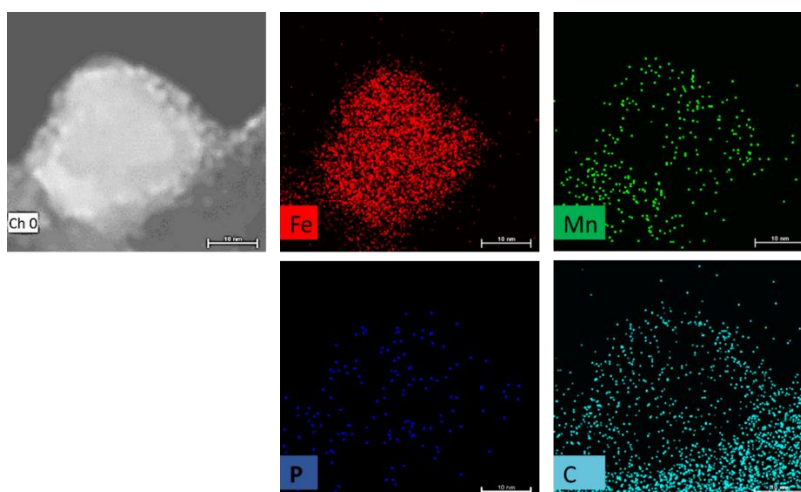


Figure 6.5 EDS analysis showing the co-localization of phosphorus and carbon with manganese and iron.

EDS analysis was also performed on the CM-coated MANPs. The presence of phosphorous and carbon is a proof of the obtained coating, as these are the main constituents of the phospholipid bilayer. The

co-localization of phosphorous and carbon with the atoms of iron and most of all manganese (**Figure 6.5**) showed that the coating was successful. Furthermore, the EDS spectrum reported in **Figure 6.6** allowed for an initial estimation of the phosphorous amount, which was found to be approximately 1/10 of the manganese and 1/100 of the iron.

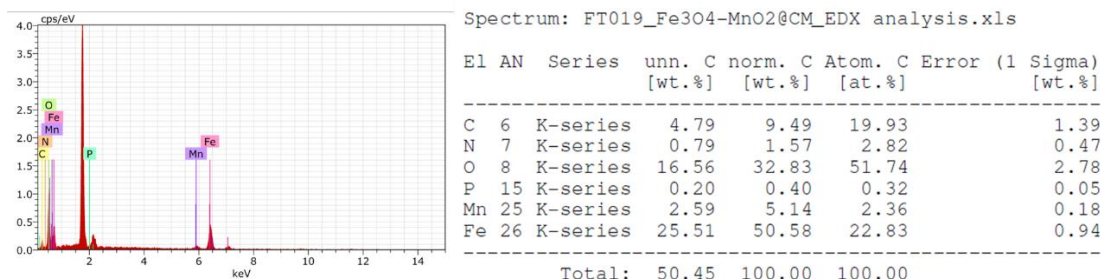


Figure 6.6 EDS map of the CM-coated NPs.

ICP analysis

In order to have a more precise analysis of the percentage of each element in the CM-coated MANPs, ICP was performed and the results are reported in **Table 6.1**: iron was found to be 62.50% of the sample, while the percentage of manganese was equal to 5.86%. Actually, this analysis showed that the percentage of phosphorous is lower than the one extracted from the EDS maps, and it is equal to 0.22%.

Table 6.1 ICP results for the CM-coated MANPs

Element	Percentage	ppm
P	0.22	0.46
Fe	62.50	130.1
Mn	5.86	12.19

DLS analysis

The DLS measurements that were performed for the uncoated MANPs were also performed for the CM-coated ones, aiming at understanding the effect of the coating in the colloidal stability of the nanoparticles. Three different solvents (deionized water, DMEM and DMEM+10%FBS) and four different time points (0h, 1h, 6h, and 24h) were chosen to perform the stability studies, always at 37 °C (**Figure 6.7**). A similar behavior with the uncoated MANPs (**Figure 3.10**) was also observed here. When the NPs were in DMEM, the hydrodynamic diameter increased, probably due to aggregation, while when FBS was added in the DMEM an increased stability was observed.

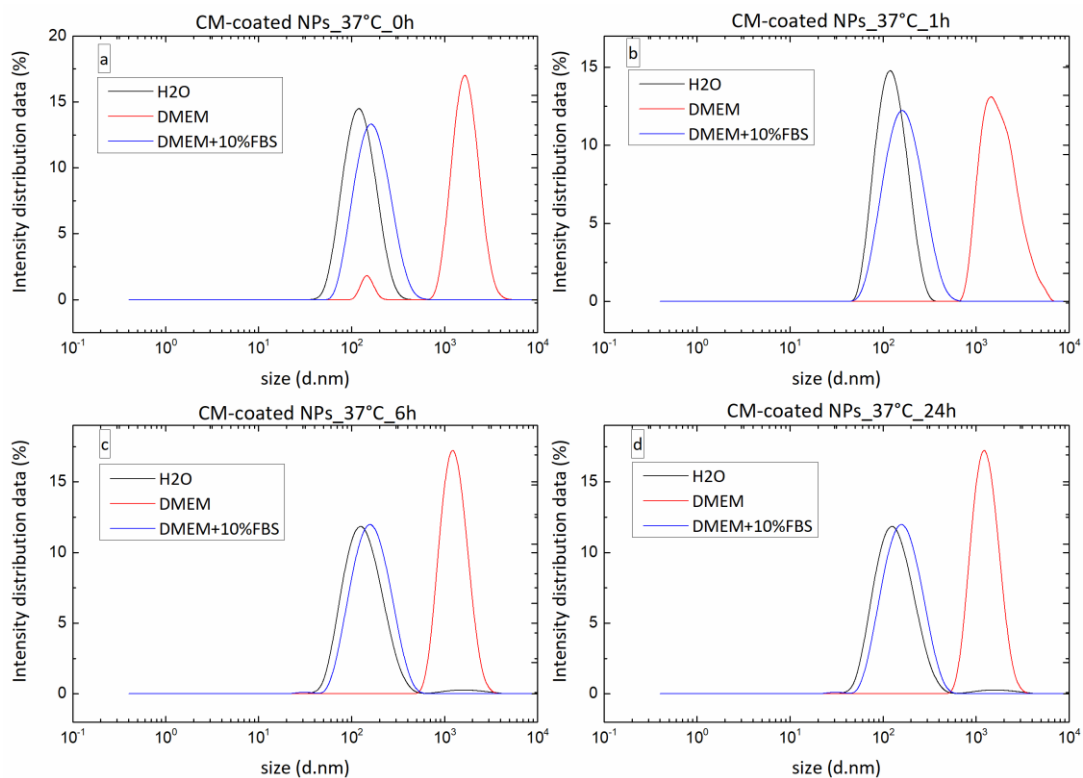


Figure 6.7 DLS measurement of the CM-coated MANPs. Samples with a concentration of 0.1 mg/ml were employed and they were tested at 37°C, at different time points (0h, 1h, 6h, 24h), using water, DMEM and DMEM+10%FBS.

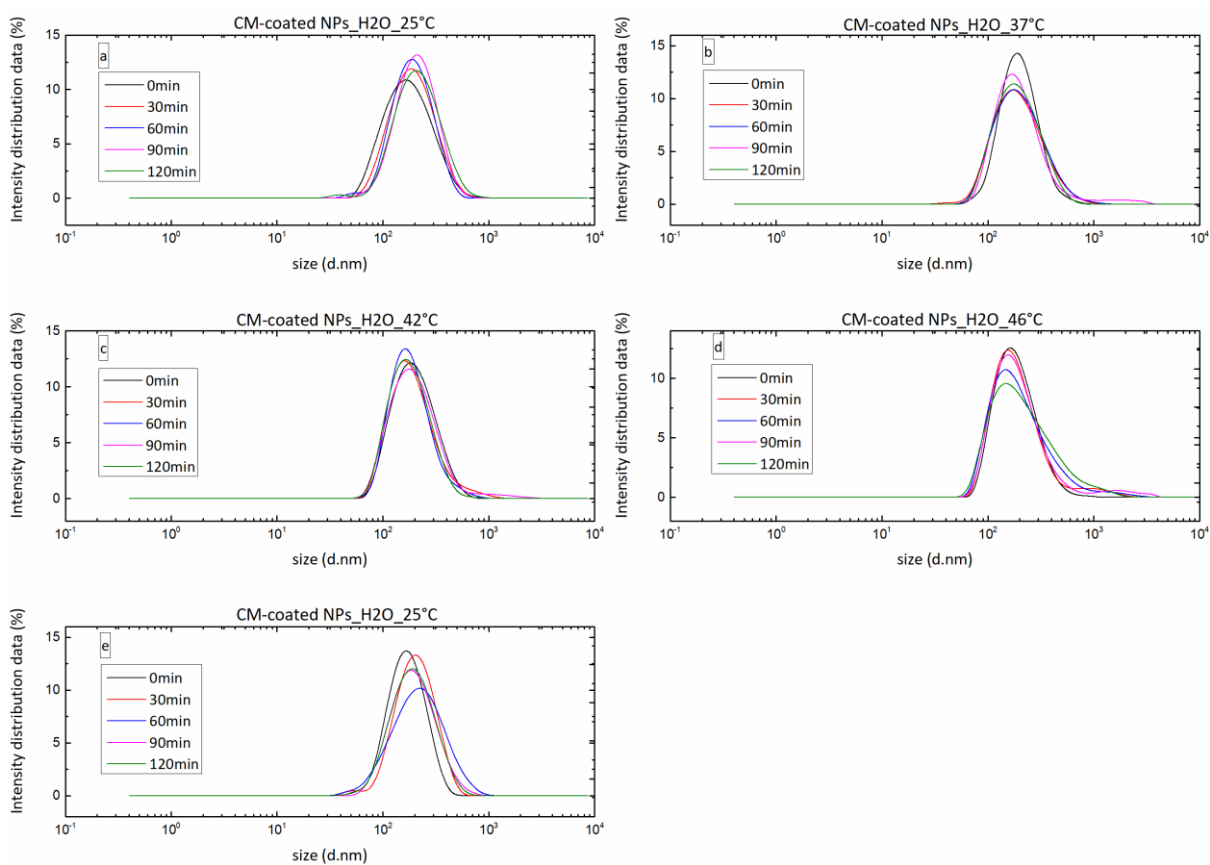


Figure 6.8 DLS stability study of CM-coated MANPs at different temperatures (25 °C, 37 °C, 42 °C and 46 °C) and at different time points (0 min, 30 min, 60 min, 90 min, 120 min).

The stability study in deionized water was performed as well, in order to have data to compare with the uncoated system's results. As for the uncoated MANPs, the samples were measured at 25°C, 37°C, 42°C, 46°C, and then again at 25°C. For each temperature condition, the analysis was run at 0 min, 30 min, 60 min, 90 min, and 120 min. The coating did not change the stability of the NPs, as showed in **Figure 6.8**.

Table 6.2 Hydrodynamic diameters and PDIs of both uncoated (on the top) and CM-coated (on the bottom) MANPs during the stability studies in water.

Average values for the uncoated NPs	T	d.nm	PDI
	25°C	159.1 ± 6.2	0.2408 ± 0.0197
	37°C	168.7 ± 2.4	0.2514 ± 0.0099
	42°C	174.7 ± 3.4	0.2480 ± 0.0130
	46°C	185.2 ± 3.3	0.2576 ± 0.0132
	25°C	195.5 ± 6.5	0.2624 ± 0.0127

Average values for the CM-coated NPs	T	d.nm	PDI
	25°C	176.1 ± 10.3	0.1996 ± 0.0072
	37°C	181.4 ± 5.4	0.2134 ± 0.0070
	42°C	179.9 ± 4.0	0.2176 ± 0.0074
	46°C	178.2 ± 2.3	0.2306 ± 0.0065
	25°C	178.8 ± 9.8	0.2212 ± 0.0285

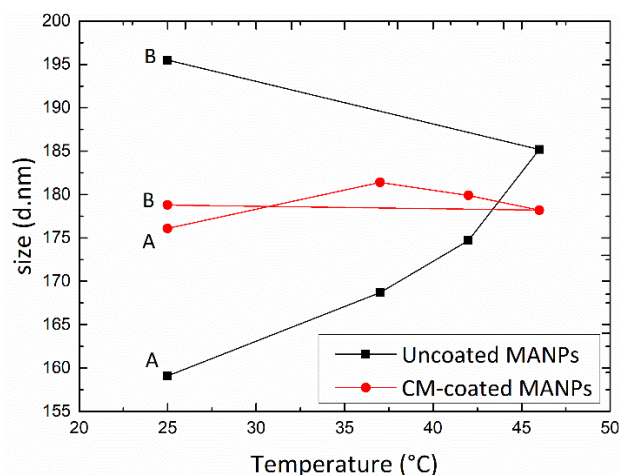


Figure 6.9 Comparison of the average values of the hydrodynamic diameter and of the PDI during the stability studies (temperature cycle from A to B) of uncoated and CM-coated MANPs in water.

As it is possible to see from **Figure 6.9**, the hydrodynamic diameter of the NPs was bigger for the CM-coated MANPs until temperature reached 42°C. As the CM layer is extremely thin, this increase was probably due to a swelling of the coating or due to surface interactions of the hydrophilic components of the phospholipid membrane. It has to be noted, that these hydrophilic components may also be responsible for the increased stability of the CM-coated MANPs, compared to the uncoated ones. The PDI is similar between the uncoated and coated situation (**Table 6.2**), that means that there are not small pieces of CM detached from the NPs, otherwise the PDI would have been increased for the coated NPs.

TGA analysis

TGA was performed using a TGA Q50 from TA instruments. The temperature was set at 600 °C with a heating rate of 10 °C/min and under a nitrogen flow of 50 ml/min.

The thermogravimetric results that are reported in **Figure 6.10** show both the thermogravimetric curves (solid lines) and the differential thermogravimetric curves (dashed lines). With the temperature increase, the weight of the MANPs remained almost unaltered for the uncoated sample, while it decreased more than 10% for the CM-coated sample. This weight loss can be attributed to the melting of the phospholipid bilayer above 200 °C. Below the so-called melting temperature (T_m), the membrane

is more rigid, while for higher temperature it becomes more fluid. The T_m of the cell membrane depends on the phospholipid chain length and saturation, but also on the presence of other substances. This was also the phenomenon exploited for the release of the drug, as presented in Section 9. By looking at the DTG graphs, it is possible to observe that the rate of loss of weight had a maximum at 300°C, meaning that at this temperature the cell membrane melted faster. Moreover, the CM-coating was not destabilized for temperatures lower than 100°C and this was important for the hyperthermia tests that will be discussed in Section 7.

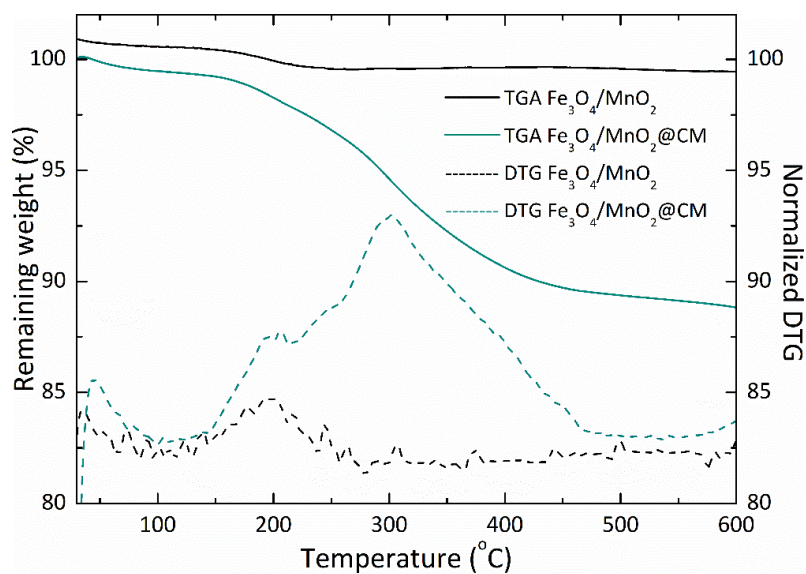


Figure 6.10 TGA results for uncoated and CM-coated NPs. When temperature increases, the weight of the CM-coated MANPs decreases, suggesting the presence of the coating.

Antioxidant measurements

The antioxidant measurements were performed with the same kit used for the uncoated sample analysis (Section 4). The obtained results that are presented in **Figure 6.11** were similar to the previous ones, although a bit lower for the 0.1 mg/ml concentration of CM-coated NPs.

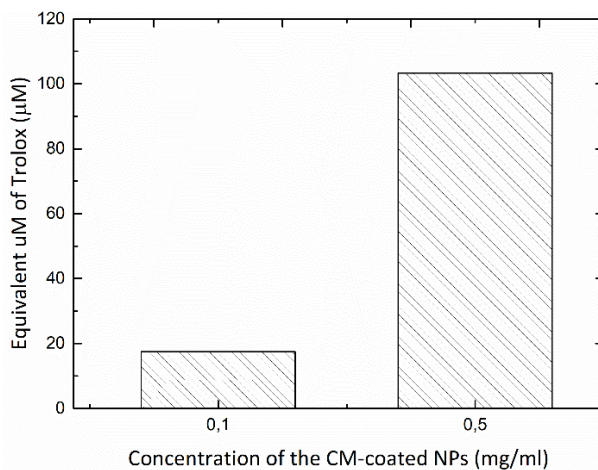


Figure 6.11 Antioxidant measurements for the CM-coated NPs

This difference was probably due to the fact that the coating did not allow the manganese dioxide to act at the maximum of its ROS-scavenger properties, at least for the time period of 15 min that the reaction was carried out.

Magnetic measurements: VSM

VSM results reported in **Figure 6.12** showed a decreased saturation magnetization for the CM-coated MANPs and an increased coercivity. While the high coercivity was not a problem, and on the contrary, it could lead to higher SAR values as it was previously mentioned (Section 3.9), the lower saturation magnetization was a negative aspect, because it is directly related with the heating efficiency. Although, the hyperthermia experiments (Section 7) showed that did not happen, probably because the high coercivity counteracted the low saturation magnetization.

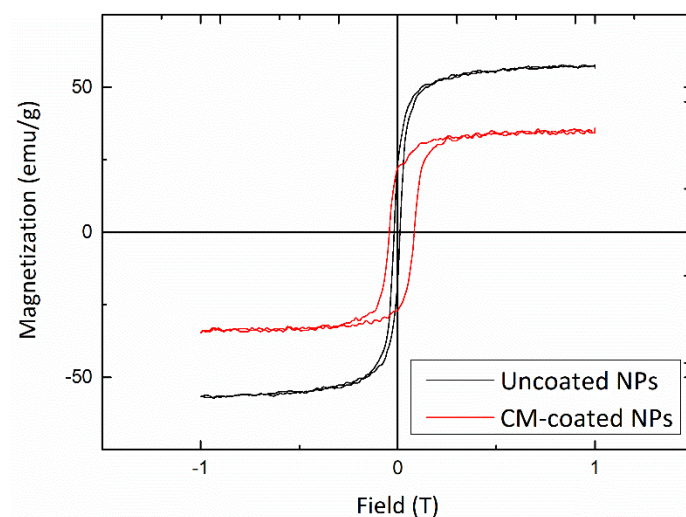


Figure 6.12 Compared B-H graphs of the uncoated and CM-coated NPs.

6.2. Coating with cetyl palmitate

This phase was preparatory for the lipid coating and it was useful to understand the right proportions between the uncoated NPs and the necessary lipids to coat them. The lipid coating was useful to have some properly coated NPs to use as a comparison in the internalization experiments.

MATERIALS

The coating of 5 mg of Mn/Fe=1/10 ratio NPs with different quantities (1 mg, 2.5 mg, 5 mg, 10 mg, and 50 mg) of cetyl palmitate ($C_{32}H_{64}O_2$, CP) (**Table 6.3**), was performed in order to find the optimal coating conditions. 3 ml of Tween80 (T80) 1% in deionized water were used as surfactant, while 200 μ l of chloroform ($CHCl_3$, also known as trichloro-methane) were used in order to improve the homogenization among the uncoated MANPs and the used lipid.

Table 6.3 Materials used to realize the cetyl palmitate coating of 5 mg of the uncoated NPs.

SAMPLE	Mn/Fe=1/10	CETYL PALMITATE	TWEEN80	CHLOROFORM
FT005A	5 mg	1 mg	3 ml	200 μ l
FT005B	5 mg	2,5 mg	3 ml	200 μ l
FT005C	5 mg	5 mg	3 ml	200 μ l
FT005D	5 mg	10 mg	3 ml	200 μ l
FT005E	5 mg	50 mg	3 ml	200 μ l

PROCEDURE

The uncoated NPs and the chloroform were mixed, and the dispersion was sonicated 20 min at 4°C. Then the dispersion was placed at 65 °C and the CP was added. After 1-2 min the T80 solution pre-warmed at 65°C was also added. The mixture was sonicated 10 min and then kept at 4°C for 30 min. Three cleanings with deionized water were performed, each of them with 15 min of spinning at 16000 xg (15000 rpm).

RESULTS and COMMENTS

During the cleanings of the coated NPs, the supernatants of the sample with 50 mg of CP every 5 mg of NPs had always a creamy colour, evident sign of the excess of cetyl palmitate. Therefore, this proportion of material was excluded from the possible useful ones. Another qualitative but clear observation was the fact that, in only few minutes, the solutions containing the NPs with lower quantities of CP were characterized by a fast precipitation (**Figure 6.13**).

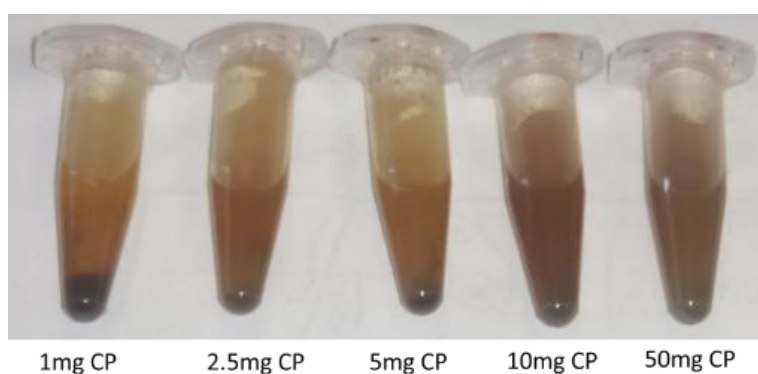


Figure 6.13 Evidence of the fast precipitation of the coated NPs with lower quantities of CP.

SEM images of all the 5 samples were taken, as shown by **Figure 6.14** in order to better understand the effect of the coating. After excluding the samples with 1 mg, 2.5 mg and 50 mg of CP for the aforementioned reasons (fast precipitation and excess of lipid), only the 5 mg and the 10 mg samples could be considered. By looking at the SEM images of these two specimens (**Figure 6.15-C** and **Figure 6.15-D** respectively for 5 and 10 mg of CP coating), it can be noticed that the 10 mg of cetyl palmitate

for 5 mg of NPs represent the best option. As a consequence, 10 mg were the quantity of lipids that was decided to be used for the following coatings.

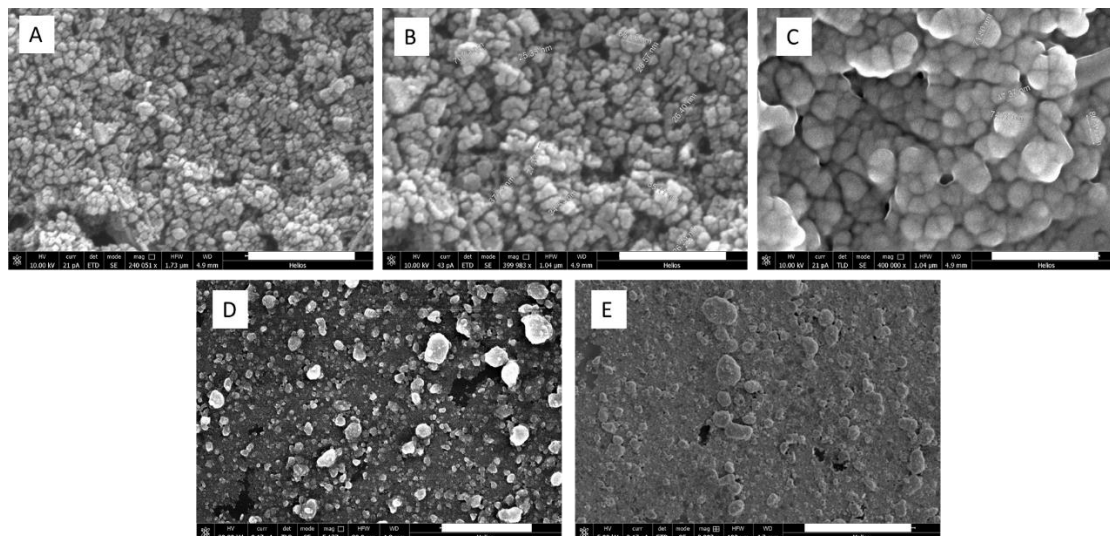


Figure 6.14 SEM images of the NPs coated with CP. Every 5 mg of NPs, different quantities of CP were used: 1mg (A, scale bar 500nm), 2.5mg (B, scale bar 300nm), 5mg (C, scale bar 300nm), 10mg (D, scale bar 20 μ m) and 50mg (E, scale bar 30 μ m).

Some EDS analyses were also performed in order to qualitatively check if the carbon was present, as a proof of the coating with cetyl palmitate. The elemental analysis for this section was performed using an SEM built-in electron dispersion X-ray analysis detector from Bruker. In the results, the silica peak that is always present it is attributed to the Si of the substrate and it is removed from the analysis.

Both the 1 mg and the 10 mg samples showed that the desired atom was there, as it can be noticed in **Figure 6.15** and in **Figure 6.16**.

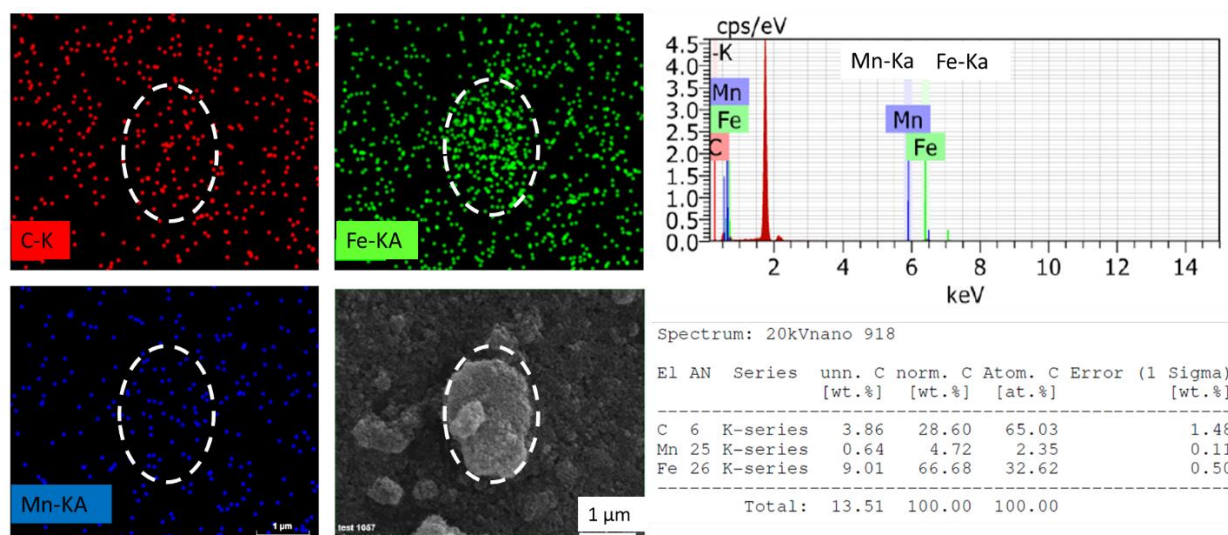


Figure 6.15 EDS analysis of the NPs coated with CP. Every 5 mg of NPs, 1mg of CP was employed for the coating.

Scale bar: 1 μ m

PEG is a hydrophilic and flexible polymer that is usually used to create an external layer around nanoparticles in order to increase their half-life in the bloodstream. It prevents the protein corona formation by making it less energetically favourable and it does not allow the opsonins to be adsorbed by the NPs. PEGylation is not an ideal coating strategy either, as it inhibits cellular uptake and endosomal escape of the nanoparticle within the target cells, a phenomenon known as the “PEG Dilemma” [119]. PEG-derived mPEG-DSPE is hydrophobic, expensive but not thermoresponsive. It was used because it increased the T_m of the solution, so it made the solution thermally stable. mPEG-DSPE structure is reported in **Figure 6.19**.

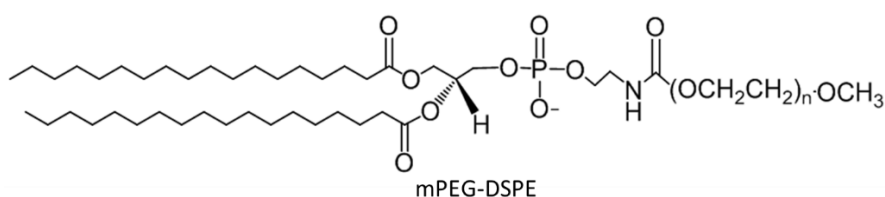


Figure 6.19 Structural formula of mPEG-DSPE

In every sample different proportions of these substances were used, with a final amount of lipids always equal to 10 mg every 5 mg of NPs, as decided in the previous phase. The exact quantities are listed in **Table 6.4**. During the procedure 200 μ l of a solvent were needed: in some cases, it was chloroform (CHCl_3), in two samples it was pure ethanol ($\text{CH}_3\text{CH}_2\text{OH}$).

Table 6.4 Material and quantities used for the lipid coating samples. Every 5 mg of NPs, 10 mg of lipids were employed, but with different proportions. The solvent was a parameter to set, too, so chloroform and ethanol were tested.

SAMPLE	Mn/Fe=1/10 (FT001)	CETYL PALMITATE	GLYCERYL MONOOLEATE	mPEG- DSPE	TWEEN80	SOLVENT
FT007A	5 mg	8 mg	-	2 mg	3 ml	CHCl_3
FT007B	5 mg	6 mg	2 mg	2 mg	3 ml	CHCl_3
FT007C	5 mg	-	6 mg	4 mg	3 ml	CHCl_3
FT007D	5 mg	-	6 mg	4 mg	3 ml	$\text{CH}_3\text{CH}_2\text{OH}$
FT007E	5 mg	-	-	10 mg	-	$\text{CH}_3\text{CH}_2\text{OH}$

PROCEDURE

The uncoated NPs were solubilized into the solvent (solution A) and sonicated around 20 min (it depends on the evaporation of the solution) at 4°C at 40% amplitude. Meanwhile, the T80 was heated up at 65°C. A second solution (solution B) with lipids and warm T80 was prepared. The solution A was then added to the solution B and it was sonicated 10 min at 65°C at 40% amplitude, while moving up and down the sonicator probe for the first minute. The final solution was kept at 4°C for 30 min. 3 cleanings with deionized water were realized by spinning down the samples 15 min at 16000 \times g (15000 rpm). Finally, each sample was re-suspended in 1 ml of deionized water.

The final average yield of the procedure was equal to 28.33%.

CHARACTERIZATION

SEM images

SEM images were taken for the lipid-coated NPs (**Figure 6.20**), but no significant difference among them was observed. All the samples still presented the desired nanostructure.

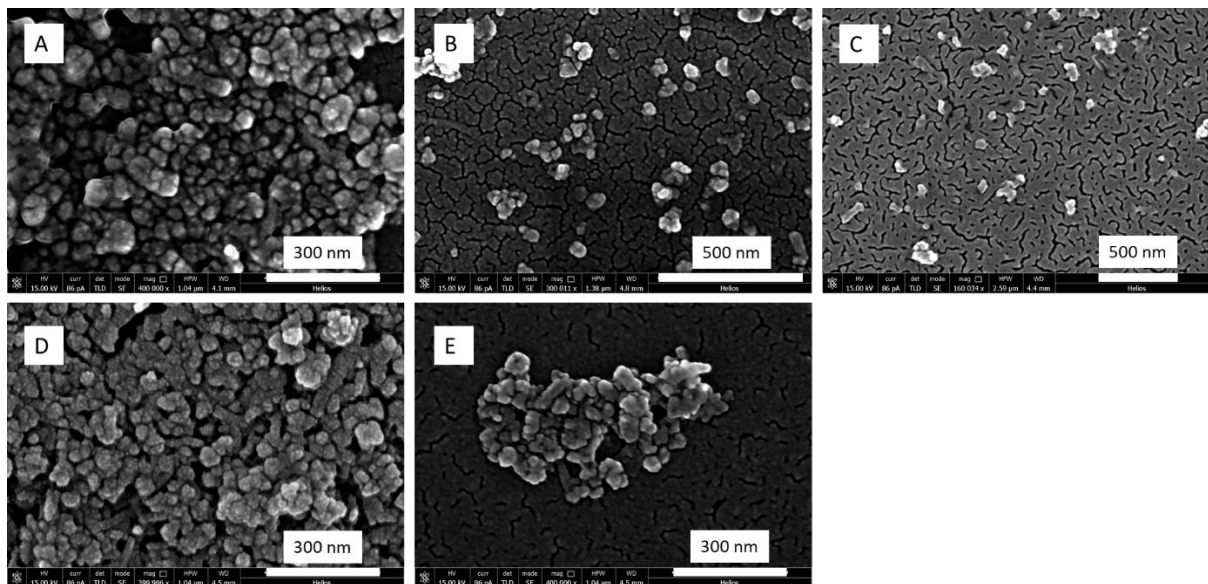


Figure 6.20 SEM images of the lipid coated NPs. A) CP, mPEG-DSPE and CHCl_3 . B) CP, GMO, mPEG-DSPE and CHCl_3 . C) GMO, mPEG-DSPE and CHCl_3 . D) GMO, mPEG-DSPE and $\text{CH}_3\text{CH}_2\text{OH}$. E) mPEG-DSPE and $\text{CH}_3\text{CH}_2\text{OH}$.

DLS measurements

DLS measurements were performed at 25°C in water. Two different concentrations were employed (0.5 mg/ml and 0.1 mg/ml) and the results are reported in **Figure 6.21**.

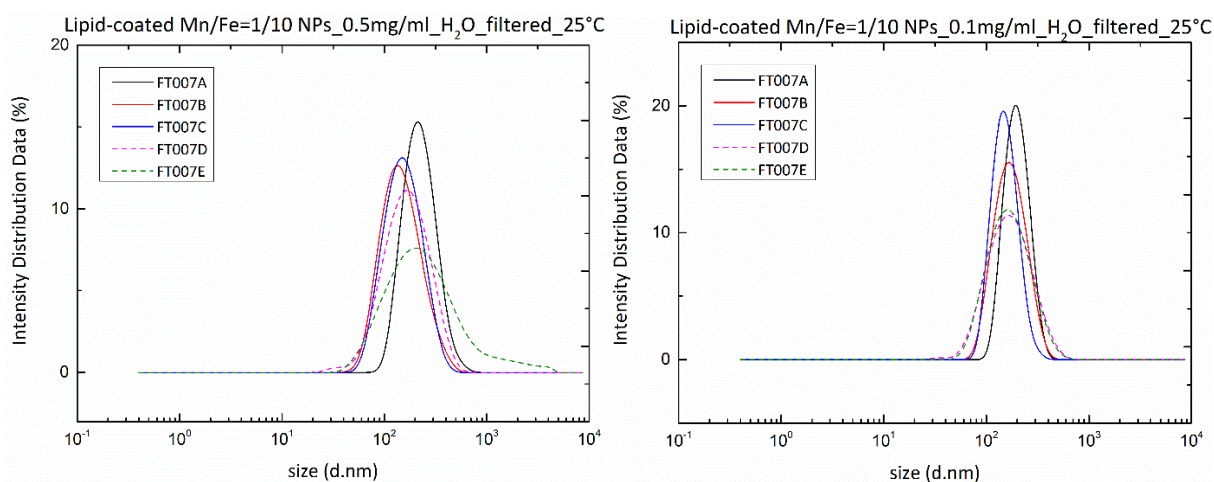


Figure 6.21 DLS measurements of lipid-coated MANPs in water at 25°C. On the left, the concentration of NPs is 0.5 mg/ml, while on the right 0.1 mg/ml were used.

with the lowest concentration better measurements were obtained in general, but the same relative behavior was observed among the lipid-coated NPs samples. The NPs that were realized with a procedure involving ethanol had a bigger PDI, so they were excluded. Among the samples coated with the help of chloroform, the one with CP and mPEG-DSPE showed a slightly bigger hydrodynamic diameter, so it was not used in the following studies. The average Z-potential of all the lipid-coated NPs was equal to -16.55 mV, so its absolute value was lower than the one of the uncoated NPs. That means that the lipid coated NPs were less stable than the CM-coated ones.

DLS stability studies

In order to decide which sample was the best one among the lipid coated MANPs, in order to be used for the internalization experiments, stability studies were performed with the two remaining samples, that means with the CP, GMO and mPEG-DSPE coated NPs and the GMO and mPEG-DSPE coated sample. Measurements were carried out in water at different temperatures (25°C, 37°C, 42°C, 46°C, and 25°C again) and for each temperature condition at various time points (0 min, 30 min, 60 min, 90 min, and 120 min). The results of the sample with CP, GMO and mPEG-DSPE (FT007B) are reported in **Figure 6.22**, while the graphs of the sample with GMO and mPEG-DSPE (FT007C) are presented in **Figure 6.23**.

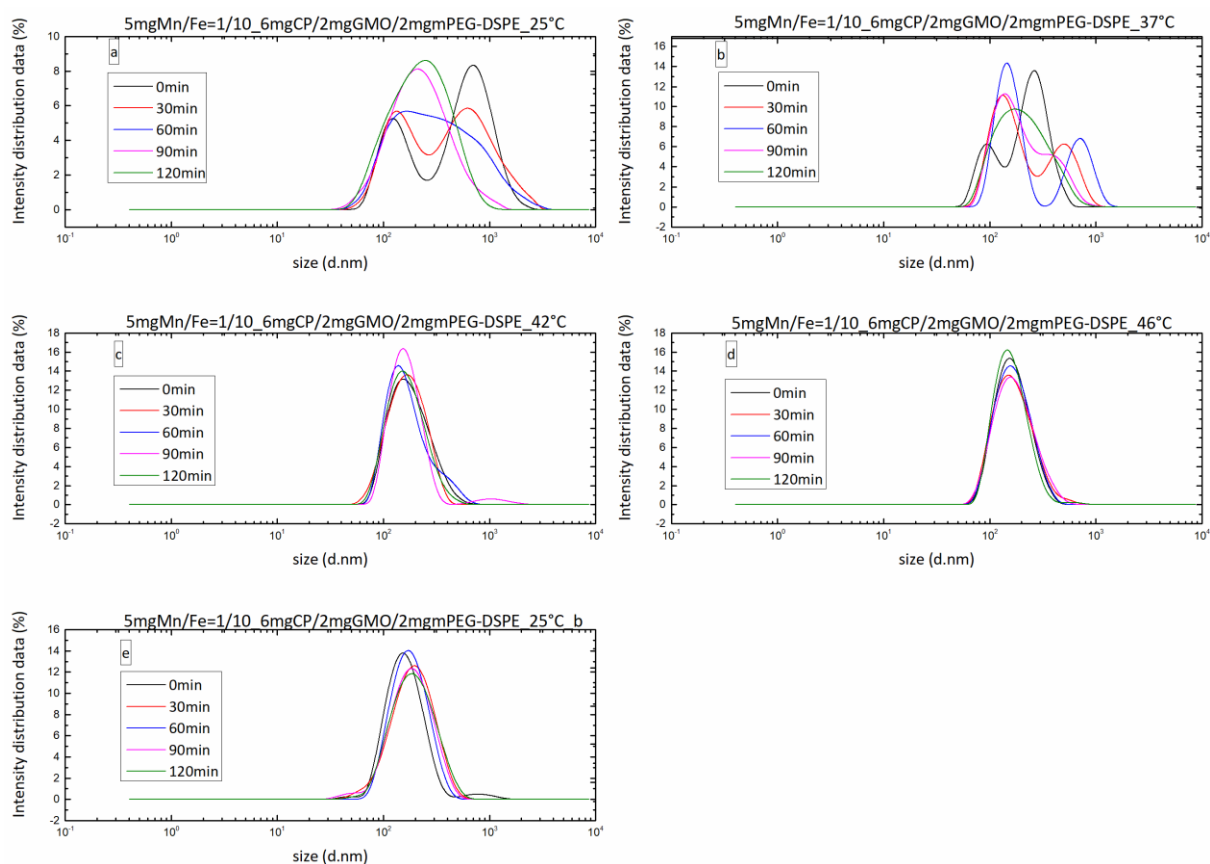


Figure 6.22 DLS stability study of the sample with a coating made of 6 mg CP, 2 mg GMO, and 2 mg mPEG-DSPE (FT007B).

Both the samples showed instabilities during the first measurements, probably due to bigger aggregates that then fell down and were not detected in the following measurements. No significant differences were highlighted between the two specimens. As a consequence, the sample containing all the three lipids was chosen for the internalization experiment, in order to exploit a more representative situation of lipid-coating.

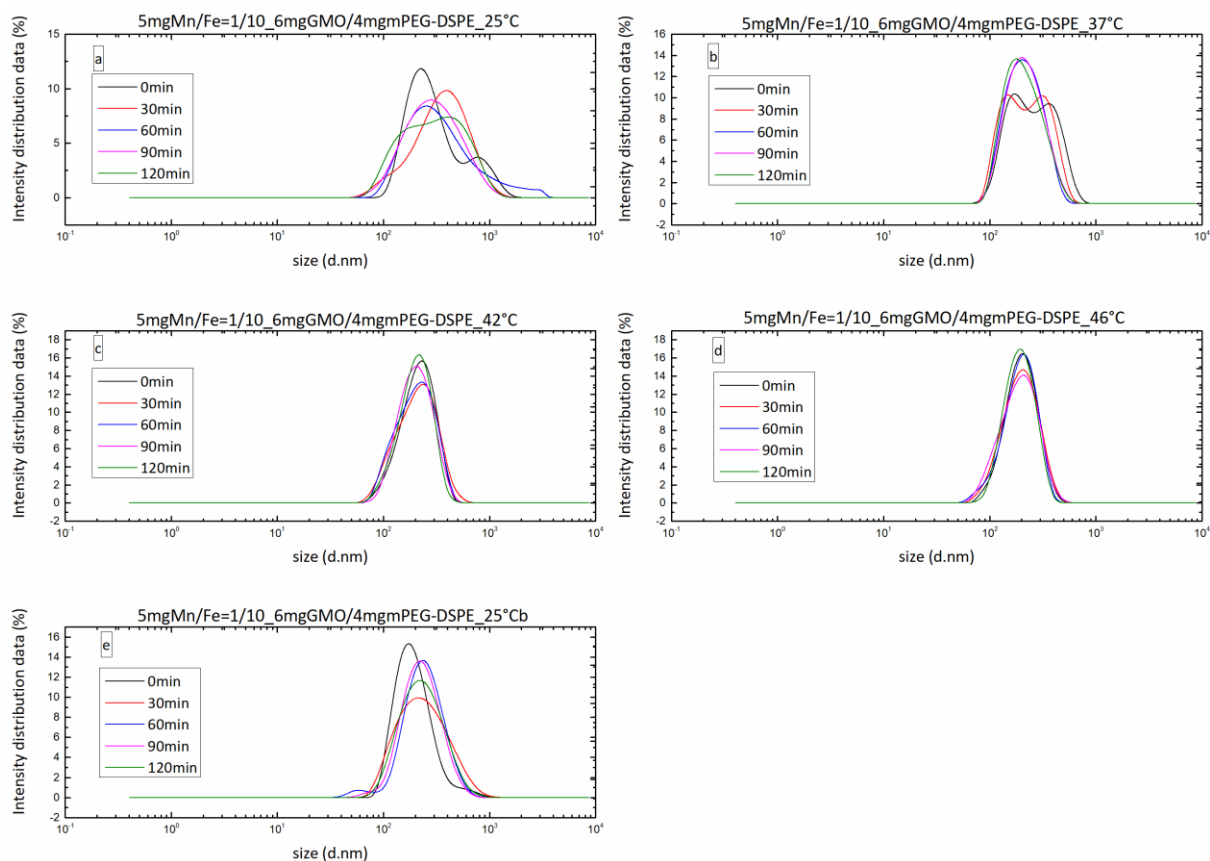


Figure 6.23 DLS stability study of FT007C, that is the sample with a coating made of 6 mg GMO and 4 mg mPEG-DSPE

6.4. The protein corona effect

The protein corona is a layer of serum proteins, lipids and small metabolites that are adsorbed on the surface of the NPs. It is characterized by heterogeneity and it evolves over time depending on the surface chemistry and degradability of the NPs [123]. With the help of advanced technologies such as a super-resolution optical microscopy, it is possible to analyze the protein corona by considering each single protein molecule involved (**Figure 6.24**).

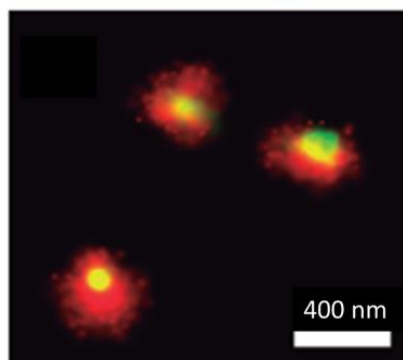


Figure 6.24 Protein corona on silica NPs observed with a super-resolution optical microscope (adapted from [123]).

In order to have a first idea about the protein corona formation, NPs were analyzed with the help of the DLS while changing the solvent between subsequent runs. After a first measurement in DMEM, the NPs were spun down 10 min at 15000 rpm at 25°C and they were re-suspended in DMEM with an additional 10% of FBS (this was repeated 3 times); the samples were analyzed and spun down again (by using the same parameters as before and repeating again 3 times); the NPs were then measured in DMEM for a second time. In this way, during the second passage the proteins created a protein corona around the NPs. This is evident in the obtained graphs reported in **Figure 6.25**. Indeed, different size populations of NPs are present when they are solubilized for the first time in DMEM. But after adding the FBS, only one population remains, showing the fact that the aggregated NPs are separated when a protein layer is created, and it acts as a barrier between the single NPs. The proteins establish quite strong interactions with the NPs because they are not eliminated by the final cleaning with DMEM: again, only one size population of NPs is present.

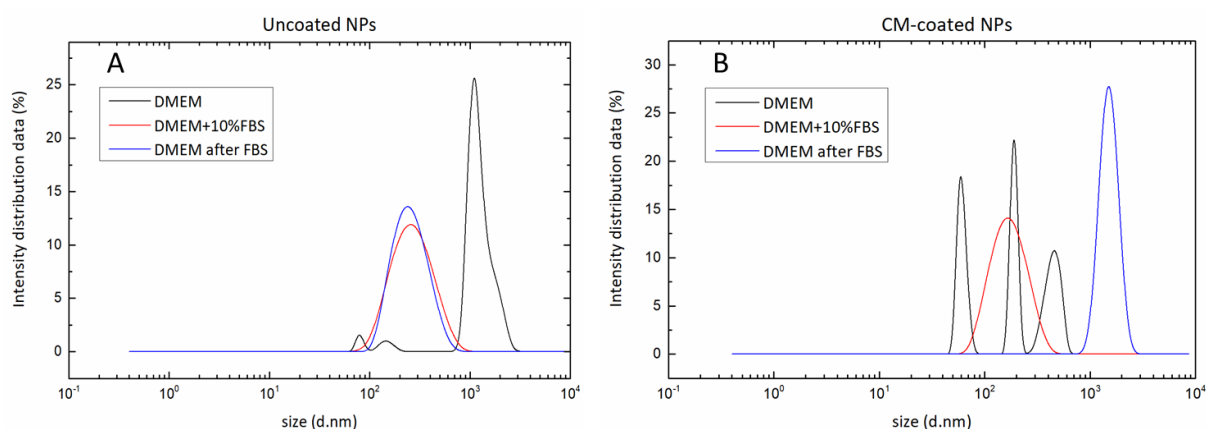


Figure 6.25 DLS measurements showing the formation of the protein corona: the NPs were analysed in DMEM, then in DMEM+10%FBS, finally again in DMEM. The proteins adsorbed during the second phase created the protein corona that stabilizes the NPs later. All the measurements were performed at 37°C.

These measurements were performed both with uncoated and CM-coated NPs: in the coated ones (**Figure 6.25-B**) the effect of the first change from DMEM to DMEM+FBS is clearer because from 2-3 populations only one is obtained when adding the FBS; in the uncoated sample (**Figure 6.25-A**), on the

contrary, is more evident the fact that the proteins do not detach from the NPs even after the DMEM cleaning. In fact, the final DLS graph is almost the same of the one in DMEM with FBS.

The protein corona formation around the NPs (uncoated and CM-coated), was also studied by using single proteins or a mixture of them, solubilized in aCSF (the composition was described in Paragraph 3.3) and measured by using DLS. aCSF was used in order to mimic a body fluid but to avoid solutions with proteins like DMEM. The parameters were set in order to increase temperature from 25°C (room temperature) to 37°C (body temperature), then 42°C (temperature at which cancer cells should start entering the apoptosis phase), then 46°C (temperature at which healthy cells start dying), and finally the temperature was decreased back to 25°C to see if the possible changes were reversible or not. For each temperature, the samples were measured at different time points: 0 min, 30 min, 60 min, 90 min, and 120 min.

The first protein to be tested was albumin, that is upregulated in CSF of GBM patients [16], and that is also the most common protein both inside the blood and inside the CSF [124]. Healthy condition values for this protein are 40.8 mg/ml inside the blood serum [125] and 0.232 mg/ml inside the CSF [126]. In the FBS added to DMEM for cell cultures, the albumin quantity is 23 mg/ml [127]. It was decided to use the same concentration of albumin that is present inside the medium used for the U-251 cells culture. As the medium is supplemented with a 10% of FBS, 2.3 mg/ml were employed in the DLS stability studies. The results (**Figure 6.26**) showed that albumin stabilizes the uncoated NPs, probably by creating a protein corona. On the contrary, CM-coated NPs in a solution with albumin (**Figure 6.27**) showed multiple size populations probably because not all of the albumin covered the NPs and some of it created albumin aggregates with a smaller hydrodynamic diameter. These results suggest that the CM coating inhibits the adhesion of proteins in the surface of NPs and the subsequent protein corona formation.

DLS stability studies were performed also with transferrin, one of the six most present proteins both in the serum and in the CSF [124]. Typical values of this macromolecule are 3.07 mg/ml inside the bloodstream [128] and 14 ng/ml in the CSF [129]. As for the albumin, the same quantity found in the cells culture medium with FBS was employed: transferrin reaches 2 mg/ml inside the FBS [130], so 0.2 mg/ml were used for the DLS stability studies. The results with transferrin showed a completely lack of stability both with the uncoated and with the CM-coated MANPs (**Figure 6.28** and **Figure 6.29**), so transferrin did not create a protein corona around the NPs.

A third protein used for the DLS measurements was ferritin, that is overexpressed both in serum [131] and in CSF of GBM patients. Inside CSF, an amount of ferritin near 100 ng/ml is present [132]. For this project, an amount between the quantity inside the CSF [133] and the one inside the FBS [134] was

used, that means 1.5 ng/ml. The results with ferritin were similar to the ones with transferrin, the system was not stable, and the protein corona was not formed. Only the stability study of the uncoated MANPs is here reported (**Figure 6.30**) because similar measurements were obtained for the CM-coated MANPs.

DLS measurements were run also with the mix of the previous proteins solubilized in aCSF, in order to see which component was prevalent. The same quantities as before were used. For the uncoated NPs it was not even possible to complete the measurements because of the unstable behavior of the system, so results are not reported, while the CM-coated NPs showed a high level of stability (**Figure 6.31**). Thus, taking into consideration all the above data it is possible to hypothesize that the mix of proteins can interact better with the nanoparticles when these are coated with a cell membrane.

The stability studies were finally performed with aCSF supplemented with 10% FBS, in order to mimic the culture conditions. In this case, both the uncoated NPs (**Figure 6.32**) and the CM-coated ones (**Figure 6.33**) showed a high level of stability, suggesting that the complexity of the protein environment is important for the NPs stability.

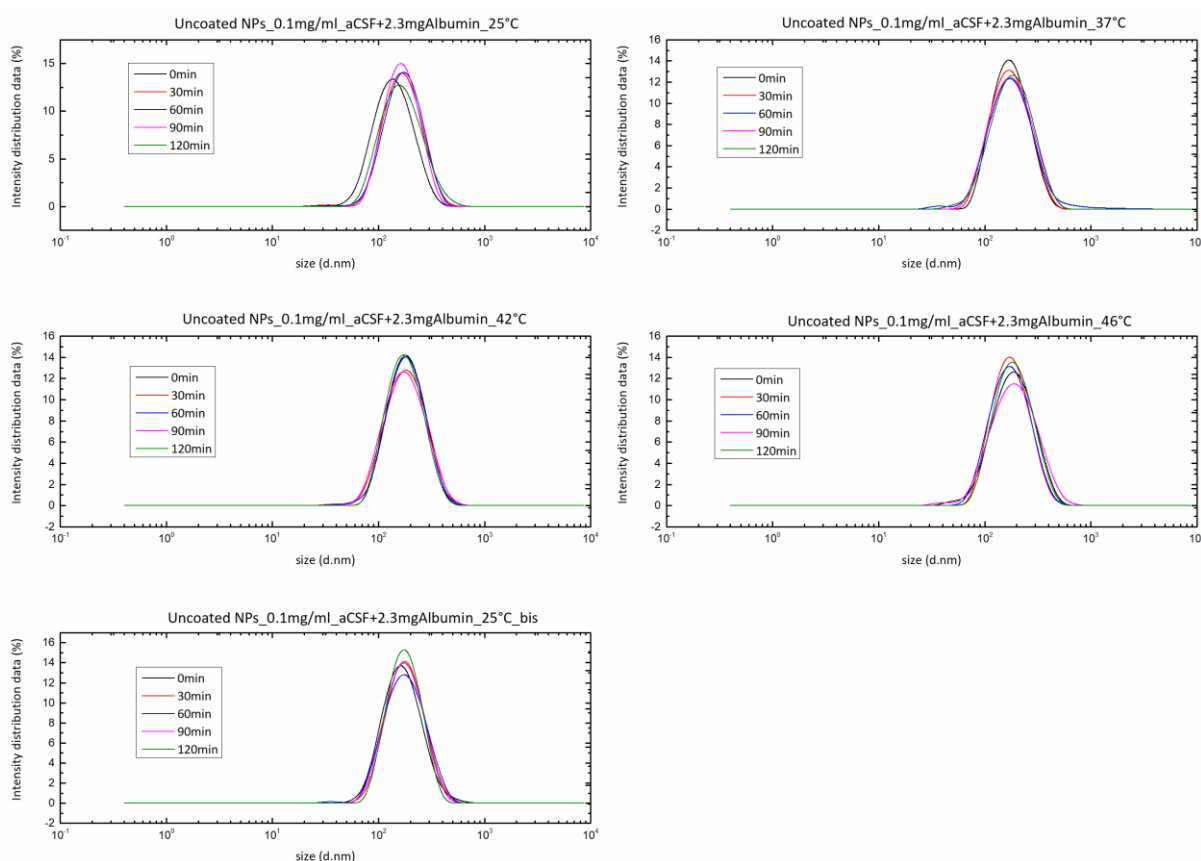


Figure 6.26 DLS stability study of uncoated NPs with albumin in aCSF.

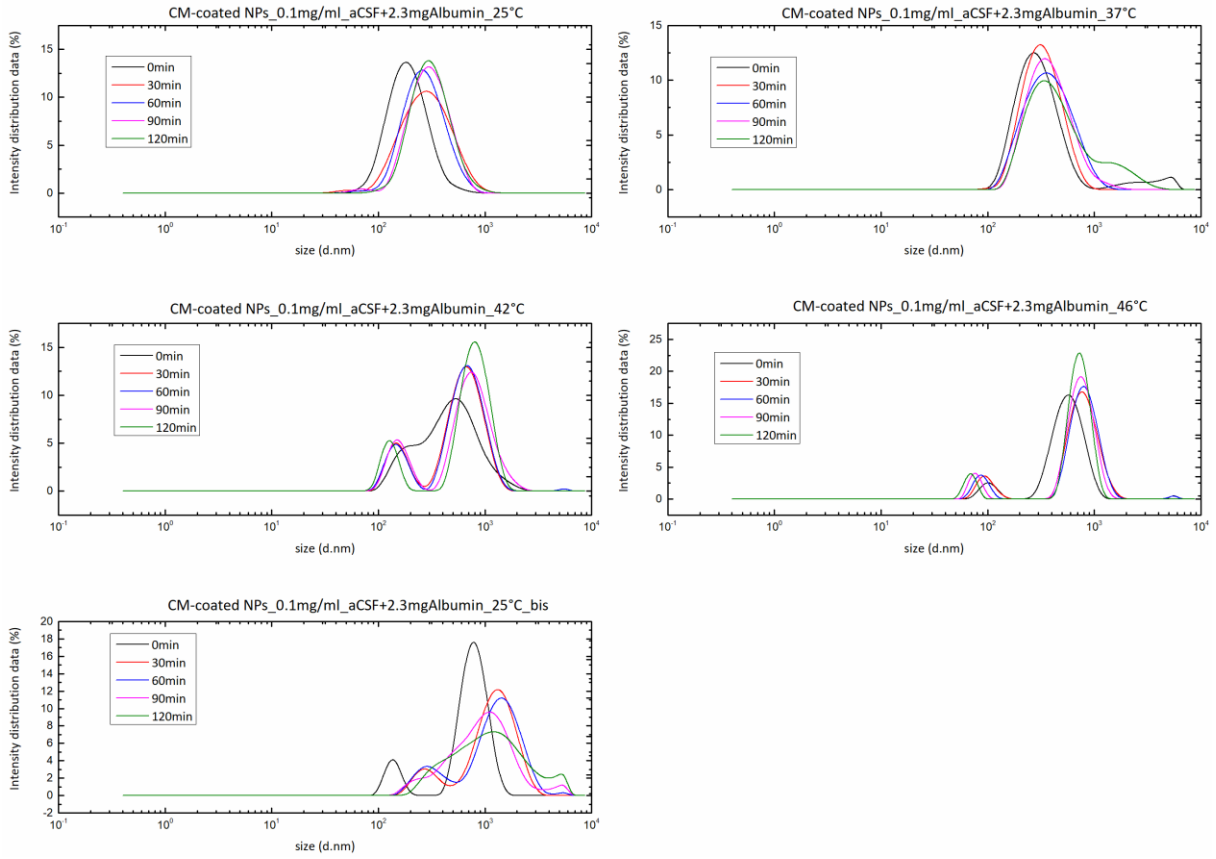


Figure 6.27 DLS stability study of CM-coated NPs with albumin in aCSF.

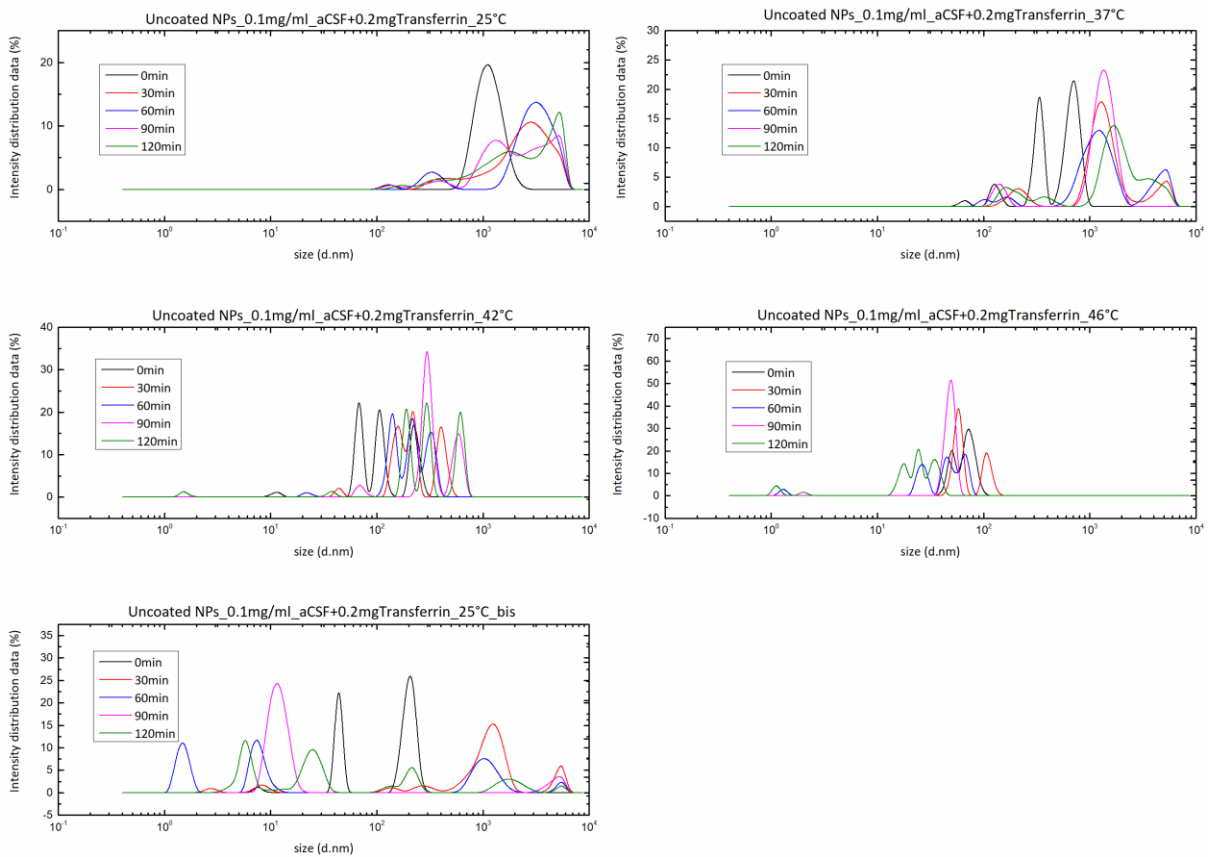


Figure 6.28 DLS stability study of uncoated NPs with transferrin in aCSF.

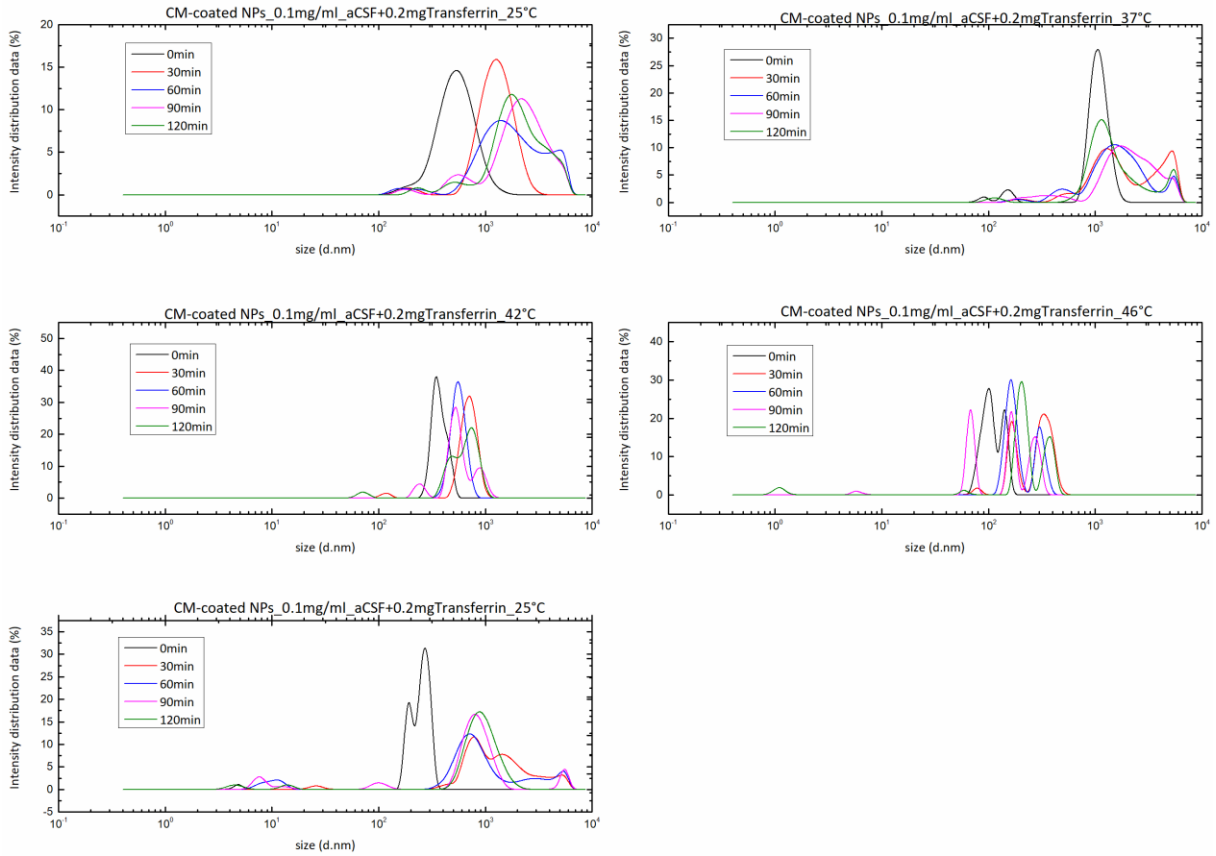


Figure 6.29 DLS stability study of CM-coated NPs with transferrin in aCSF.

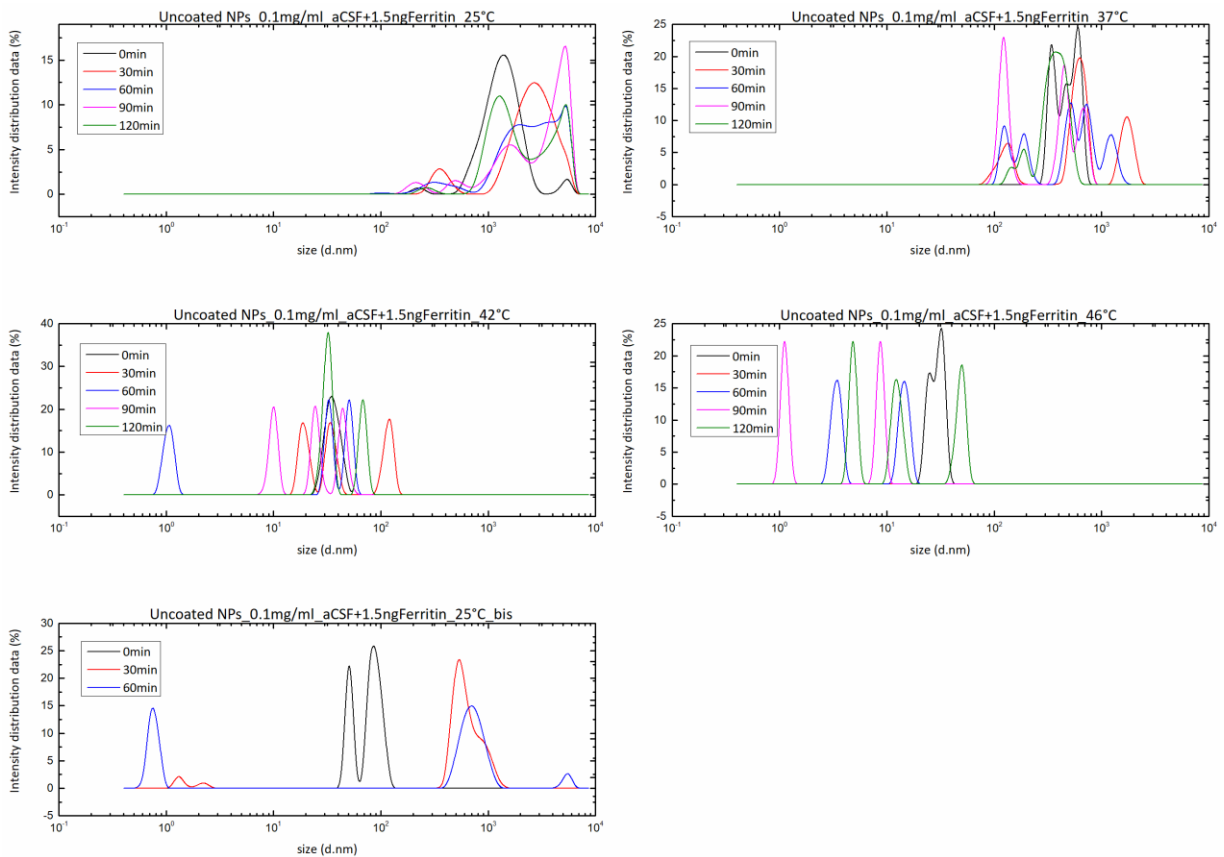


Figure 6.30 DLS stability study of uncoated NPs with ferritin in aCSF.

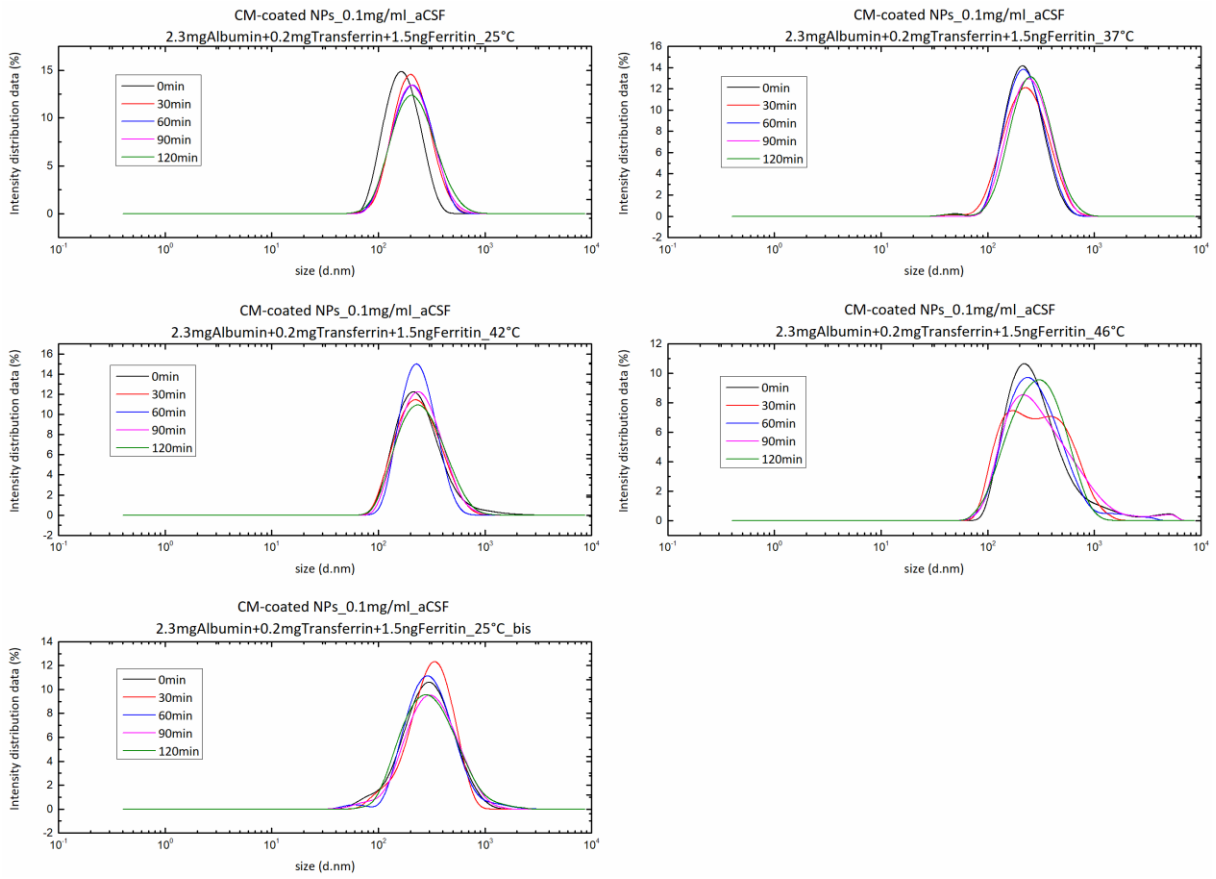


Figure 6.31 DLS stability study of CM-coated NPs with a mix of proteins in aCSF.

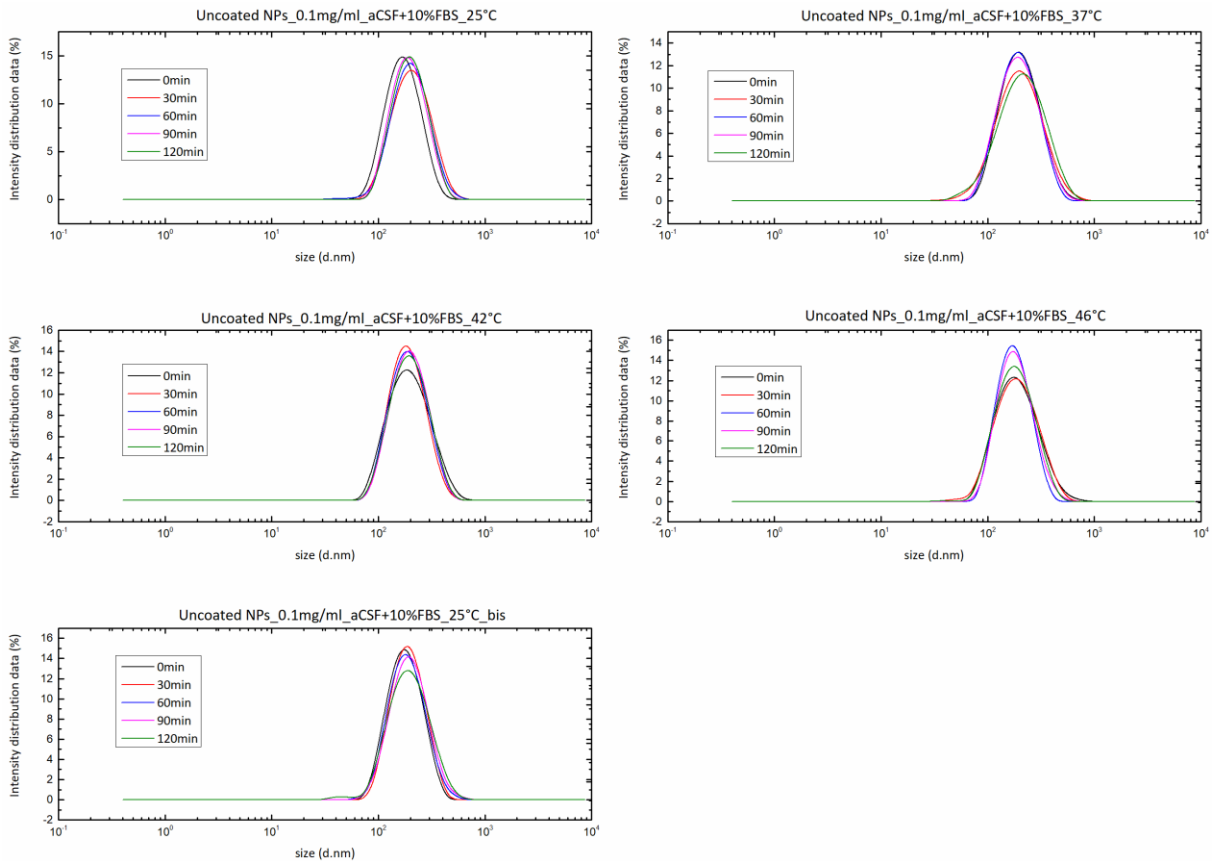


Figure 6.32 DLS stability study of uncoated NPs in aCSF+10%FBS.

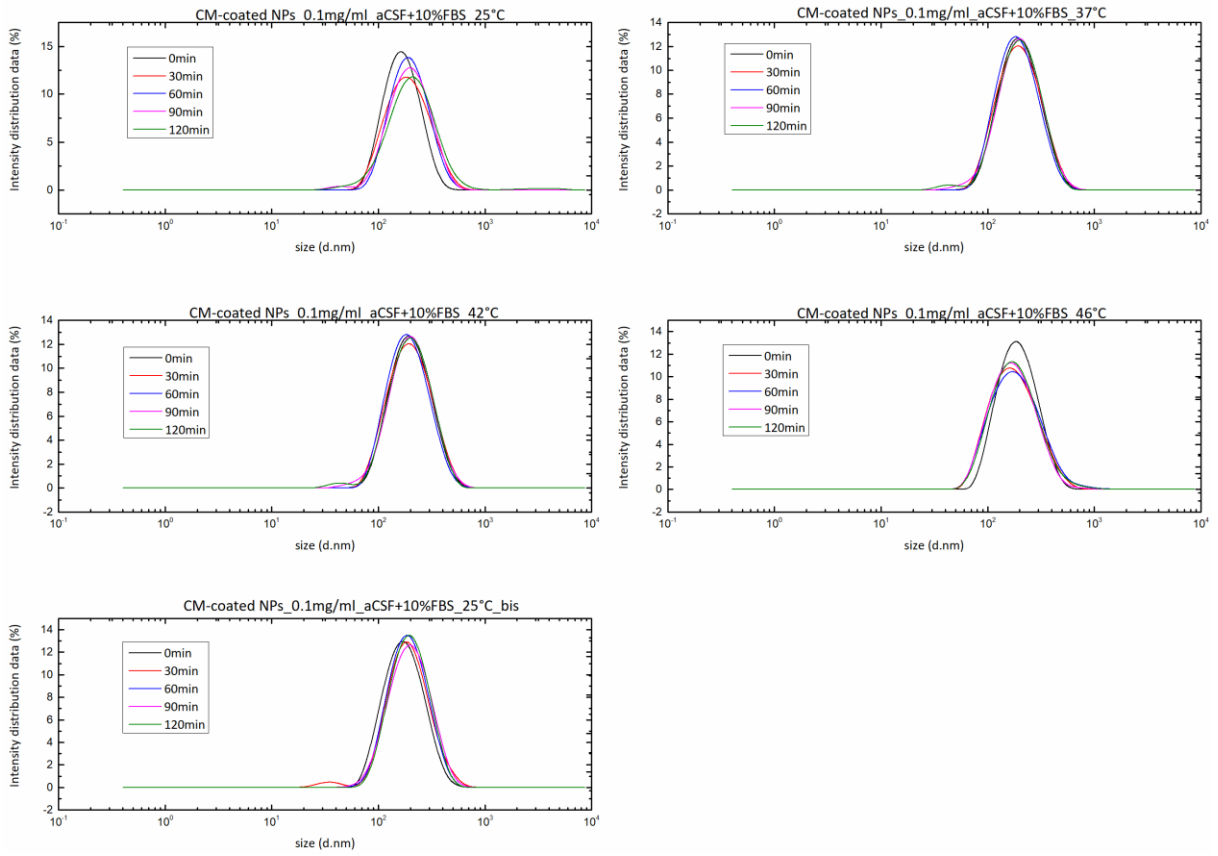


Figure 6.33 DLS stability study of CM-coated NPs in aCSF+10%FBS.

7. Hyperthermia experiments

Hyperthermia is the exploitation of temperature increase to kill the cells in the tumor site through the unfolding of their proteins [135]. Recently, it has been proven that cells die when a small but fundamental amount of proteins is destroyed, because the unfolding temperature of the majority of them is higher than the maximum one which allows cells to survive [136]. Depending on the dose-time combination of the exposure to heat, cells can undergo apoptosis or necrosis [137]. The desired temperature to reach in order to make cancer cells enter the apoptotic phase is around 42-43°C. On the contrary, healthy cells die at a temperature equal to 46°C because they are more effective in dissipating heat. MANPs' temperature was increased by applying an external alternating magnetic field.

When the NPs are exposed to an alternating magnetic field, they can dissipate the energy in the form of heat in three different ways, depending on the applied field and on the magnetic pre-history of the NPs (**Figure 7.1**). First of all, superparamagnetic materials dissipate the external magnetic field with the relaxation of the magnetic moment to its equilibrium orientation (Néel relaxation). Secondly, ferromagnetic materials generate heat through the hysteresis loss mechanism, proportionally to the frequency and the area of the loop, and dissipate the energy through the domain wall displacement due to the fact that the magnetic moments oscillate [138]. Thirdly, all the magnetic NPs produce heat because of the rotational Brownian motion inside a liquid due to the torque exerted on the magnetic moment by the external alternating magnetic field. As a consequence, in this case the viscosity of the media and the hydrodynamic diameter of the NPs are important factors.

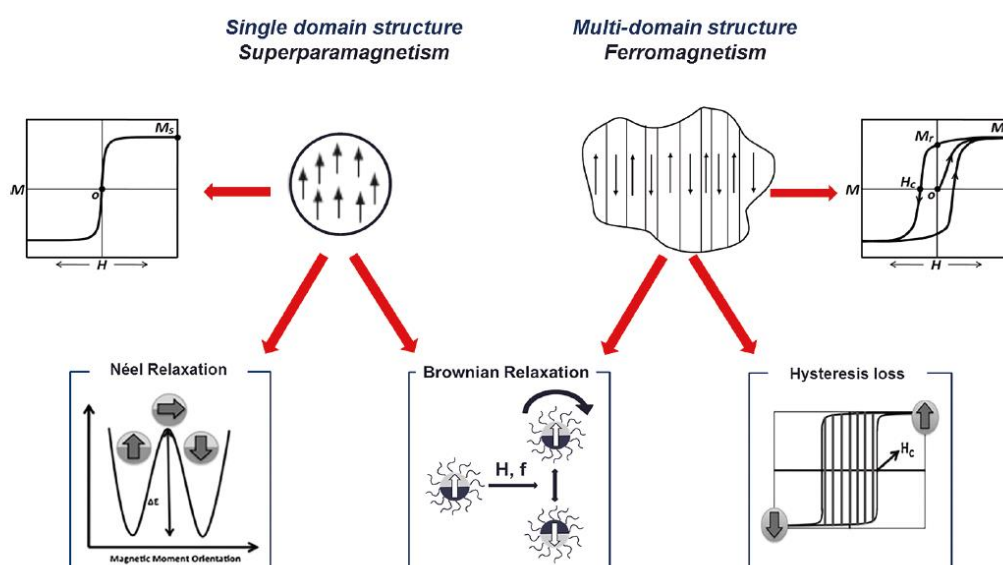


Figure 7.1 General mechanisms for heat generation of magnetic nanoparticles ([138]).

The heat created for hyperthermia through MANPs can be generated by the hysteresis losses and great resistivity in the magnetic material combined with the dielectric losses of the manganese dioxide shell. In this way, the electromagnetic waves are converted into thermal energy [75]. Their absorption depends on factors such as frequency, dimensions of the system, relative complex permittivity and relative complex permeability (where the real part represents the energy storage, while the imaginary one corresponds to the loss of the electromagnetic waves) and it happens through electron transition. The MnO₂ is important because it is responsible of the localization of electron density and more energy levels are generated near the Fermi one. Therefore, the electron transition energy is reduced, and the transition can happen at lower energy, so at lower frequencies. The CM coating is important for hyperthermia, too. In fact, thanks to its steric hindrance and by introducing repulsive forces, it prevents the NPs from aggregating. If not for the CM coating the MANPs would tend to agglomerate due to Van der Waals forces and magnetic dipole-dipole interactions generated from residual magnetic moments [139], which would lead to a decreased hyperthermia efficiency.

Two temperatures are important for magnetic materials: the blocking temperature T_B and the Curie temperature T_c . The blocking temperature is the characteristic temperature that defines the transition from ferromagnetic to thermally unstable or superparamagnetic behaviour [138].

The Curie temperature (T_c), above which the magnetic materials lose their magnetic characteristics, of the materials usually used for the hyperthermia is around 50°C [140]. By approaching the T_c , materials gradually demagnetize and lose their ability to absorb energy from an AMF [141], so having a T_c some degrees higher than 43°C could be useful in order to allow to kill the cancer cells, but to protect the surrounding tissues (self-regulated hyperthermia). It is possible to calculate the T_c of a nanoparticle of a specific material by knowing the bulk T_c of it [142]. In fact, it is possible to exploit the Equation 23.

$$\frac{T_c(bulk) - T_c(d)}{T_c(bulk)} = \left(\frac{\xi}{d}\right)^\lambda \quad (\text{Eq. 23})$$

where ξ is a constant for the correlation length of bulk phase at a temperature away from the ordering temperature, d is the diameter of the NP and λ is the shift exponent. Unfortunately, the T_c of Fe₃O₄ NPs is still too high to exploit the self-regulated hyperthermia. Indeed, T_c decreases with the diameter, but it remains near the bulk value, that is 850 K [93]. This is evident in **Figure 7.2**, where experimental results and data from a Monte Carlo simulation were reported [143].

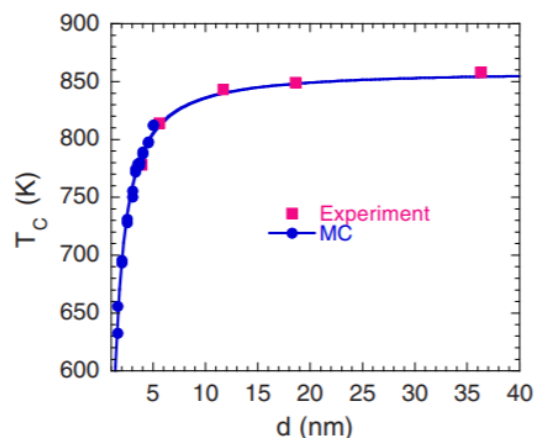


Figure 7.2 Curie temperature of Fe_3O_4 reported in the literature [143]. Both experimental data and results from a Monte Carlo simulation are shown. Even for the smallest NPs, the Curie temperature is above 600 K.

The hyperthermia experiments with the MANPs were performed by using different frequencies, different magnetic fields and different concentrations of NPs. MagneTherm™ by nanoTherics was used to create the alternating magnetic field (AMF) and record the data. With this instrument it was possible to choose among four capacitors and the corresponding frequencies (12 nF – 675 kHz, 22 nF – 470kHz, 88 nF – 240 kHz, and 200 nF – 160 kHz) and four coils (9 or 17 turns and a diameter of 44 or 56 mm). The coils with 17 turns were not used since the 9-turn ones were enough to create the desired magnetic field. Regarding the capacitors, all of them were tested and the results are reported in **Figure 7.3**. For each capacitor two frequencies were used: the maximum reachable one and a frequency around 676 kHz. This last one was chosen because it is the maximum reachable with the 12 nF capacitor when the 9 turn 56 mm diameter coil is employed, so this frequency was used as lower limit. This frequency allows to create a magnetic field of 12 mT. The samples were prepared as 2 ml of a 5 mg/ml solution of the uncoated NPs. As both an Ibidi dish and a vial were used as containers, the resulting amount of NPs per cm^2 was respectively 5 mg/cm^2 and 14 mg/cm^2 . The Ibidi dish was employed in order to test the condition similar to the one that would have been used later with the cells, while the vial was used to check the behavior of the system when it is as closer as possible to the center of the coil, where the magnetic field is maximum.

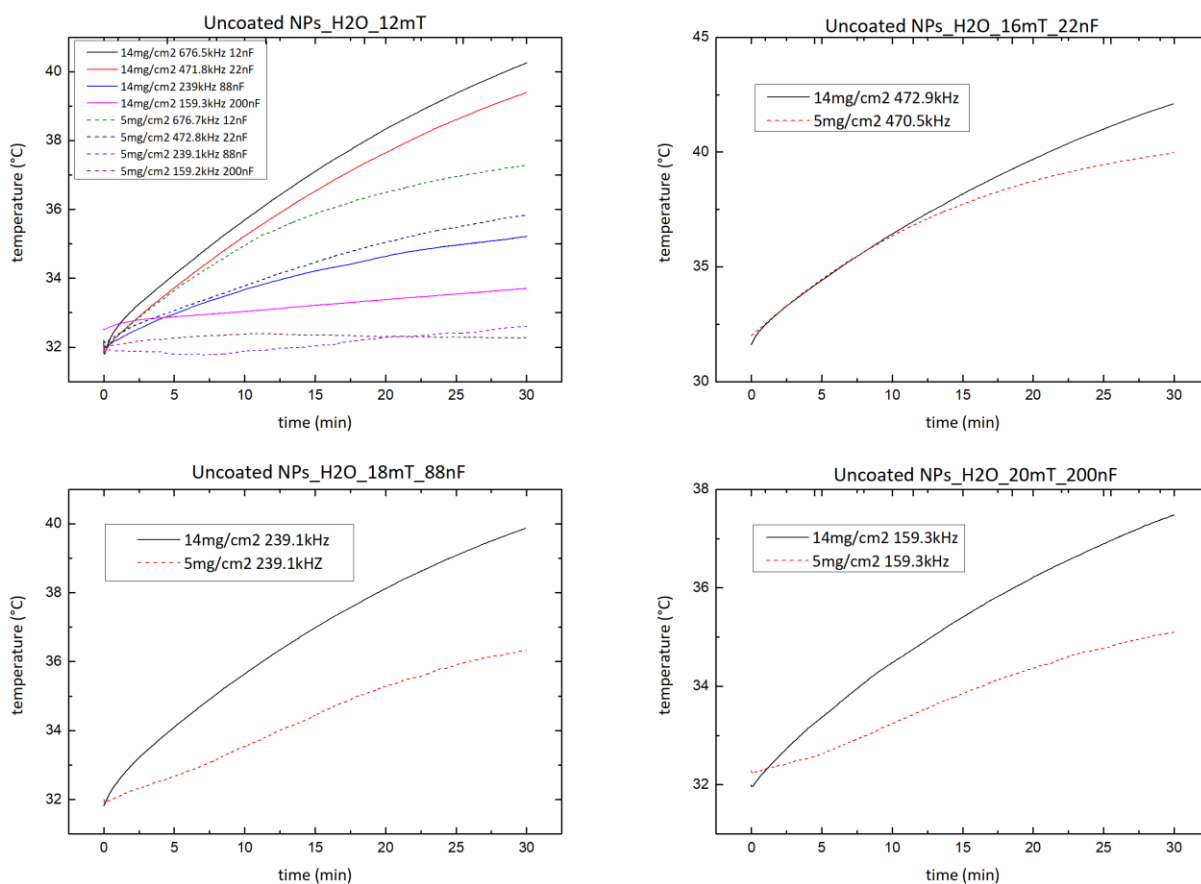


Figure 7.3 Temperature measurements of the uncoated NPs with the available capacitors and with the 9 turns 56 mm diameter coil. With each capacitor, the maximum reachable frequency and the lower useful one were applied. For every condition, two concentrations were tested.

The 88 nF (240 kHz) and 200 nF (160 kHz) capacitors did not allow to reach temperatures as high as the other capacitors did, so they were not used for the following measurements. As the 12 nF and 22 nF capacitors gave the best results, they were employed to measure the system with different solvents: deionized water, DMEM, and DMEM supplemented with 10% of FBS. The results are reported in **Figure 7.4**.

In general, similar results were obtained with the different solvents. Then, in order to run measurements to understand which coil could allow to have the best results, only deionized water was used as solvent. The tests with different coils are reported in **Figure 7.5** and the temperature was recorded for a longer time (1 h instead of 30 min).

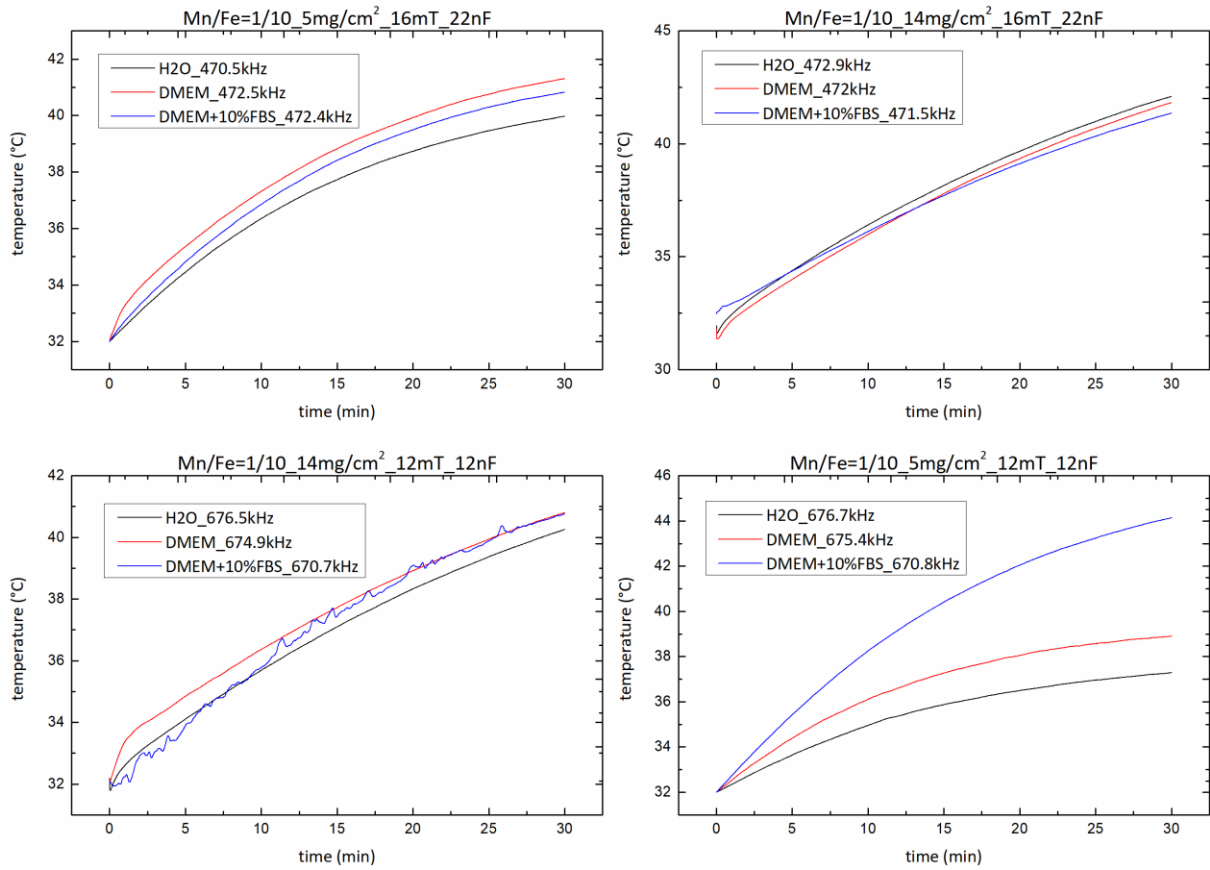


Figure 7.4 Temperature measurements of the uncoated NPs in magnetic fields equals to 12 mT or 16 mT, that are the ones created with the 9 turns 56 mm diameter coil and the 12 nF and 22 nF capacitors. Two concentrations were used because of the exploited container: in the Ibbidi dish the concentration was 5 mg/cm², while in the vial the concentration was 14 mg/cm².

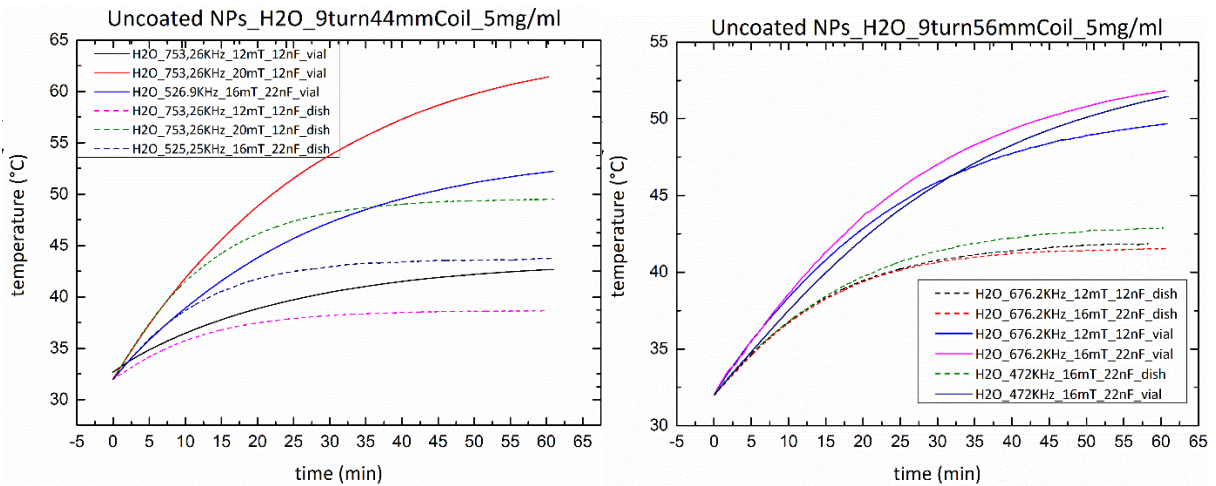


Figure 7.5 Results of the hyperthermia measurements with two different coils. On the left, data collected by using the 9 turns 44 mm diameter coil are reported. On the right, results obtained with the 9 turns 56 mm diameter coil are shown.

The best results in terms of temperature were obtained with the 9-turn 44 mm diameter coil, which allowed to reach 60°C (almost 10°C more than the maximum temperature obtained with the 56 mm coil) with the 12 nF capacitor, a 20 mT magnetic field (200 Oe) and the concentration equal to 14

mg/cm². As a consequence, these parameters were decided to be used with the cells. Then, different solvents were employed again to run more complete and biomimetic measurements with the tuned parameters (**Figure 7.6**). In general, positive results similar to the work of Babincovà et al. [144], where magnetoliposomes were stimulated with frequencies between 1 MHz and 3.5 MHz, were obtained with frequencies between 470 kHz and 760 kHz.

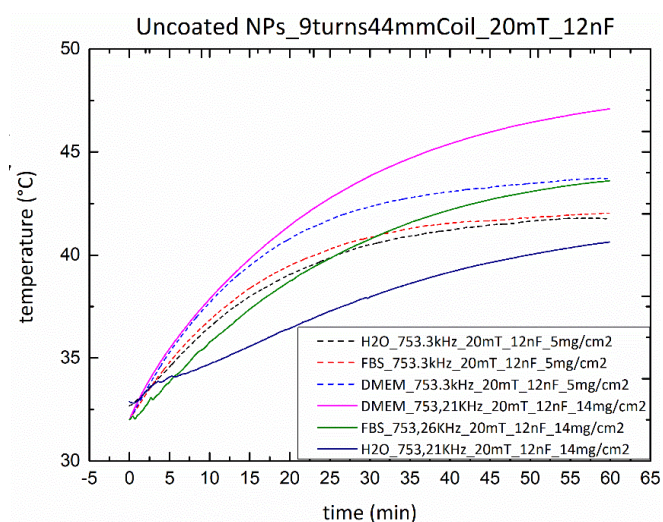


Figure 7.6 Temperature measurements of the uncoated NPs in an alternating magnetic field of 20 mT generated with a 12nF capacitor and a 9 turns 44 mm diameter coil. Different solvents were used: deionized water, DMEM and DMEM + 10% FBS.

Finally, the measurements were performed with CM-coated NPs in DMEM supplemented with 10% FBS. The data were collected for a longer period of time (2 h), but because of the instrument, a 1 min pause after the first hour let the temperature decrease of some degrees. Concerning the measurements with the sample inside the vial, one of them was run with the previously decided parameters (9 turn 44 mm diameter coil, 12 nF capacitor, 20 mT magnetic field), then the capacitor and the field were changed in order to check if the same behaviour of the uncoated system was shown (**Figure 7.7**). After this further demonstration of the parameters to set, also the experiment with the ibidi dish was performed. Data are presented in **Figure 7.8**, were results of different concentrations are reported. Again 5 mg/cm² and 14 mg/cm² were tested in order to keep the same conditions used for the uncoated NPs, but then also 2.5 mg/cm² and 7 mg/cm² (that means the half of before) were tested, in order to understand how big the difference was. Concerning the vial data, they are similar in terms of reached temperature (the higher concentration just reached 2 °C more than the lower one), but the 14 mg/cm² shows a tendency to increase more, while the 7 mg/cm² seems to be more stable on the final temperature. The difference is evident in the dish data, where by doubling the concentration it is possible to obtain an increase of more than 5 °C.

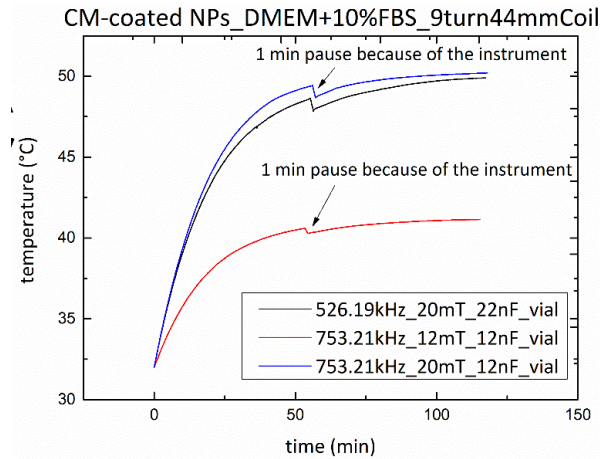


Figure 7.7 Hyperthermia measurements with CM-coated NPs in DMEM+10%FBS with the 9 turns 44 mm diameter coil. On the left, data with a bigger concentration and with different capacitors and magnetic fields. On the right, results with two concentrations in a 20mT field and with a 12nF capacitor.

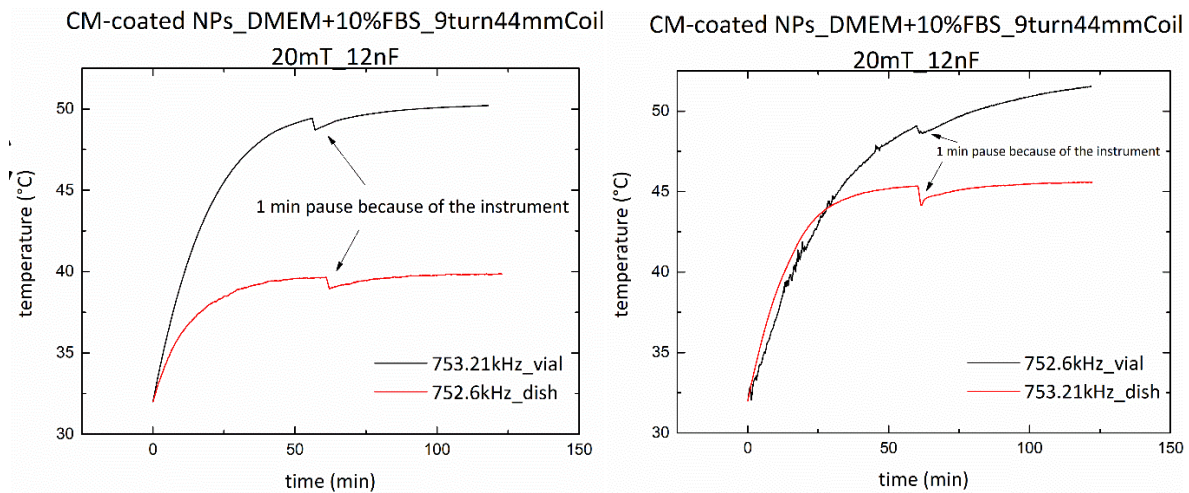


Figure 7.8 Hyperthermia measurements with CM-coated NPs in DMEM+10%FBS with the 9 turns 44 mm diameter coil, in a 20 mT field and with a 12 nF capacitor. On the left concentrations are half of the ones on the right.

Of course, the fact that the system worked for hyperthermia was the desired goal, but as the purpose of the MANPs was to solve a problem inside the human brain, it was necessary to check if the employed parameters were compatible with the safety of human body. In fact, it should be considered that the impact of the alternative magnetic field on it is connected with heating effects due to eddy currents induced in the electrically conducting tissue. It has been suggested that the upper limit for the magnetic field (the product of amplitude and frequency) should not exceed 5×10^9 A/(m*s)[145]. The main tool to determine the heating of tissues is the specific absorption rate (SAR) or specific loss power (SLP), already mentioned in Sections 3.9 and 6.1. The highest is the SAR value, the best is the system, because a lower number of NPs is required to get the same results in terms of hyperthermia. The highest SAR value measured until now is the one of magnetosomes produced from some bacteria. They are single iron oxide nanocrystals with a diameter of 20-50 nm and covered with a membrane

bilayer [146]. In order to achieve more efficient hyperthermia treatments with the same amount of NPs, it is advisable to use lower frequencies and higher magnetic field amplitudes.

SAR is defined as the amount of power absorbed by the sample per mass unit. In Equation 24, P is the absorbed power (W) and m_{Fe} is the magnetic mass inside the sample.

$$SAR = \frac{P}{m_{Fe}} = \frac{1}{m_{Fe}} \frac{Q}{\Delta t} \quad (\text{Eq. 24})$$

The absorbed power can be expressed as the energy converted into heat (Q measured in J) per time unit (s). The dissipated heat can in turn be calculated as a function of mass, both of the NPs (m_{NP}) and of the liquid medium (m_l), of specific heat capacities (c_{NP} and c_l) and of temperature variation ΔT (Equation 25).

$$Q = (m_{NP}c_{NP} + m_l c_l) * \Delta T \quad (\text{Eq. 25})$$

Then, SAR can be calculated through Equation 26.

$$SAR = \frac{(m_{NP}c_{NP} + m_l c_l) \Delta T}{m_{Fe} \Delta t} \approx \frac{(m_l c_l) \Delta T}{m_{Fe} \Delta t} \quad (\text{Eq. 26})$$

The increase in temperature with respect to time is the maximum value of the gradient of the temperature curve [147], which normally corresponds to its initial gradient. Thus, the first 20s of the experiments were considered as time step to do these calculations. Equation 26 can be simplified by assuming $m_{NP}c_{NP} \ll m_l c_l$. Moreover, the density of the liquid (δ_l) was used instead of its mass and density of DMEM+10%FBS was approximated with the density of water. As a consequence, instead of using the magnetic mass, the concentration of the magnetic moiety was employed (C_{Fe}).

SAR values were finally calculated for both uncoated and CM-coated MANPs, by using Equation 27.

$$SAR = \frac{\delta_l c_l}{C_{Fe}} \left(\frac{dT}{dt} \right)_{max} \quad (\text{Eq. 27})$$

The following values of the constants were used:

$$\delta_l = 7.05 \text{ mg/ml}$$

$$C_l = 4.186 \frac{J}{g \text{ } ^\circ C}$$

$$dt = 20 \text{ s}$$

Table 7.1 SAR values for uncoated and CM-coated MANPS.

Sample	C _{Fe} (mg/ml)	dT (°C)	dT (°C)/dt (s)	SAR (W/g)	SAR (W/kg)
Uncoated_5mg/cm ²	3.36	0.20	0.010	0.088	87.83
Uncoated_14mg/cm ²	3.36	0.12	0.006	0.053	52.70
CMcoated_5mg/cm ²	3.13	0.27	0.014	0.127	127.49
CMcoated_14mg/cm ²	3.13	0.25	0.013	0.118	118.05

Another important parameter to consider was the intrinsic loss power (ILP), that was calculated by exploiting Equation 28 [148].

$$ILP = \frac{SAR}{fH^2} \quad (\text{Eq. 28})$$

where SAR is expressed in W/g, frequency in Hz and the magnetic field in A/m. In this case, the frequency was 753 kHz and the magnetic field 20 mT (16000 A/m). The results are reported in **Table 7.2**, but ILP values are extremely low if compared with the commercial Fe₃O₄ (Feridex® ILP = 0.15 nHm²/kg) [149].

Table 7.2 ILP values

Sample	ILP (Hm ² /g)	ILP (pHm ² /kg)
Uncoated_5mg/cm ²	4.56*10 ⁻¹⁶	0.456
Uncoated_14mg/cm ²	2.73*10 ⁻¹⁶	0.273
CMcoated_5mg/cm ²	6.61*10 ⁻¹⁶	0.661
CMcoated_14mg/cm ²	6.12*10 ⁻¹⁶	0.612

8. Loading with temozolomide

Drug release systems are commonly referred as “smart drug delivery systems” if it is possible to control the release of encapsulated therapeutic molecules. Different drug delivery platforms at the nanoscale including, liposomes, liquid crystals (surfactants and polymers), and nanoparticles (polymeric, lipid, inorganic and others) have been presented in the literature [150]. MANPs are part of the third group, presenting several advantages, among of which the most important one is the fact that they allow the delivery of the right amount of drug into the correct site of the body. Another advantage of these systems is that they reduce the side-effects presented on healthy cells, since there is a specific targeting towards cancer cells that inhibits the accumulation of the drug into healthy cells and tissues. In addition, these systems present controlled and sustained release increasing the overall therapeutic efficacy. Indeed, the right concentration of drug must be kept: it has to be enough to be therapeutic, but not too much not to become toxic for the body. Indeed, with the standard administering of the medicines, drug concentration into the site of action is not constant and it is not always in the so-called therapeutic window, but it has a peak that can exceed the toxic limit and then it falls under the minimum therapeutic level. This implicates that bigger quantities of drug are necessary in order to provide for the systemic losses and more frequent injections are requested, with the consequent side effects. NPs assure the right amount of drug to be delivered to the disease site. Finally, the drug is not free in the bloodstream, so it is protected by the action of the enzymes that otherwise could destroy it before it performs the therapeutic action. In this way, the NPs improve the biological half-life of the drug and reduce the clearance, so lower doses of the drug can be administered and there are fewer side effects. All these advantages lead to a better efficacy of the drug.

Drug delivery NPs can be generally divided into two groups: capsules and spheres. Capsules are reservoirs in which the drug is protected by a layer and they usually have a liquid core; spheres (or matrix systems) have the drug sprinkled into all the structure of the NP. MANPs have some properties of the capsules, such as a protective layer represented by the lipids or the cell membrane coating, and some of the spheres because they have not got a liquid part.

In general, the loading can take place as precipitation during the NPs' synthesis or it can be performed later exploiting the diffusion phenomenon. For MANPs loading, the second option was followed, by taking advantage of the porosity of the NPs and of the chemical nature of the drug. Indeed, TMZ is hydrophobic, so it is energetically pushed to enter the NPs inside an aqueous solution.

The TMZ loading protocol for the MANPs was really easy: 10 mg of uncoated NPs were dispersed in deionized water and sonicated 5 min at 50% amplitude. Then 4 mg of TMZ were added, and the solution was sonicated again 5 min at 50% amplitude. The solution was left 24 h under shaking. The

cell membrane derived from 50 million cells was added and the final solution was sonicated 30 min at 60% amplitude at 4°C. Three cleanings were realized with deionized water and 1h of spinning at 16000 xg (15000 rpm).

The supernatants of the cleaning were kept and analyzed with a HPLC Shimadzu LC-20AT. The chromatographic separation was carried out using a C-18 column (150 mm × 4.6 mm i.d., 5 µm particle size). The mobile phase consisted of 60% v/v methanol (MeOH) and 40% v/v water (containing acetic acid 1% v/v) and it was pumped with a steady flow rate of 0.5 ml/min. The standard curve was prepared with serial dilutions at concentrations ranging from 7.8 ug to 300 µg. The elution of the analyte was monitored at 300 nm and at 3.8 min.

Two parameters were calculated from the results. The encapsulation efficiency (EE) is the amount of drug encapsulated in the NPs (derived by subtracting the drug measured in the supernatant from the amount weighted at the beginning) divided for the initial amount of drug put in the solution with the NPs (Equation 29). The loading efficiency (LE), also called dynamic loading (DL), is the amount of encapsulated drug divided for the total amount of material (NPs and drug), thus it shows how much of the final system is represented by the drug (Equation 30). Both these parameters are expressed as percentages.

$$EE(\%) = \frac{\text{Loaded drug (mg)}}{\text{Initial weighed drug (mg)}} = \frac{\text{Initial weighed drug} - \text{Drug in the SN}}{\text{Initial weighed drug}} \quad (\text{Eq. 29})$$

$$DL(\%) = \frac{\text{Loaded drug (mg)}}{\text{Loaded drug (mg)} + \text{NPs used(mg)}} \quad (\text{Eq. 30})$$

The encapsulation efficiency and the dynamic loading results were the following:

$$EE = 73.47\%$$

$$DL = 17\%$$

The EE was 6% higher than the best value found in the literature and it was almost the double of the other data found in recent papers [151-153], so the loading was definitely considered successful.

9. Release studies

In general, the release of the encapsulated drug from NPs can occur in many ways: it can happen through simple diffusion, with a chemical control (the solubilization of the NP's matrix or the action of an enzyme that cut the bonds between the medicine molecule and the NP), thanks to the activation through the solvent (pH, temperature or salt concentration), or it can be due to a stimulus.

MANPs follow the last two options: it was fulfilled with a diffusion method together with the pH conditions change and it was controlled with an external magnetic field. Indeed, the release was obtained both because of the decreased pH in the tumor environment and with the help of an external alternating magnetic field that made the NPs increase their temperature. The heat is responsible for the changes and collisions among the molecules of the coating. For temperatures near the melting one of the membrane, that depends on the lipid composition, the cell membrane becomes more permeable (with too high temperatures it is denatured and damaged) [93]. The AMF does not only let the NPs increase the temperature, but it can also suppress the interactions between the drug and the carrier and it accelerate the diffusion.

The release should be measured in different pH solutions and at different time points in order to test the different conditions that the NPs will face. A solution with pH equal to 7.4 is useful to check the release in conditions similar to the ones of the blood, a pH=6 solution is important to simulate the extracellular and intracellular environment of the cancer cells, while a pH=4.5 solution can be exploited to check the release as it would happen into the lysosomes. Because of the limited available period of time, only the conditions at the extremes were checked.

The sample used for the loading (10 mg NPs with 4 mg TMZ) was divided into 4 parts for the 4 different conditions (pH 7.4, pH 7.4+Hyperthermia, pH 4.5, pH 4.5+Hyperthermia) to test. They were spun down and re-suspended in solutions with the proper pH. For the pH 7.4 PBS was exploited, while for pH 4.5 a 0.05 M phosphate buffer solution was prepared by dissolving 340 mg of potassium dihydrogen phosphate (KH_2PO_4) in 50 ml of deionized water.

For the first 72h the samples that underwent hyperthermia were inside the AMF for 2h and their temperature increase was recorded (44-45°C were reached). All the sample were kept at 37°C when not exposed to the AMF. At each time point (8h, 24h, 48h, 72h, 144h, and 196h), the samples were spun down, the supernatants were collected for HPLC analyses and the samples were re-suspended in the corresponding solutions.

The data collected with the HPLC were used to calculate the release profile, by following Equation 31.

$$\begin{aligned} \text{Cumulative release}_i(\%) &= \\ &= \frac{\text{release}_1 + \text{release}_2 + \dots + \text{release}_{i-1} + \text{release}_i}{\text{loaded drug}} * 100 \end{aligned} \quad (\text{Eq. 31})$$

where i is the considered time point. Results are reported in **Figure 9.1**.

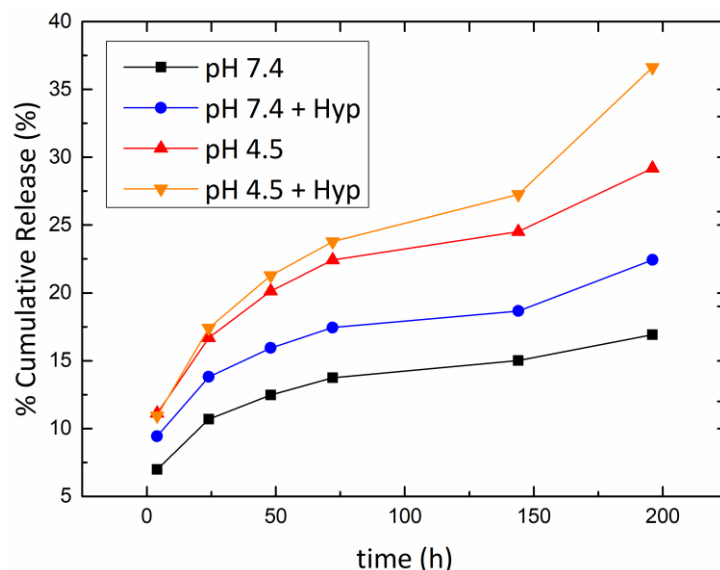


Figure 9.1 Release profile of TMZ from the CM-coated MANPs

The release profile seemed not to show a burst release. The drug was released slowly, ensuring an extended therapeutic effect of the system. Moreover, the role of the temperature increase was proved by the higher releases of the NPs that were stimulated with the AMF than the release of the NPs without hyperthermia. It has to be noted also, that the release in pH 4.5 was almost the double of the one in pH 7.4, meaning that the release would be more efficient once the CM-coated MANPs would be found inside the acidic organelles of the U251 cells.

PART II: *in vitro* studies

In 1933 GBM cells started to be studied from surgically removed tumors [154], but they were difficult to maintain. Only in 1968 Ponten et al. [155] established a set of glioma cell lines. Even if cell lines do not represent accurately primary GBM cells, they are similar enough in order to perform *in vitro* studies and have reliable results. For this thesis project, U-251 MG (formerly known as U-373 MG) ATCC® HTB-17™ (ECACC 09063001) line cell, derived by human glioblastoma astrocytoma, was used to perform the majority of the *in vitro* experiments. These cells represent only one of the many GBM cell lines, each of which is characterized by a different pattern of proteins into the cell membrane and a different ECM. Belot et al. [5] analyzed ten different glioblastoma cell lines and found a high proportion of thrombospondin-immunopositive cells in all of them and low percentages of vitronectin-immunopositive cells. They also observed that all the cell lines expressed the $\beta 8$ integrin subunit. Among the ECM components, laminin was the most present in the major part of the cell lines. Examples of other GBM cell lines are U87, U118 and A172. Proteomic patterns of these cell lines have been compared to U251 one and to primary GBM samples in a study [156] which showed that almost 160 proteins were gained and 60 were lost on culture. Each cell line has only 5-10 unique proteins, while all the cell lines share more than 100 proteins.

For the internalization studies other three cell lines were also employed: SH-SY5Y (ATCC® CRL-2266™), which are human neuroblastoma cells taken from bone marrow; C8-D1A (ATCC® CRL-2541™), healthy astrocytes taken from murine brain; bEnd.3 (ATCC® CRL-2299™), which are murine endothelial cells of the brain and the cerebral cortex.

U-251 MG, C8-D1A, and bEnd.3 were cultured in Petri dishes using high-glucose DMEM supplemented with 10% FBS, 1% penicillin/ streptomycin, and 1% L-glutamine, while SH-SY5Y were cultured in DMEM/Nutrient Mixture F-12 (containing 15 mM HEPES) again supplemented with 10% FBS, 1% penicillin/ streptomycin, and 1% L-glutamine. For all the cell lines, normal culture conditions (37 °C, 5% CO₂) were employed and the medium during culture was changed every 2-3 days. In order to split them when 80% confluent, trypsin was used with U-251 MG, bEnd.3 and SH-SY5Y, while with C8-D1A a scraper was employed to detach the cells from the dishes.

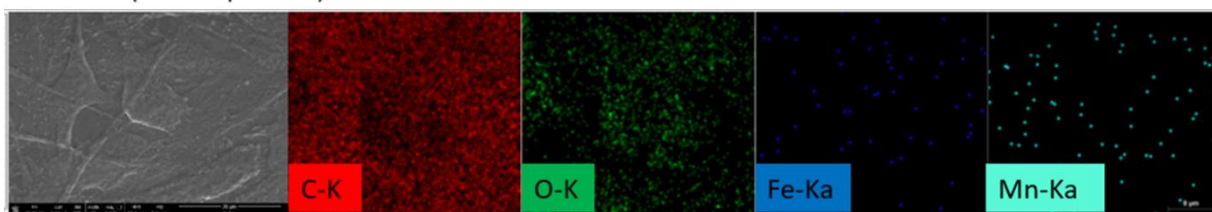
10. Internalization

A first test to understand if MANPs could be uptaken by cancer cells was observing if they were able to be attached or to be localized near them. In order to do this, 50000 U-251 cells were seeded on 2 cm² wells (24 multiwell plates) with high-glucose DMEM supplemented with 10% FBS, 1% penicillin/streptomycin, and 1% L-glutamine. After 1 day the cells were treated with 100 µg of uncoated NPs (a control sample was also realized, without NPs). The samples were fixed at 24 h: they were washed with PBS, then paraformaldehyde (PFA) diluted 4% v/v was added and the samples were kept 20 min at 4°C; finally, they were washed with PBS again. In order to observe cells with SEM, a special protocol was followed to prepare the samples:

1. Clean with deionized water to remove salts
2. Put glutaraldehyde 4% and leave it 2 h at 4°C
3. Wash with ethanol 25% 5 min
4. Wash with ethanol 50% 5 min
5. Wash with ethanol 75% 5 min
6. Wash with ethanol 100% 5 min
7. Remove the ethanol and sputter with gold (30 mA, 60 s)

At this point, the samples were observed with SEM and pictures were taken (**Figure 10.1**). It is evident that MANPs are present and that they localize near and on the top or inside the cells. According to the EDS analysis, the percentage of iron went from 0% in the sample without MANPs to 4.38% in the sample treated with uncoated MANPs. Manganese increased from 0% to 0.26%.

U251 CTRL (without particles)



U251+FT012A (uncoated NPs)

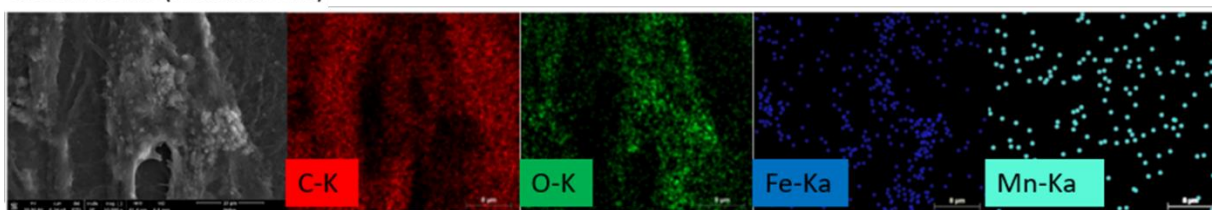


Figure 10.1 SEM image of cells without (on the top) and with (on the bottom) uncoated NPs.

A second and more complete experiment about internalization was later performed. Four cell lines were used: U-251 MG, SH-SY5Y, C8-D1A and bEnd.3. The internalization was tested both with CM-

coated NPs and with lipid coated ones, and 2 time points were considered: 4h and 24h. The aim of this experiment was to check if the CM coating could improve the uptake of the NPs and if it allowed to selectively recognize the GBM cells with respect to other brain cancer cells (SH-SY5Y), with healthy brain cells (C8-D1A), and with endothelial brain cells (bEnd.3).

Four samples for each cell line were prepared, in order to have for each time point a specimen with CM-coated NPs and one with lipid-coated NPs. For every sample, 50000 cells were seeded on a round glass for microscopy (4.9 cm²). In order to do this, all the glasses were washed with ethanol, treated with gelatine 1% and left 30 min at 37°C, washed with PBS and with medium, and then seeded. For each cell line the proper medium was used, but for the SH-SY5Y a different medium specific for this cell line was employed to make the stem cells differentiate: high-glucose DMEM supplemented with 1% FBS, 1% penicillin/ streptomycin, 1% L-glutamine, and 1:1000 retinoic acid. Samples were then treated with 100 µg of coated MANPs. Concerning the lipid-coated ones, the NPs with a coating made of cetyl palmitate, glyceryl monooleate, and mPEG-DSPE (sample FT007B of section 6.3) were employed.

At each time point, the samples were fixed by removing the medium, washing with PBS, adding PFA 4% and keeping them 20 min at 4°C. Then they were washed and kept with PBS. When the specimens of all the time points were ready, they were stained with Invitrogen™ Rhodamine Phalloidin, a red dye (Tetramethylrhodamine Isothiocyanate - TRITC) by ThermoFisher Scientific that localizes the actin of the cytoskeleton, and with Hoechst 33342 Solution (20 mM) again by ThermoFisher Scientific, a blue dye that localizes the nucleus of the cell. The staining protocol imposes to remove the PBS from fixed samples, by adding PBS with 10% of goat serum (GS) and leave it at room temperature for 40 min. Then replace the solution with a similar one supplemented with the desired dyes (1:1000 for both of them) and leave it 90 min at 37°C, then wash with PBS.

The samples were finally ready to be observed with the confocal microscope: images were taken and three-dimensional (3D) rendering of z-stacks were performed by using NIS-Elements software (Nikon).

In order to have also a quantitative analysis of the internalization experiment, a parallel study of flow cytometry was performed with a CytoFLEX by Beckman Coulter. The same cell lines were employed, and they were cultured as abovementioned. In this case, 24 multiwell plates were used and 50000 cells were seeded in every well. For each cell line, half of the samples were treated with CM-coated NPs and the rest of them with the lipid-coated NPs. Aiming at avoiding the saturation of the fluorescent signal in the flow cytometry measurements, instead of using 100 µg of MANPs for each sample, only 10 µg were used (5 µg/cm²); green DiO was used to stain the NPs. As controls untreated cells were used. The samples were analyzed after 4h and 24h.

At each time point, the cells were washed three times with PBS. The medium removed was collected and analyzed with the absorbance reader. As the wells were too small to use the scraper, all the cell lines were trypsinized. White medium was used to block the trypsin action and a good pipetting was performed. The cells were then put in Eppendorf tubes and spun down for 5 min at 445 xg (2000 rpm). The supernatant of each sample was removed and replaced with 500 µl of PBS. After a good pipetting, the samples were measured with the flow cytometer.

The results concerning internalization in U-251 are reported in **Figure 10.2**, and they showed that CM-coated MANPs are strongly uptaken by this cell line. Indeed, during the first 4h already 66% of the NPs were inside the cells and 86% after 24h were internalized. By comparing these results with the lipid-coating NPs, it was possible to notice that at the beginning only 36% of the lipid NPs were uptaken, almost half of the CM-coated ones. This big difference could of course be useful for the treatment of a patient that after the MANPs administering would need only few hours before the hyperthermia induction with an alternating magnetic field. However, after 24 h it was not possible to see a different uptake level between the two NPs.

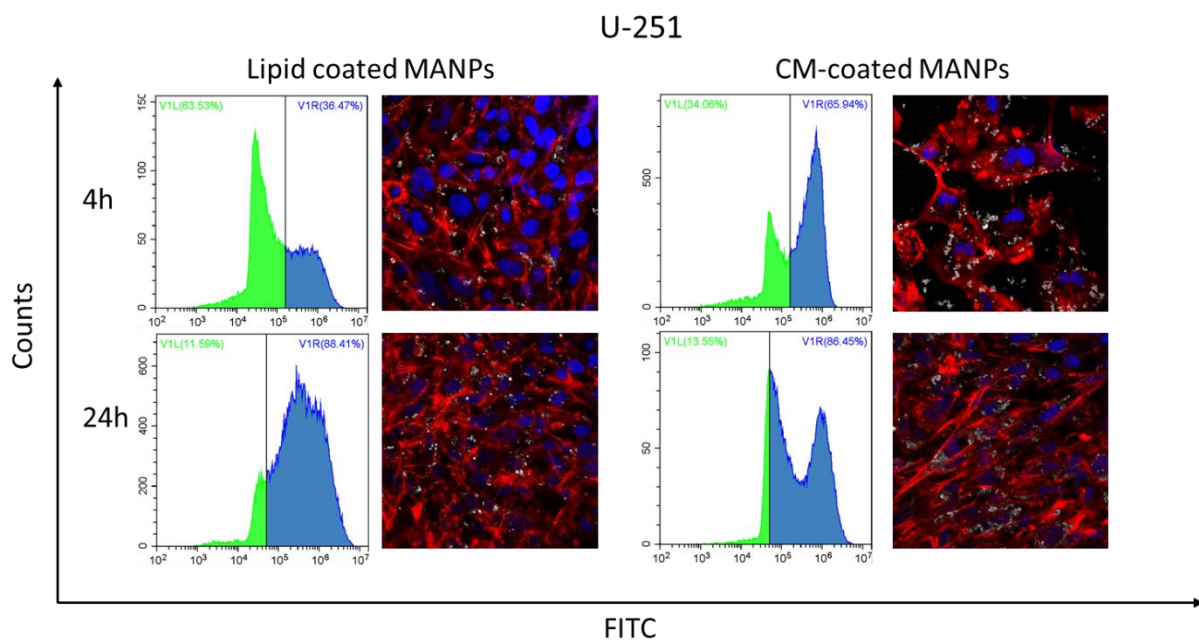


Figure 10.2 Internalization results with U-251 cell line.

The uptake of NPs by bEnd3 cell line was also high (**Figure 10.3**) and it reached 94% after 24h of incubation of the CM-coated MANPs with the cells. This is a good result because bEnd3 are endothelial cells, which are the type of cells that the NPs meet in the BBB. Thus, a strong internalization by this cell line was a promising data for the BBB successful crossing. In this case, the lipid-coated NPs were better uptaken by the cells after 4h, but the difference was around 15%. However, after 24h the level of NPs inside the cells was the same for the two types of coated MANPs.

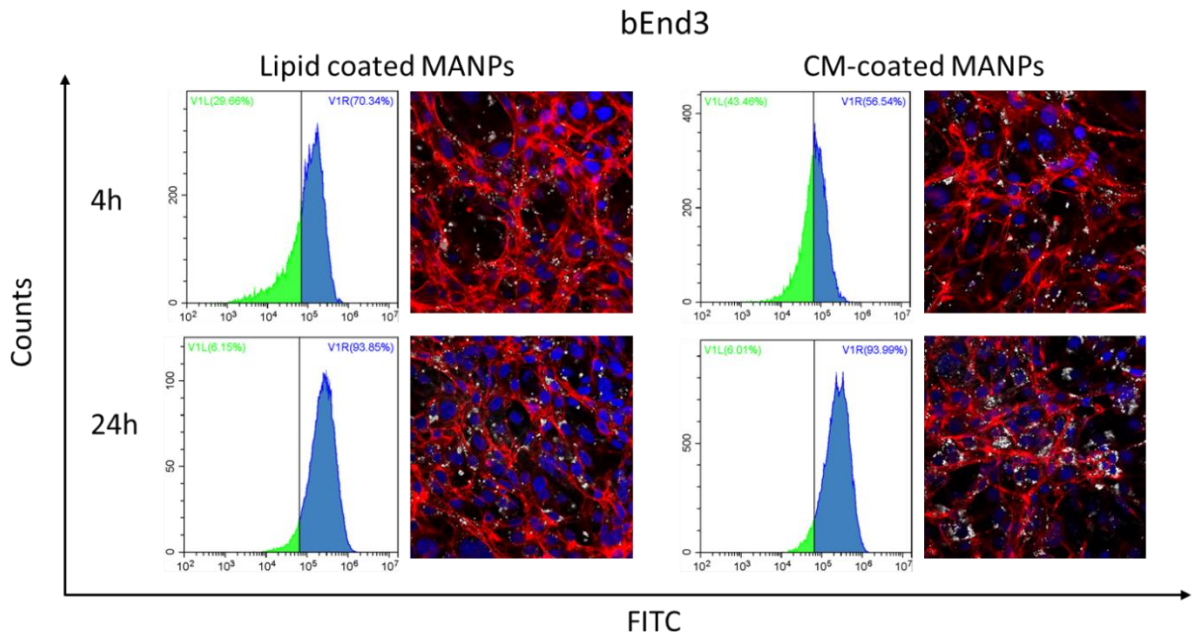


Figure 10.3 Internalization results with bEnd3 cell line.

The results of the internalization with the healthy astrocytes are reported in **Figure 10.4**. After 24h the uptake of CM-coated MANPs was the double of the one of lipid-coated NPs, 86% and 43% respectively. This means that the coating with the cell membrane taken from tumor cells was a good targeting for all the astrocytes, both healthy and cancerous ones, probably because the composition of the cell membrane does not change significantly when cells become cancerous, thus they can both recognize the CM-coated MANPs in the same way.

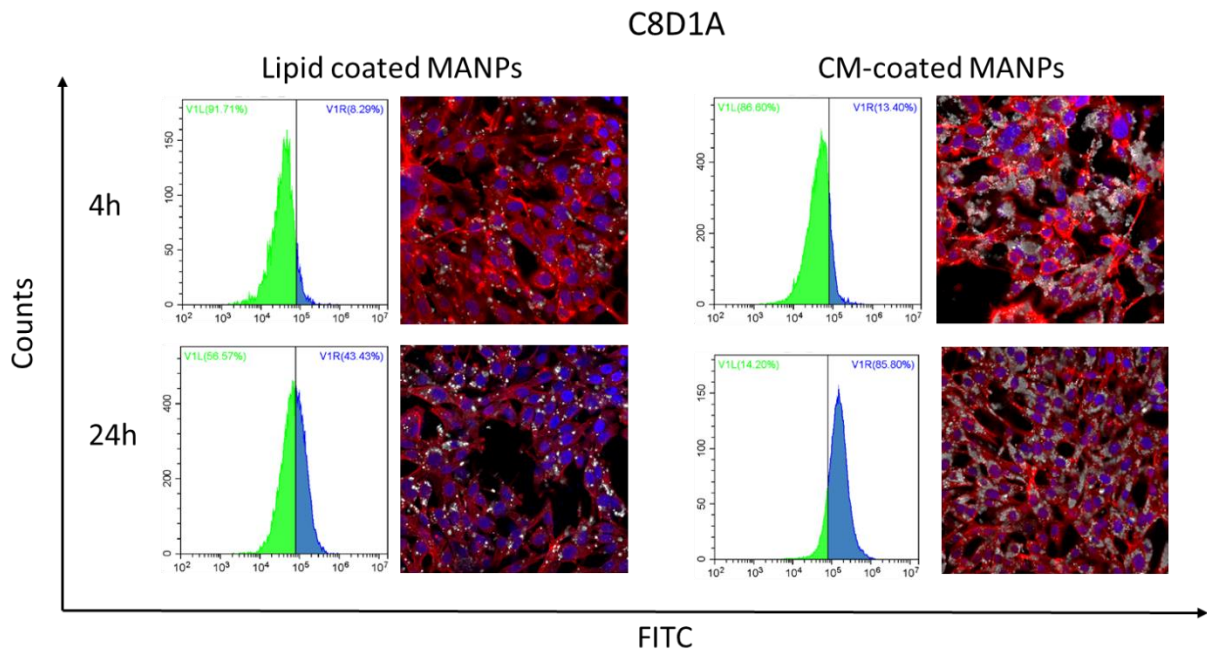


Figure 10.4 Internalization results with C8D1A cell line.

Finally, the internalization with a different brain cancer cell line was tested and the results are reported in **Figure 10.5**. In this case it was possible to observe that 19% of the CM-coated MANPs were uptaken by the cells after 4h, but this percentage did not change after 24h. That means that an amount of the CM-coated NPs inevitably entered the cancer cells, but the number was stable, underlining the difference with the internalization in the GBM cells then showing again that the targeting had a role in the uptake. On the contrary, the lipid-coated NPs' internalization was lower at both the time points (7% and 12% respectively), but it was increasing.

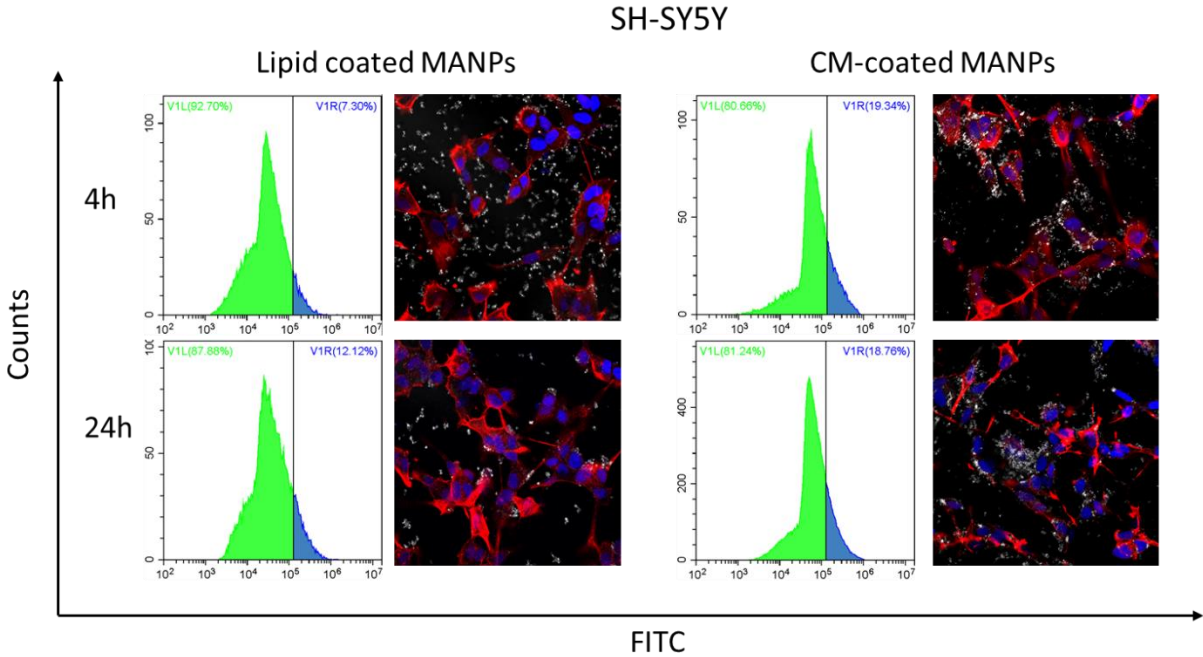


Figure 10.5 Internalization results with SH-SY5Y cell line.

11. Viability studies

Viability studies were performed in order to evaluate the cytotoxicity of the CM-coated and uncoated MANPs.

11.1. Metabolic assay

Experiments in triplicate were performed using Alamar Blue[®] Cell Viability Assay by ThermoFisher. Alamar Blue[®] solution contains some substances that cells are able to metabolize if they are alive. This leads to a change of the absorbance value which is measurable with an absorbance plate reader. Alamar Blue[®] needs to be kept at 4°C and in dark conditions, but it has to be used at room temperature in order not to stress the cells with the temperature change.

Results of the experiments with Alamar Blue[®] are reported in **Figure 11.1**. 25000 U-251 cells were seeded in each well of 24 multiwell plates and they were treated with different concentrations of both uncoated and CM-coated MANPs: 125 µg/ml, 250 µg/ml, 500 µg/ml, and 1000 µg/ml (only for the samples with uncoated NPs). A control was also realized. Then, the cells were analyzed both after 24h and after 72h. At each time point, in order to prepare the samples, the medium of the wells was replaced with a 1:10 Alamar Blue[®]: white media. The well-plate was kept for 2 h (this parameter depends on the cell line type and on the concentration of cells) in the incubator at 37°C, in the dark. Later, the medium with Alamar Blue[®] was replaced with standard medium again and the solutions with Alamar Blue[®] were spun down in order not to keep the NPs in the measured samples. The supernatants were then analyzed with the absorbance plate reader. The absorbance emission was checked at 585 nm.

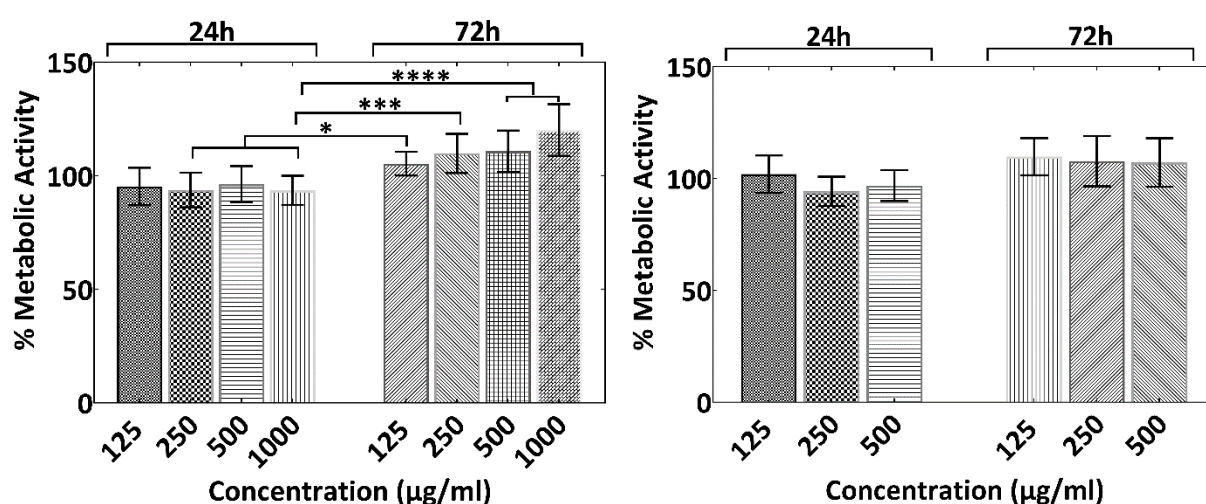


Figure 11.1 Metabolic activity of cells 24h and 72h after the treatment with different concentrations of uncoated NPs (on the left) and CM-coated NPs (on the right).

After 24 h incubation with the NPs, no significant difference was observed in the metabolic activity, either of the uncoated or the CM-coated MANPs. Both for the samples treated with the uncoated and the CM-coated MANPs an increase of the metabolic activity was observed after 72 h suggesting that the proliferation of the U251 cells is not affected even at high concentrations of uncoated or CM-coated MANPs. The level of metabolic activity was significantly higher after 72 h for the cells treated with uncoated NPs compared to the cells treated with the coated NPs suggesting that the increase in the cells' metabolic activity may be affected by the stress that high concentrations of uncoated NPs may cause.

Images of cells with NPs and stained with Coomassie Blue by Sigma-Aldrich® are shown in **Figure 11.2**. 72h after the treatment with the NPs, the samples were fixed by following the same procedure already described in Section 8, and they were washed with deionized water. In every well, 300 µl of Coomassie Blue 0.2% were put and the samples were left 10 min at room temperature. After two cleanings with water to remove the excess of dye, the cells were observed with a standard microscope. In the samples with higher concentrations of NPs it was difficult to clearly see the cells, but in general they showed not to have been affected by the incubation with the MANPs.

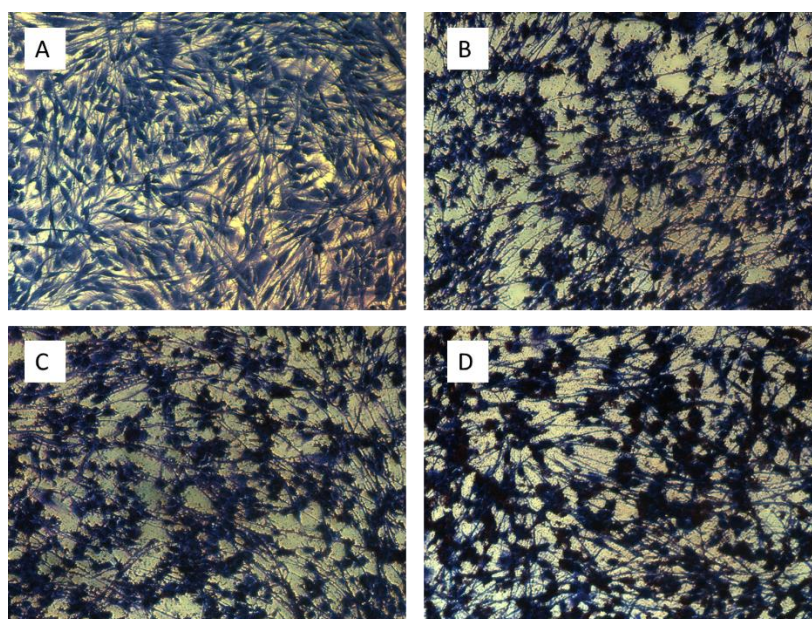


Figure 11.2 Microscope images of samples stained with Coomassie Blue. U-251 cells were treated with different concentrations of NPs, fixed and stained. A) Control B) 125 µg/cm² NPs C) 250 µg/cm² NPs D) 500 µg/cm² NPs

11.2. Proliferation test

Quant-iT™ PicoGreen™ dsDNA Assay Kit was used to analyse the amount of nucleic acid of the cells treated with the NPs. The more the cells proliferated, the higher was the DNA amount. The culture conditions of U-251 cells and the concentrations of MANPs, both uncoated and CM-coated, employed were the same as the ones used for the metabolic assay. At each time point (24h and 72h) the cells

were fixed by following the procedure described in Section 8. Then the samples were washed with PBS and left in water. Multiple cycles of freezing at -80°C and thawing at 37°C were repeated. For each sample a good pipetting for performed to detach everything from the well. Later, the samples were spun down and the supernatants containing the genetic material were properly prepared for the analysis by following the protocol instructions of the assay kit. Finally, the absorbance of the samples was checked (**Figure 11.3**).

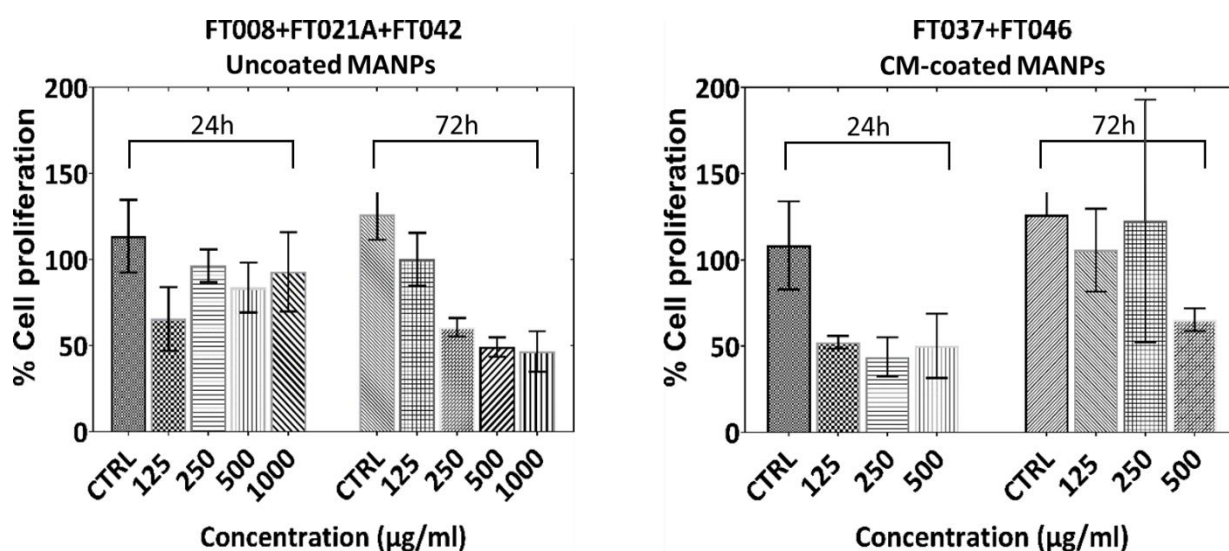


Figure 11.3 Proliferation analysis of cells 24h and 72h after the treatment with different concentrations of uncoated NPs (on the left) and CM-coated NPs (on the right).

Concerning the samples treated with uncoated MANPs, the proliferation alteration is more evident after 72h of incubation with the NPs. In this case, it was also evident that by increasing the concentration of the NPs, the proliferation of the cells was more reduced. In the samples treated with CM-coated MANPs the reduction of proliferation was clearer after 24h, probably due to the coating that allowed a better internalization of the NPs.

11.3. Hyperthermia induced apoptosis

Flow cytometry is an extremely useful tool to determine if cells are viable, apoptotic or necrotic. The Annexin V/Propidium Iodide Apoptosis Assay is usually exploited to understand in which phase the cells are, by considering the differences in plasma membrane integrity and permeability [157]. In fact, late apoptotic and necrotic cells' membranes are characterized by a high level of permeability, which allows propidium iodide to enter the cells and stain the fragmented DNA [158]. Moreover, in the intermediate stages of apoptosis, phosphatidylserine, which is a phospholipid of the cell membrane usually present in the inner and cytoplasmic layer of the membrane, changes its position and it is expressed in the outside layer of the plasma membrane. Thus, apoptotic cells can be distinguished from the others by labeling this molecule with fluorescent Annexin V.

In order to assess the effect of NPs' induced hyperthermia on cancer cells, U-251 cells (30000) were seeded at the glass-bottom center of WillCo-dishes®. Six samples were prepared: two controls, two samples treated with 0.5 mg/ml of CM-coated MANPs, and two samples treated with 1 mg/ml of CM-coated NPs. One dish from each concentration was exposed to an alternated magnetic field once per day for 2h for 3 consecutive days. The parameters of the magnetic field were the ones optimized as described in Section 7, that means 20 mT of AMF and a frequency of 750 kHz. On the 4th day, the samples were washed, trypsinized, spun down and analyzed with the flow cytometer, in order to check the effect of the hyperthermia treatment (**Figure 11.4**). A sample with only NPs was analyzed too, in order to later remove the signal from the flow cytometer associated with free NPs.

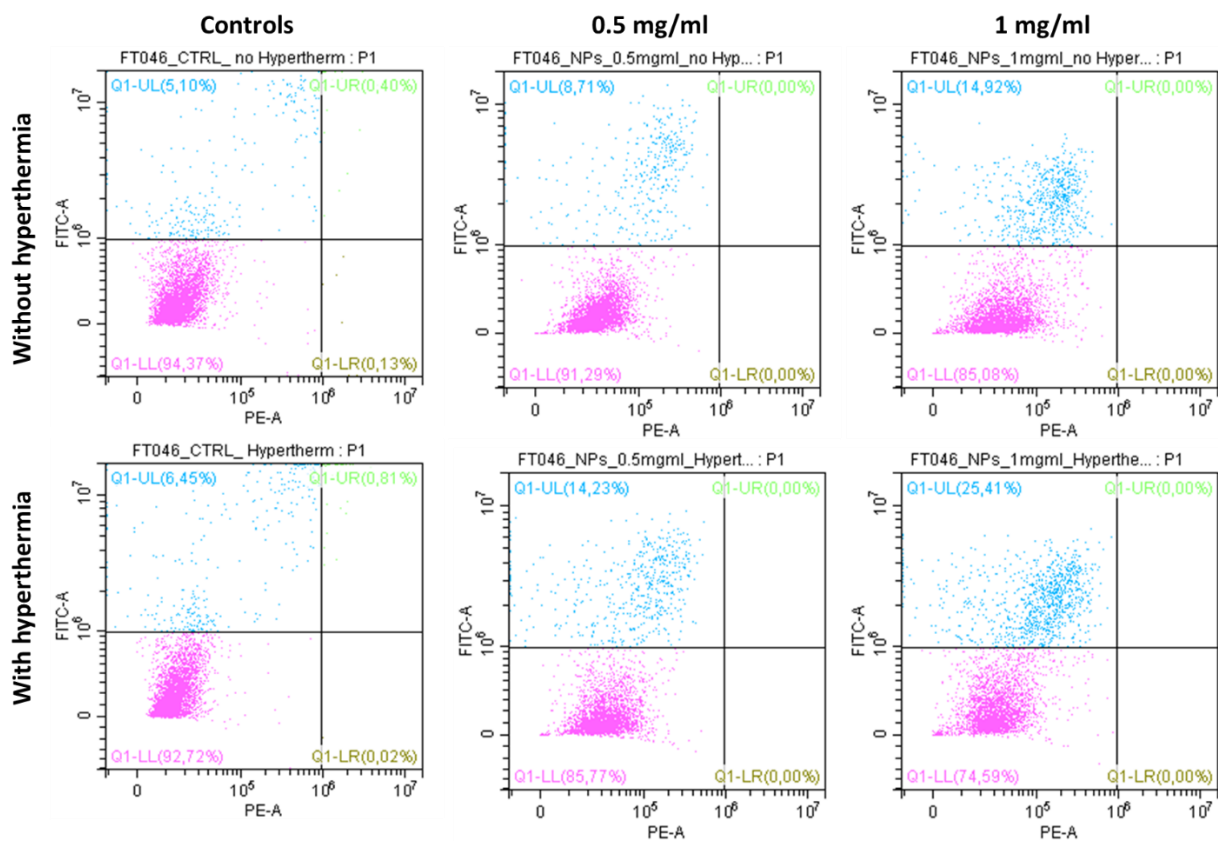


Figure 11.4 Flow cytometry results of the samples chronically exposed to the alternating magnetic field.

In all the samples, the exposure to the magnetic field increased the number of apoptotic cells, but in the samples with the NPs this increase was clearly higher. Indeed, in the control without hyperthermia the apoptotic cells were 5.10% of the total amount, while in the control exposed to the magnetic field this percentage was 6.45%. Among the cells treated with 500 $\mu\text{g}/\text{cm}^2$, 8.71% were apoptotic in the sample without hyperthermia, while 14.23% activated the programmed death pathway when treated with temperature. By doubling the concentration of NPs, the apoptotic cells increased from 14.92% to 25.41% when exposed to the alternating magnetic field. Although, these preliminary results proved the efficacy of the hyperthermia treatment together with the ability of the CM-coated MANPs to reach

the necessary temperature to kill the cancer cells, these experiments should be repeated since an apoptotic effect is also observed in the samples that were not exposed in an alternating magnetic field.

12. The blood brain barrier crossing

An in vitro model of BBB was employed in an experiment aimed both to understand if the CM coating worked as correct functionalization for two targets (the BBB cells together with the cancer cells) and to check the enhancement of the crossing due to the presence of an external magnet.

Briefly, two-compartment BBB models consisting of porous scaffolds (with pores of 3 μm diameter) were used to culture brain endothelial cells at high confluence. The developed endothelial layer completely covered the porous scaffold, separating the luminal chamber (on the top) by the abluminal compartment (on the bottom), and was characterized by a sustained expression of the tight junction marker zonula occludens-1 (**Figure 12.1-A**, ZO-1). The BBB model showed a transendothelial electrical resistance (TEER) of $42 \Omega \cdot \text{cm}^2$ and its permeability to 50 $\mu\text{g}/\text{ml}$ of FITC-dextran (4 kDa) was significantly lower with respect to the plain porous scaffold (**Figure 12.1-B**, without cells; $p < 0.05$).

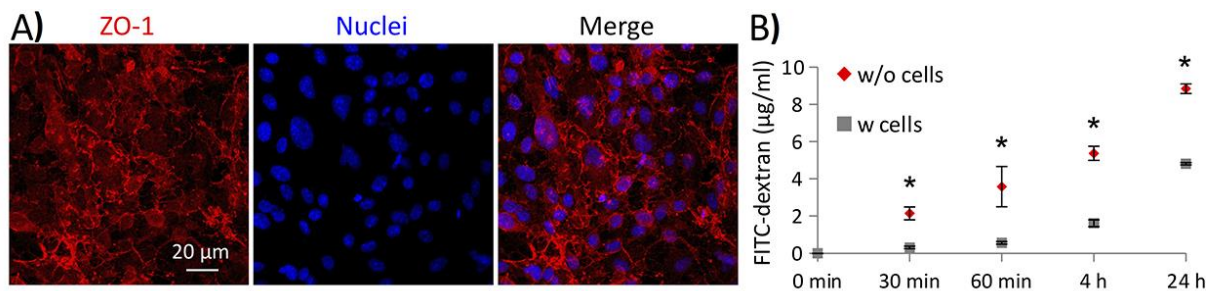


Figure 12.1 BBB in vitro model analysis

A progressive crossing of CM-coated MANPs through the BBB was detected (**Figure 12.3**) when treating the luminal compartment of the BBB model with 200 μg of CM-coated MANPs. The crossing to the abluminal compartment at 1h, 4h, 16h, 24h and 48h of incubation was measured both through transwell with endothelial cells and transwell without cells (**Figure 12.2**).

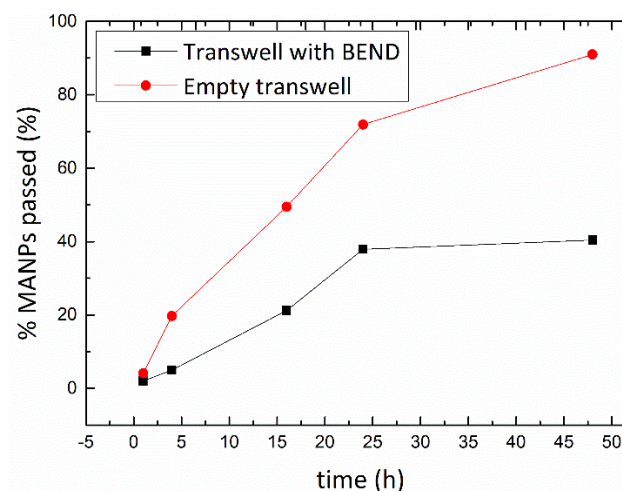


Figure 12.2 Percentage of CM-coated MANPs that passed through the in vitro model of the BBB. Data of the transwell with and without cells are compared.

The percentage of MANPs that passed through the BBB model was half of the percentage of NPs that crossed the transwell without cells. This means that the system has the ability to target the endothelial cells and cross the most problematic barrier for substances in the brain. These preliminary results concerning the ability of CM-coated MANPs to cross the BBB are certainly promising and pave the way to test the efficiency of the presented system on more relevant *in vivo* GBM models for preclinical evaluations.

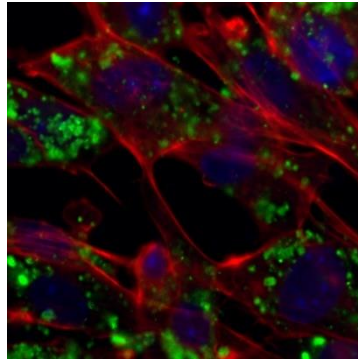


Figure 12.3 CM-coated MANPs uptaken by B.End3 cell line during the BBB crossing experiment.

Conclusions

Glioblastoma multiforme is still one of the most malignant brain tumors and current treatments are not able to improve the life expectancy for more than 5 years. New technologies for surgery and radiotherapy, such as new drugs for chemotherapy are being developed, but innovative treatments are necessary to really overcome the actual problems and help patients.

The cell membrane-coated magnetic and antioxidant NPs realized within this project could be a promising drug delivery system for the treatment of GBM. It showed to have good antioxidant properties (0.5 mg/ml of MANPs have the same antioxidant ability of more than 100 μ M of Trolox) to reduce the ROS-dependent oxidative stress, and it simultaneously produces oxygen (0.5 mg/ml of MANPs are able to increase the oxygen of 20% in 5 min). The consequent hypoxia reduction not only improves the drug and radiotherapy efficacy, but it also blocks the angiogenesis phenomenon in the cancer site. MANPs are stable inside the biological fluids and they can reach the GBM cells both with the help of an external magnet and through the active targeting properties of the cell membrane coating. They are easily uptaken by the endothelial cells (94% in 24h), overcoming the BBB problem of drugs in general (40% of MANPs cross the BBB in 48h), but they are also able to be recognized and uptaken by the cancer cells (86% of MANPs are uptaken by U-251 in 24h). Once in the GBM cells, they can be stimulated through an external alternating magnetic field in order to achieve a controlled release of the TMZ (around 35% in one week) and to add the hyperthermia treatment to their therapeutic effect (43°C can be reached in 30 min). Thanks to the magnetic properties, MANPs' path can also be checked with common imaging techniques.

Of course, a further development of the presented study is possible and necessary, but because of the limited time period some experiments have not been performed. For example, more accurate measurements of the acidosis reduction (and not only of the ROS-scavenging and oxidative reduction) could be realized with proper dyes. A deeper analysis of the components of the employed cell membrane could be performed, for instance with southern blot techniques, in order to understand how to enhance the targeting by adding some molecules or removing some of the existing ones. It could be interesting also deciphering how the interfaces of the cell membrane and the NPs interact during the coating processes. Moreover, the cell membrane production protocol could be further improved by completely eliminating the cytosolic proteins, for example by using ghost cells [119], and by adding a specific targeting for cancerous astrocytes. A further analysis of the amount of uptaken MANPs could be also realized through ICP analysis with cells.

However, the developed system has promising properties and it is original in its way of combining such a consistent number of abilities.

Finally, the project allowed the candidate to explore the laboratory environment, to understand some material characterization methods and together discover how to behave with cell cultures. All the information learned and the abilities acquired will be certainly useful for a career in the research field.

Appendix

Correlograms about the NPs with different molar ratios of Mn/Fe are here reported. The concentration of the under-examination samples was adjusted to 0.1 mg/ml and the temperature was set at 37°C in order to simulate the body temperature. For every Mn/Fe ratio, three solvents were used to disperse the NPs: water, DMEM and DMEM+10%FBS. All the samples were also tested at different time points: 0 h (that means after 1 min sonication), 1 h, 6 h, and 24 h after the addition of the solvent; the samples were always kept at 37°C.

The correlograms confirmed what the intensity graphs had already shown: the NPs created agglomerates in DMEM more than what they did in DMEM+10%FBS. Indeed, the DMEM plots show bigger oscillations when the correlation coefficient decreased.

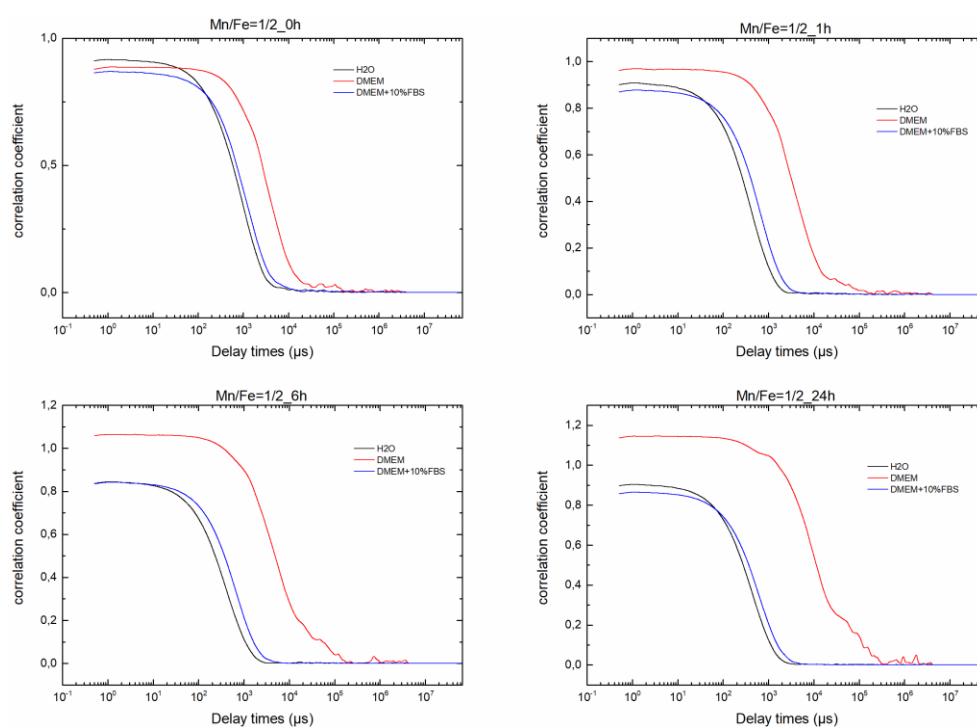


Figure 0.1 Correlation graphs of the sample with Mn/Fe=1/2 ratio. The measurements were run at 37°C, at different time points (0h, 1h, 6h, 24h), and with water, DMEM or DMEM+10%FBS.

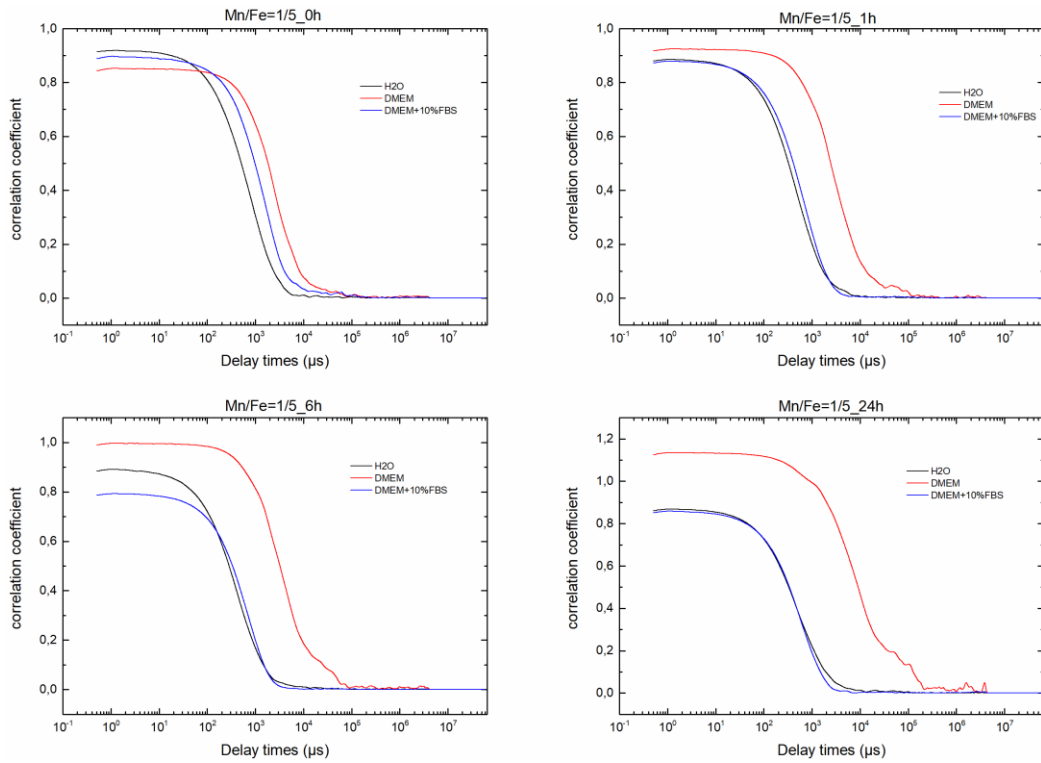


Figure 0.2 Correlation graphs of the sample with Mn/Fe=1/5 ratio. The measurements were run at 37°C, at different time points (0h, 1h, 6h, 24h), and with water, DMEM or DMEM+10%FBS.

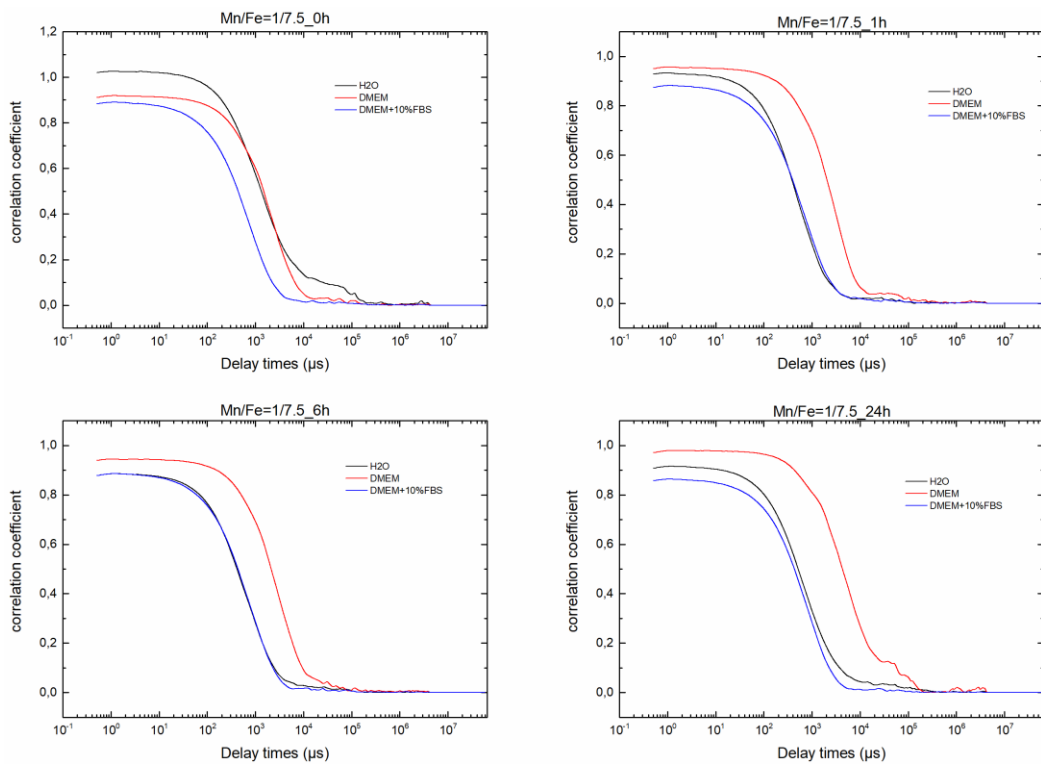


Figure 0.3 Correlation graphs of the sample with Mn/Fe=1/7.5 ratio. The measurements were run at 37°C, at different time points (0h, 1h, 6h, 24h), and with water, DMEM or DMEM+10%FBS.

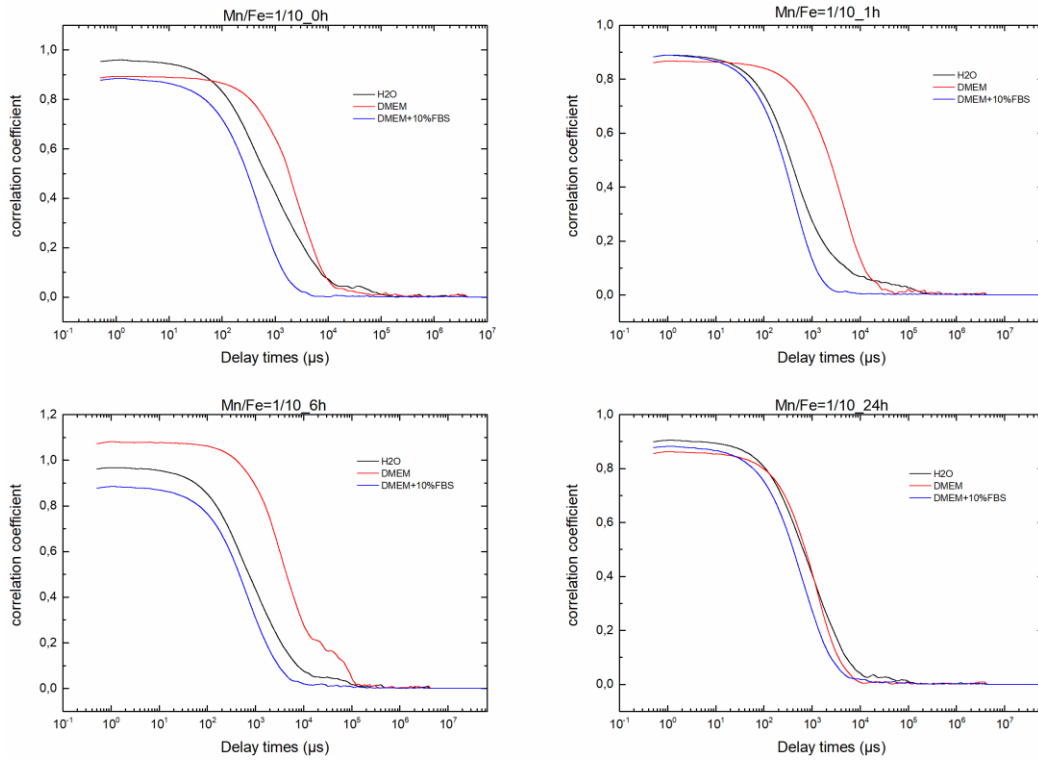


Figure 0.4 Correlation graphs of the sample with Mn/Fe=1/10 ratio. The measurements were run at 37°C, at different time points (0h, 1h, 6h, 24h), and with water, DMEM or DMEM+10%FBS.

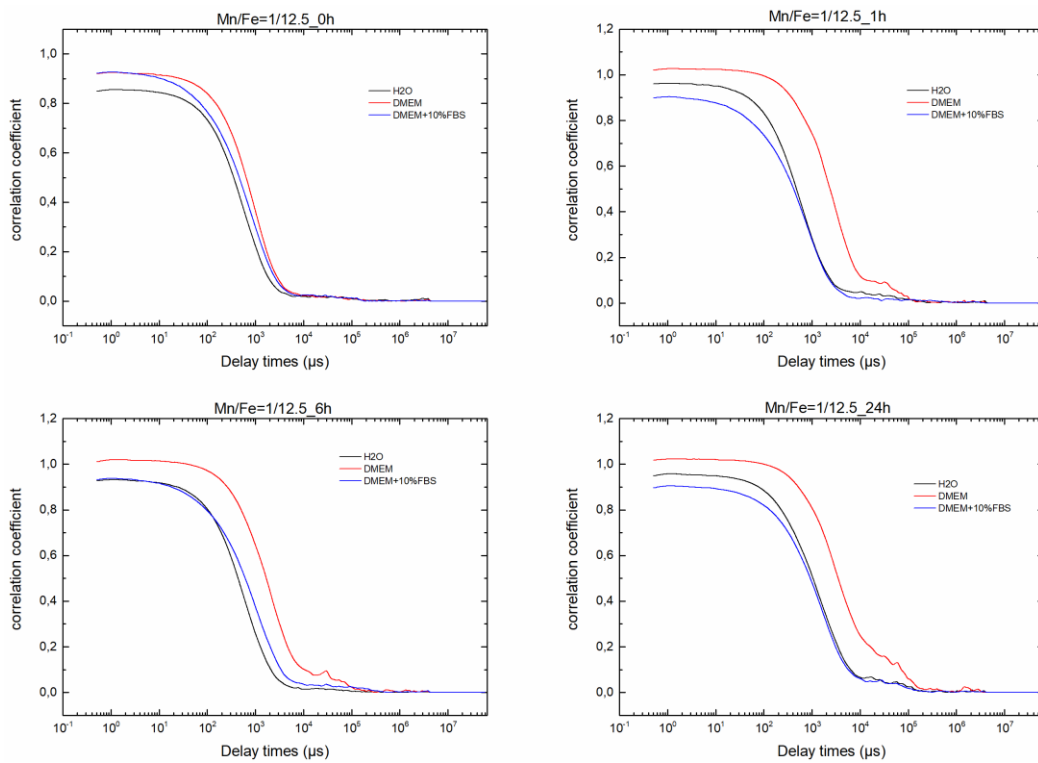


Figure 0.5 Correlation graphs of the sample with Mn/Fe=1/12.5 ratio. The measurements were run at 37°C, at different time points (0h, 1h, 6h, 24h), and with water, DMEM or DMEM+10%FBS.

Bibliography

1. Stoyanov, G.S., et al., *Correlation Between Ki-67 Index, World Health Organization Grade and Patient Survival in Glial Tumors With Astrocytic Differentiation*. Cureus, 2017. **9**(6): p. e1396.
2. Brandes, A.A., et al., *Glioblastoma in adults*. Crit Rev Oncol Hematol, 2008. **67**(2): p. 139-52.
3. Stoyanov, G.S., et al., *Cell biology of glioblastoma multiforme: from basic science to diagnosis and treatment*. Med Oncol, 2018. **35**(3): p. 27.
4. Holland, E.C., *Glioblastoma multiforme: The terminator*. Proceedings of the National Academy of Sciences of the United States of America, 2000. **97**(12): p. 6242-6244.
5. Belot, N., et al., *Molecular characterization of cell substratum attachments in human glial tumors relates to prognostic features*. Glia, 2001. **36**(3): p. 375-90.
6. Nakada, M., et al., *Integrin alpha3 is overexpressed in glioma stem-like cells and promotes invasion*. Br J Cancer, 2013. **108**(12): p. 2516-24.
7. Sidransky, D., et al., *Clonal expansion of p53 mutant cells is associated with brain tumour progression*. Nature, 1992. **355**: p. 846.
8. Robert, M. and M. Wastie, *Glioblastoma multiforme: a rare manifestation of extensive liver and bone metastases*. Biomed Imaging Interv J, 2008. **4**(1): p. e3.
9. Fiaschi, T. and P. Chiarugi, *Oxidative stress, tumor microenvironment, and metabolic reprogramming: a diabolic liaison*. Int J Cell Biol, 2012. **2012**: p. 762825.
10. Park, J., J. Lee, and C. Choi, *Mitochondrial network determines intracellular ROS dynamics and sensitivity to oxidative stress through switching inter-mitochondrial messengers*. PLoS One, 2011. **6**(8): p. e23211.
11. Lamonte, G., et al., *Acidosis induces reprogramming of cellular metabolism to mitigate oxidative stress*. Cancer Metab, 2013. **1**(1): p. 23.
12. Sgarbi, G., et al., *Hypoxia and IF(1) Expression Promote ROS Decrease in Cancer Cells*. Cells, 2018. **7**(7).
13. Milane, L., et al., *Multi-modal strategies for overcoming tumor drug resistance: hypoxia, the Warburg effect, stem cells, and multifunctional nanotechnology*. J Control Release, 2011. **155**(2): p. 237-47.
14. Lee, S.L., et al., *Hypoxia-induced pathological angiogenesis mediates tumor cell dissemination, invasion, and metastasis in a zebrafish tumor model*. Proc Natl Acad Sci U S A, 2009. **106**(46): p. 19485-90.
15. von Neubeck, C., et al., *Glioblastoma multiforme: emerging treatments and stratification markers beyond new drugs*. Br J Radiol, 2015. **88**(1053): p. 20150354.

16. Carlsson, S.K., S.P. Brothers, and C. Wahlestedt, *Emerging treatment strategies for glioblastoma multiforme*. EMBO Mol Med, 2014. **6**(11): p. 1359-70.
17. Gzell, C., et al., *Radiotherapy in Glioblastoma: the Past, the Present and the Future*. Clin Oncol (R Coll Radiol), 2017. **29**(1): p. 15-25.
18. Dinnes, J., et al., *A rapid and systematic review of the effectiveness of temozolomide for the treatment of recurrent malignant glioma*. British Journal Of Cancer, 2002. **86**: p. 501.
19. Stella Pelengaris, M.K., *The molecular biology of cancer: a bridge from bench to bedside*. Wiley Blackwell, 2011.
20. Thurston, D.E., *Chemistry and Pharmacology of Anticancer Drugs*. 2006: CRC Press Inc.
21. Oshiro, S., et al., *Efficacy of temozolomide treatment in patients with high-grade glioma*. Anticancer Res, 2009. **29**(3): p. 911-7.
22. Ujifuku, K., et al., *miR-195, miR-455-3p and miR-10a(*) are implicated in acquired temozolomide resistance in glioblastoma multiforme cells*. Cancer Lett, 2010. **296**(2): p. 241-8.
23. Brandes, A.A., et al., *Role of MGMT Methylation Status at Time of Diagnosis and Recurrence for Patients with Glioblastoma: Clinical Implications*. Oncologist, 2017. **22**(4): p. 432-437.
24. Cocucci, E., G. Racchetti, and J. Meldolesi, *Shedding microvesicles: artefacts no more*. Trends Cell Biol, 2009. **19**(2): p. 43-51.
25. Shao, H., et al., *Protein typing of circulating microvesicles allows real-time monitoring of glioblastoma therapy*. Nat Med, 2012. **18**(12): p. 1835-40.
26. Manterola, L., et al., *A small noncoding RNA signature found in exosomes of GBM patient serum as a diagnostic tool*. Neuro Oncol, 2014. **16**(4): p. 520-7.
27. Srividya, M.R., et al., *Homozygous 10q23/PTEN deletion and its impact on outcome in glioblastoma: a prospective translational study on a uniformly treated cohort of adult patients*. Neuropathology, 2011. **31**(4): p. 376-83.
28. Corwin, D., et al., *Toward patient-specific, biologically optimized radiation therapy plans for the treatment of glioblastoma*. PLoS One, 2013. **8**(11): p. e79115.
29. Dunn, G.P., L.J. Old, and R.D. Schreiber, *The immunobiology of cancer immunosurveillance and immunoediting*. Immunity, 2004. **21**(2): p. 137-48.
30. Carter, H., et al., *Cancer-specific high-throughput annotation of somatic mutations: computational prediction of driver missense mutations*. Cancer Res, 2009. **69**(16): p. 6660-7.
31. Swartz, A.M., Q.J. Li, and J.H. Sampson, *Rindopepimut: a promising immunotherapeutic for the treatment of glioblastoma multiforme*. Immunotherapy, 2014. **6**(6): p. 679-90.
32. Zhou, Q., Y. Wang, and W. Ma, *The progress of immunotherapy for glioblastoma*. Hum Vaccin Immunother, 2015. **11**(11): p. 2654-8.

33. Rick, J., A. Chandra, and M.K. Aghi, *Tumor treating fields: a new approach to glioblastoma therapy*. J Neurooncol, 2018. **137**(3): p. 447-453.
34. Ryu, J.H., et al., *Theranostic nanoparticles for future personalized medicine*. J Control Release, 2014. **190**: p. 477-84.
35. Genchi, G.G., et al., *Smart Materials Meet Multifunctional Biomedical Devices: Current and Prospective Implications for Nanomedicine*. Front Bioeng Biotechnol, 2017. **5**: p. 80.
36. Tapeinos, C. and A. Pandit, *Physical, Chemical, and Biological Structures based on ROS-Sensitive Moieties that are Able to Respond to Oxidative Microenvironments*. Adv Mater, 2016. **28**(27): p. 5553-85.
37. Masserini, M., *Nanoparticles for brain drug delivery*. ISRN Biochem, 2013. **2013**: p. 238428.
38. Marino, A., et al., *Gold Nanoshell-Mediated Remote Myotube Activation*. ACS Nano, 2017. **11**(3): p. 2494-2508.
39. Tapeinos, C., et al., *Sustained release profile of quatro stimuli nanocontainers as a multi sensitive vehicle exploiting cancer characteristics*. Colloids Surf B Biointerfaces, 2016. **148**: p. 95-103.
40. Marino, A., et al., *Piezoelectric Nanoparticle-Assisted Wireless Neuronal Stimulation*. ACS Nano, 2015. **9**(7): p. 7678-89.
41. Tapeinos, C., et al., *Microspheres as therapeutic delivery agents: synthesis and biological evaluation of pH responsiveness*. J. Mater. Chem. B, 2013. **1**(2): p. 194-203.
42. Dubertret, B., et al., *In vivo imaging of quantum dots encapsulated in phospholipid micelles*. Science, 2002. **298**(5599): p. 1759-62.
43. Jun, B.-H., et al., *Ultrasensitive, Biocompatible, Quantum-Dot-Embedded Silica Nanoparticles for Bioimaging*. Advanced Functional Materials, 2012. **22**(9): p. 1843-1849.
44. Bazylińska, U., et al., *Core/shell quantum dots encapsulated in biocompatible oil-core nanocarriers as two-photon fluorescent markers for bioimaging*. Langmuir, 2014. **30**(49): p. 14931-43.
45. Zhou, J., Y. Yang, and C.Y. Zhang, *Toward Biocompatible Semiconductor Quantum Dots: From Biosynthesis and Bioconjugation to Biomedical Application*. Chem Rev, 2015. **115**(21): p. 11669-717.
46. Ciofani, G., et al., *Folate Functionalized Boron Nitride Nanotubes and their Selective Uptake by Glioblastoma Multiforme Cells: Implications for their Use as Boron Carriers in Clinical Boron Neutron Capture Therapy*. Nanoscale Res Lett, 2008. **4**(2): p. 113-121.
47. Stanley, S.A., et al., *Radio-wave heating of iron oxide nanoparticles can regulate plasma glucose in mice*. Science, 2012. **336**(6081): p. 604-8.

48. Wetterskog, E., et al., *Size and property bimodality in magnetic nanoparticle dispersions: single domain particles vs. strongly coupled nanoclusters*. *Nanoscale*, 2017. **9**(12): p. 4227-4235.
49. Parmar, H., et al., *Size Dependent Heating Efficiency of Iron Oxide Single Domain Nanoparticles*. *Procedia Engineering*, 2015. **102**: p. 527-533.
50. Bastl, Z., et al., *Nickel nanoparticle assembly on single-crystal support: formation, composition and stability*. *Nanotechnology*, 2006. **17**(5): p. 1492-1500.
51. Kirkpatrick, E.M., S.A. Majetich, and M.E. McHenry, *Magnetic properties of single domain samarium cobalt nanoparticles*. *IEEE Transactions on Magnetics*, 1996. **32**(5): p. 4502-4504.
52. Colombo, M., et al., *Biological applications of magnetic nanoparticles*. *Chem Soc Rev*, 2012. **41**(11): p. 4306-34.
53. Zhang, E., et al., *Dynamic magnetic fields remote-control apoptosis via nanoparticle rotation*. *ACS Nano*, 2014. **8**(4): p. 3192-201.
54. Shen, J.M., et al., *cRGD-functionalized polymeric magnetic nanoparticles as a dual-drug delivery system for safe targeted cancer therapy*. *Pharmacol Res*, 2013. **70**(1): p. 102-15.
55. Rivera Gil, P., et al., *Nanopharmacy: Inorganic nanoscale devices as vectors and active compounds*. *Pharmacological Research*, 2010. **62**(2): p. 115-125.
56. Ciofani, G., et al., *Effects of cerium oxide nanoparticles on PC12 neuronal-like cells: proliferation, differentiation, and dopamine secretion*. *Pharm Res*, 2013. **30**(8): p. 2133-45.
57. Kim, S.S., et al., *A nanoparticle carrying the p53 gene targets tumors including cancer stem cells, sensitizes glioblastoma to chemotherapy and improves survival*. *ACS Nano*, 2014. **8**(6): p. 5494-514.
58. Ciardelli, G., et al., *Acrylic polymeric nanospheres for the release and recognition of molecules of clinical interest*. *Biosens Bioelectron*, 2004. **20**(6): p. 1083-90.
59. Barenholz, Y., *Doxil(R)--the first FDA-approved nano-drug: lessons learned*. *J Control Release*, 2012. **160**(2): p. 117-34.
60. Swierczewska, M., S. Lee, and X. Chen, *Inorganic Nanoparticles for Multimodal Molecular Imaging*. *Molecular Imaging*, 2011. **10**(1): p. 7290.2011.00001.
61. Gou, Y., et al., *Bio-Inspired Protein-Based Nanoformulations for Cancer Theranostics*. *Front Pharmacol*, 2018. **9**: p. 421.
62. Shea, J.E., et al., *Genexol inhibits primary tumour growth and metastases in gemcitabine-resistant pancreatic ductal adenocarcinoma*. *HPB (Oxford)*, 2011. **13**(3): p. 153-7.
63. Von Hoff, D.D., et al., *Phase I Study of PSMA-Targeted Docetaxel-Containing Nanoparticle BIND-014 in Patients with Advanced Solid Tumors*. *Clin Cancer Res*, 2016. **22**(13): p. 3157-63.

64. Stirland, D.L., et al., *Mind the gap: a survey of how cancer drug carriers are susceptible to the gap between research and practice*. J Control Release, 2013. **172**(3): p. 1045-64.
65. Rempe, R., et al., *Transport of Poly(n-butylcyano-acrylate) nanoparticles across the blood-brain barrier in vitro and their influence on barrier integrity*. Biochem Biophys Res Commun, 2011. **406**(1): p. 64-9.
66. Chrastina, A., K.A. Massey, and J.E. Schnitzer, *Overcoming in vivo barriers to targeted nanodelivery*. Wiley Interdiscip Rev Nanomed Nanobiotechnol, 2011. **3**(4): p. 421-37.
67. Absolom, D.R., [13] *Opsonins and dysopsonins: An overview*. 1986. **132**: p. 281-318.
68. Choi, H.S., et al., *Renal clearance of quantum dots*. Nat Biotechnol, 2007. **25**(10): p. 1165-70.
69. Shinde Patil, V.R., et al., *Particle diameter influences adhesion under flow*. Biophys J, 2001. **80**(4): p. 1733-43.
70. He, Y., et al., *Cell-culture models of the blood-brain barrier*. Stroke, 2014. **45**(8): p. 2514-26.
71. Kręcisz, M., et al., *Interactions between magnetic nanoparticles and model lipid bilayers—Fourier transformed infrared spectroscopy (FTIR) studies of the molecular basis of nanotoxicity*. Journal of Applied Physics, 2016. **120**(12): p. 124701.
72. Wahajuddin and S. Arora, *Superparamagnetic iron oxide nanoparticles: magnetic nanoplatforms as drug carriers*. Int J Nanomedicine, 2012. **7**: p. 3445-71.
73. Mahmoudi, M., et al., *Toxicity evaluations of superparamagnetic iron oxide nanoparticles: cell "vision" versus physicochemical properties of nanoparticles*. ACS Nano, 2011. **5**(9): p. 7263-76.
74. Schlachter, E.K., et al., *Metabolic pathway and distribution of superparamagnetic iron oxide nanoparticles: in vivo study*. Int J Nanomedicine, 2011. **6**: p. 1793-800.
75. Liu, X., et al., *One pot synthesis of Fe₃O₄/MnO₂ core-shell structured nanocomposites and their application as microwave absorbers*. RSC Advances, 2015. **5**(31): p. 24016-24022.
76. Leng, Y., *Materials Characterization : Introduction to Microscopic and Spectroscopic Methods*. 2013, Weinheim, GERMANY: John Wiley & Sons, Incorporated.
77. Giannuzzi, L.A. and F.A. Stevie, *Introduction to Focused Ion Beams. Instrumentation, Theory, Techniques and Practice*. 2005.
78. Tscharnuter, W., *Photon Correlation Spectroscopy in Particle Sizing*. Encyclopedia of Analytical Chemistry, 2000.
79. Kholodenko, A.L. and J.F. Douglas, *Generalized Stokes-Einstein equation for spherical particle suspensions*. Physical Review E, 1995. **51**(2): p. 1081-1090.
80. Moore, T.L., et al., *Nanoparticle colloidal stability in cell culture media and impact on cellular interactions*. Chem Soc Rev, 2015. **44**(17): p. 6287-305.

81. Bunaciu, A.A., E.G. Udristoiu, and H.Y. Aboul-Enein, *X-ray diffraction: instrumentation and applications*. Crit Rev Anal Chem, 2015. **45**(4): p. 289-99.
82. Langford, J.I. and A.J.C. Wilson, *Scherrer after sixty years: A survey and some new results in the determination of crystallite size*. Journal of Applied Crystallography, 1978. **11**(2): p. 102-113.
83. Cornell, R.M. and U. Schwertmann, 2003.
84. Griffiths, P.R., *Fourier Transform Infrared Spectrometry*. Science, 1983. **222**(4621): p. 297-302.
85. van der Heide, P., *X-ray Photoelectron Spectroscopy : An introduction to Principles and Practices*. 2011, Hoboken, UNITED STATES: Wiley.
86. Beauchemin, D., *Inductively coupled plasma mass spectrometry*. Anal Chem, 2010. **82**(12): p. 4786-810.
87. Brunauer, S., P.H. Emmett, and E. Teller, *Adsorption of Gases in Multimolecular Layers*. Journal of the American Chemical Society, 1938. **60**(2): p. 309-319.
88. Langmuir, I., *The Constitution and Fundamental Properties of Solids and Liquids. Part I. Solids*. Journal of the American Chemical Society, 1916. **38**(11): p. 2221-2295.
89. De Lange, M.F., et al., *Adsorptive characterization of porous solids: Error analysis guides the way*. Microporous and Mesoporous Materials, 2014. **200**: p. 199-215.
90. Romagnoli, M., et al., *Effect of drying method on the specific surface area of hydrated lime: A statistical approach*. Powder Technology, 2013. **246**: p. 504-510.
91. Czarnecki, J. and J. Sestak, *From recording balances to thermogravimetric instruments and back*. Journal of Thermal Analysis and Calorimetry, 2015. **120**(1): p. 157-166.
92. Coats, A.W. and J.P. Redfern, *Thermogravimetric analysis. A review*. The Analyst, 1963. **88**(1053): p. 906.
93. Estelrich, J., et al., *Iron oxide nanoparticles for magnetically-guided and magnetically-responsive drug delivery*. Int J Mol Sci, 2015. **16**(4): p. 8070-101.
94. Freeman, M.W., A. Arrott, and J.H.L. Watson, *Magnetism in Medicine*. Journal of Applied Physics, 1960. **31**(5): p. S404-S405.
95. Kost, J., J. Wolfrum, and R. Langer, *Magnetically enhanced insulin release in diabetic rats*. J Biomed Mater Res, 1987. **21**(12): p. 1367-73.
96. Zhao, Z., et al., *One pot synthesis of tunable Fe₃O₄-MnO₂ core-shell nanoplates and their applications for water purification*. Journal of Materials Chemistry, 2012. **22**(18): p. 9052.
97. Visser, D., Armstrong, Sauer, Yachandra, *FTIR Spectra and Normal-Mode Analysis of a Tetranuclear Manganese Adamantane-like Complex in Two Electrochemically Prepared Oxidation States: Relevance to the Oxygen-Evolving Complex of Photosystem II*. 2002.

98. Cao, J.-L., et al., *Mesoporous Co–Fe–O nanocatalysts: Preparation, characterization and catalytic carbon monoxide oxidation*. Journal of Environmental Chemical Engineering, 2014. **2**(1): p. 477-483.
99. Srivastava, M., et al., *Synthesis of superparamagnetic bare Fe(3)O(4) nanostructures and core/shell (Fe(3)O(4)/alginate) nanocomposites*. Carbohydr Polym, 2012. **89**(3): p. 821-9.
100. R. Palanivel, G.V., *FTIR and FT-Raman spectroscopic studies of fired clay artifacts recently excavated in Tamilnadu, India*. Indian Journal of pure & applied physics, 2007. **45**: p. 501-508.
101. Abboud, M., et al., *Superparamagnetic Fe₃O₄ nanoparticles, synthesis and surface modification*. Materials Science in Semiconductor Processing, 2015. **39**: p. 641-648.
102. Samali, A., et al., *Thermotolerance and cell death are distinct cellular responses to stress: dependence on heat shock proteins*. FEBS Letters, 1999. **461**(3): p. 306-310.
103. Kolhatkar, A.G., et al., *Magnetic Sensing Potential of Fe₃O₄ Nanocubes Exceeds That of Fe₃O₄ Nanospheres*. ACS Omega, 2017. **2**(11): p. 8010-8019.
104. Zhu, L.-P., et al., *One-Pot Template-Free Synthesis of Monodisperse and Single-Crystal Magnetite Hollow Spheres by a Simple Solvothermal Route*. Crystal Growth & Design, 2008. **8**(3): p. 957-963.
105. Huang, Z. and F. Tang, *Preparation, structure, and magnetic properties of mesoporous magnetite hollow spheres*. J Colloid Interface Sci, 2005. **281**(2): p. 432-6.
106. Sing, K.S.W., *Reporting physisorption data for gas/solid systems with special reference to the determination of surface area and porosity (Recommendations 1984)*. Pure and Applied Chemistry, 1985. **57**(4): p. 603-619.
107. Thommes, M., et al., *Physisorption of gases, with special reference to the evaluation of surface area and pore size distribution (IUPAC Technical Report)*. Pure and Applied Chemistry, 2015. **87**(9-10).
108. Bhambhani, M.R., et al., *Analysis of nitrogen adsorption isotherms on porous and nonporous silicas by the BET and as methods*. Journal of Colloid and Interface Science, 1972. **38**(1): p. 109-117.
109. Nayek, C., et al., *Investigating Size- and Temperature-Dependent Coercivity and Saturation Magnetization in PEG Coated Fe₃O₄ Nanoparticles*. Magnetochemistry, 2017. **3**(2): p. 19.
110. Fesenko, O. and L. Yatsenko, *Nanophysics, Nanomaterials, Interface Studies, and Applications: Selected Proceedings of the 4th International Conference Nanotechnology and Nanomaterials (NANO2016), August 24-27, 2016, Lviv, Ukraine*. 2017: Springer International Publishing.
111. Arosio, P., et al., *Magnetism and spin dynamics of novel encapsulated iron oxide superparamagnetic nanoparticles*. Dalton Trans, 2013. **42**(28): p. 10282-91.

112. Vilema-Enriquez, G., et al., *Molecular and Cellular Effects of Hydrogen Peroxide on Human Lung Cancer Cells: Potential Therapeutic Implications*. *Oxid Med Cell Longev*, 2016. **2016**: p. 1908164.
113. Halliwell, B., M.V. Clement, and L.H. Long, *Hydrogen peroxide in the human body*. *FEBS Letters*, 2000. **486**(1): p. 10-13.
114. Charles, S. and J. Popplewell, *Progress in the development of ferromagnetic liquids*. *IEEE Transactions on Magnetics*, 1980. **16**(2): p. 172-177.
115. Wu, Z., et al., *Turning erythrocytes into functional micromotors*. *ACS Nano*, 2014. **8**(12): p. 12041-8.
116. Rao, L., et al., *Cancer Cell Membrane-Coated Upconversion Nanoprobes for Highly Specific Tumor Imaging*. *Adv Mater*, 2016. **28**(18): p. 3460-6.
117. Fang, R.H., et al., *Cancer cell membrane-coated nanoparticles for anticancer vaccination and drug delivery*. *Nano Lett*, 2014. **14**(4): p. 2181-8.
118. Jang, H.S., *The Diverse Range of Possible Cell Membrane Interactions with Substrates: Drug Delivery, Interfaces and Mobility*. *Molecules*, 2017. **22**(12).
119. Goh, W.J., et al., *nCVTs: a hybrid smart tumour targeting platform*. *Nanoscale*, 2018. **10**(15): p. 6812-6819.
120. Laurens, L.M.L. and E.J. Wolfrum, *Feasibility of Spectroscopic Characterization of Algal Lipids: Chemometric Correlation of NIR and FTIR Spectra with Exogenous Lipids in Algal Biomass*. *BioEnergy Research*, 2010. **4**(1): p. 22-35.
121. Zarshenas, K., A. Raisi, and A. Aroujalian, *Surface modification of polyamide composite membranes by corona air plasma for gas separation applications*. *RSC Advances*, 2015. **5**(25): p. 19760-19772.
122. Dilnawaz, F., et al., *Dual drug loaded superparamagnetic iron oxide nanoparticles for targeted cancer therapy*. *Biomaterials*, 2010. **31**(13): p. 3694-706.
123. Feiner-Gracia, N., et al., *Super-Resolution Microscopy Unveils Dynamic Heterogeneities in Nanoparticle Protein Corona*. *Small*, 2017. **13**(41).
124. Thompson, E.J., *The roster of CSF proteins*. 2005: p. 13-31.
125. Carl-Bertil, G.K.a.L., *Measurement of IgG and Albumin Content of Cerebrospinal Fluid and Its Interpretation*. *CLIN. CHEM.*, 1974. **20**(5): p. 571-573.
126. Blennow K., F.P., Wallin A., Gottfries C. G., Karlsson I., Langstrom G., Skoog I., Svennerholm L., Wikkelso C., *Protein analysis in cerebrospinal fluid*. *Eur Neurol*, 1993. **33**: p. 129-133.
127. Gstraunthaler, G., *Alternatives to the use of fetal bovine serum: Serum-free cell culture*. *ALTEX - Alternatives to animal experimentation*, 2003. **20**(4): p. 275-281.

128. Steven W. Stites, M.M.E.N., MD; and Lewis]. Wesselius, MD, FCCP, *Transferrin Concentrations in Serum and Lower Respiratory Tract Fluid of Mechanically Ventilated Patients With COPD or ARDS**. *Chest*, 1995. **107**: p. 1681-85.
129. P. Gallo, F.B., S. Morara, L. Battistin and B. Tavolato, *The Cerebrospinal Fluid Transferrin/Tau Proteins. A Study by Two-Dimensional Polyacrylamide Gel Electrophoresis (2D) and Agarose Isoelectrofocusing (IEF) Followed by Double-Antibody Peroxidase Labeling and Avidin-Biotin Amplification*. *Journal of the Neurological Sciences*, 1985. **70**: p. 81-92.
130. Gifford, A.H.T., *Serum Stimulates Growth of and Proteinase Secretion by Aspergillus fumigatus*. *Infection and Immunity*, 2002. **70**(1): p. 19-26.
131. Gautam, P., et al., *Proteins with altered levels in plasma from glioblastoma patients as revealed by iTRAQ-based quantitative proteomic analysis*. *PLoS One*, 2012. **7**(9): p. e46153.
132. Sato Y1, H.Y., Asoh T, Oizumi K, Ohshima Y, Honda E, *Cerebrospinal fluid ferritin in glioblastoma: evidence for tumor synthesis*. *J Neurooncol.*, 1998. **40**(1): p. 47-50.
133. Sindic C J M, C.-C.D., Cambiaso C L, Masson P L, Laterre E C *The clinical relevance of ferritin concentration in the cerebrospinal fluid*. *Journal of Neurology, Neurosurgery, and Psychiatry*, 1981. **44**: p. 329-333.
134. Kakuta, K., et al., *High Levels of Ferritin and its Iron in Fetal Bovine Serum*. *Comparative Biochemistry and Physiology Part A: Physiology*, 1997. **118**(1): p. 165-169.
135. Jha, S., P.K. Sharma, and R. Malviya, *Hyperthermia: Role and Risk Factor for Cancer Treatment*. *Achievements in the Life Sciences*, 2016. **10**(2): p. 161-167.
136. Leuenberger, P., et al., *Cell-wide analysis of protein thermal unfolding reveals determinants of thermostability*. *Science*, 2017. **355**(6327).
137. DeNardo, G.L. and S.J. DeNardo, *Update: Turning the heat on cancer*. *Cancer Biother Radiopharm*, 2008. **23**(6): p. 671-80.
138. Nguyen, D.T. and K.-S. Kim, *Controlled Magnetic Properties of Iron Oxide-Based Nanoparticles for Smart Therapy*. *KONA Powder and Particle Journal*, 2016. **33**(0): p. 33-47.
139. Shete, P.B., et al., *Magnetic chitosan nanocomposite for hyperthermia therapy application: Preparation, characterization and in vitro experiments*. *Applied Surface Science*, 2014. **288**: p. 149-157.
140. J, S.H. and W. Hitoshi, *Materials Processing In Magnetic Fields - Proceedings Of The International Workshop On Materials Analysis And Processing In Magnetic Fields*. 2005: World Scientific Publishing Company.
141. Kuznetsov, O.A., et al., *ESR study of thermal demagnetization processes in ferromagnetic nanoparticles with Curie temperatures between 40 and*. *Journal of Magnetism and Magnetic Materials*, 2007. **311**(1): p. 204-207.

142. He, L., et al., *Finite size effect on Néel temperature with Co₃O₄ nanoparticles*. Journal of Applied Physics, 2007. **102**(10): p. 103911.
143. Wang, J., et al., *Curie temperature reduction in SiO₂-coated ultrafine Fe₃O₄ nanoparticles: Quantitative agreement with a finite-size scaling law*. Applied Physics Letters, 2011. **98**(8): p. 083107.
144. Babincová, M., et al., *AC-magnetic field controlled drug release from magnetoliposomes: design of a method for site-specific chemotherapy*. Bioelectrochemistry, 2002. **55**(1-2): p. 17-19.
145. Hergt, R., et al., *Magnetic particle hyperthermia: nanoparticle magnetism and materials development for cancer therapy*. Journal of Physics: Condensed Matter, 2006. **18**(38): p. S2919-S2934.
146. Guardia, P., et al., *Water-soluble iron oxide nanocubes with high values of specific absorption rate for cancer cell hyperthermia treatment*. ACS Nano, 2012. **6**(4): p. 3080-91.
147. Kallumadil, M., et al., *Suitability of commercial colloids for magnetic hyperthermia*. Journal of Magnetism and Magnetic Materials, 2009. **321**(10): p. 1509-1513.
148. Wildeboer, R.R., P. Southern, and Q.A. Pankhurst, *On the reliable measurement of specific absorption rates and intrinsic loss parameters in magnetic hyperthermia materials*. Journal of Physics D: Applied Physics, 2014. **47**(49): p. 495003.
149. Jang, J.T., et al., *Giant Magnetic Heat Induction of Magnesium-Doped gamma-Fe₂O₃ Superparamagnetic Nanoparticles for Completely Killing Tumors*. Adv Mater, 2018. **30**(6).
150. Farokhzad, O.C. and R. Langer, *Impact of nanotechnology on drug delivery*. ACS Nano, 2009. **3**(1): p. 16-20.
151. Kumari, S., et al., *Overcoming blood brain barrier with a dual purpose Temozolomide loaded Lactoferrin nanoparticles for combating glioma (SERP-17-12433)*. Scientific Reports, 2017. **7**(1): p. 6602.
152. Bertucci, A., et al., *Combined Delivery of Temozolomide and Anti-miR221 PNA Using Mesoporous Silica Nanoparticles Induces Apoptosis in Resistant Glioma Cells*. Small, 2015. **11**(42): p. 5687-95.
153. Hu, J., et al., *Pharmacokinetics and antitumor efficacy of DSPE-PEG2000 polymeric liposomes loaded with quercetin and temozolomide: Analysis of their effectiveness in enhancing the chemosensitization of drug-resistant glioma cells*. Int J Mol Med, 2016. **37**(3): p. 690-702.
154. Russell, D.S. and J.O.W. Bland, *A study of gliomas by the method of tissue culture*. The Journal of Pathology and Bacteriology, 1933. **36**(2): p. 273-283.
155. PONTÉN, J. and E.H. MACINTYRE, *LONG TERM CULTURE OF NORMAL AND NEOPLASTIC HUMAN GLIA*. Acta Pathologica Microbiologica Scandinavica, 1968. **74**(4): p. 465-486.

156. Vogel, T.W., et al., *Proteins and protein pattern differences between glioma cell lines and glioblastoma multiforme*. Clin Cancer Res, 2005. **11**(10): p. 3624-32.
157. Rieger, A.M., et al., *Modified annexin V/propidium iodide apoptosis assay for accurate assessment of cell death*. J Vis Exp, 2011(50).
158. Riccardi, C. and I. Nicoletti, *Analysis of apoptosis by propidium iodide staining and flow cytometry*. Nat Protoc, 2006. **1**(3): p. 1458-61.

Acknowledgments

Thank you to Prof. Gianni Ciofani for giving me the opportunity to spend these months at the Istituto Italiano di Tecnologia in Pontedera: I learnt a lot and I deeply realised how much I love doing research. But thank you also for the opportunities related to the project, such as the article and the conference, and for the help with the PhD application. Thanks to all the Smart Bio Interfaces group for accepting me and for helping me.

An enormous thanks to Christos: you are the best supervisor I could hope to meet, but you're also a precious friend. I admire you and I will forever be grateful to you for all the knowledge you transferred to me, for the help and for the advices, for making me have fun in the lab, for showing me how difficult but also how wonderful is the research world. Thanks for the unforgettable time spent together, I will miss you a lot. BSSFE

Un grazie particolare a Matteo per la pazienza infinita nello spiegarmi una procedura nuova in ogni momento libero e per gli esperimenti portati avanti insieme o anche solo immaginati con tanto entusiasmo. Grazie per avermi aiutata e fatta sentire a mio agio fin dal primo momento all'IIT, per aver prestato attenzione a tutti i miei dettagli estetici e linguistici, per aver portato ogni giorno l'allegria in laboratorio.

Grazie a Simone e a Luca, simpatici compagni di avventure in questa esperienza toscana.

Grazie a Cristina, per avermi permesso di entrare per la prima volta in un laboratorio, alimentando il mio entusiasmo ogni giorno per tre mesi. Sei esattamente la ricercatrice che vorrei diventare.

Grazie ai miei amici. A quelli di sempre, con cui sono cresciuta e con i quali non ho mai smesso di confrontarmi e di ridere: Carlo, Simona, Elena, Niccolò, Enrico, Giorgia, Myriam, Stefano, Federica. Grazie agli amici di Roma e del Collegio dei Cavalieri del Lavoro, fondamentali compagni di viaggio che si sono conquistati un posto indelebile nel mio cuore: Erik, Digio, Gabriella, Giulia, Elisabetta, Liviana, Davide, Giulio, Vittorio, Noemi, Sara, Lella, Emanuele, Pasquale. Grazie alle compagne di avventure torinesi per avermi fatto amare i due anni di Magistrale: Valentina, Chiara, Sara, Giorgia, Anna, Mariana, Elisa.

Grazie a chi mi ha accompagnata per tre anni, facendomi crescere e insegnandomi tanto sul mondo e su me stessa. "A mano a mano si scioglie nel pianto/quel dolce ricordo sbiadito dal tempo/di quando vivevi con me in una stanza".

Grazie ai nonni, instancabilmente pronti ad accogliermi con un sorriso quando torno a casa. Grazie agli zii, per il tifo fatto ad ogni esame e per avermi sempre coccolata come una figlia.

Un grazie gigantesco va a Mamma e Papà, che mi hanno sempre appoggiata, spronata, sostenuta nei momenti entusiasmanti come in quelli davvero difficili. Grazie a Papi per avermi lasciata libera di seguire la mia strada e per avermi capita quando ne avevo bisogno. Grazie a Mami per avermi resa forte davanti agli ostacoli e determinata a inseguire i miei sogni. Senza di voi non sarei mai arrivata alla fine di questo percorso; il lavoro che ho fatto è anche vostro. Vorrei avere almeno un decimo delle qualità che avete voi due: siete il mio esempio come persone, come genitori e come coppia. Vi voglio un mondo di bene.

Grazie a Edolin, il fratello meraviglioso senza il quale la mia vita non avrebbe senso, per essere SEMPRE riuscito a farmi sorridere. La generosità che ti caratterizza, la capacità di superare gli ostacoli e il tuo sguardo attento sul mondo non smetteranno mai di stupirmi. Sono orgogliosa di te e sei la persona di cui mi fido di più nell'universo. Ti auguro la vita fantastica e piena di felicità che ti meriti. Ti voglio tantissimo bene!

Infine, grazie a te, Edo, amore mio, per avermi dato la serenità di cui avevo bisogno per affrontare l'Università. Grazie per la delicatezza con cui sei entrato nella mia vita, per il tempo e le migliaia di coccole che mi dedichi (anche quando sono insopportabile), per la travolgente felicità che mi regali continuamente. Grazie per la capacità che hai di capirmi e di farmi ridere. Sono consapevole di essere incredibilmente fortunata ad averti accanto.